Thin films of Nanomaterials at Interfaces and their Applications

THESIS

Submitted in partial fulfillment
of the requirements for the degree of

Doctor Of Philosophy

by

Amrit Kumar
ID: 2019PHXF0063P

Under the Supervision of

Prof. Raj Kumar Gupta

BITS Pilani
Pilani | Dubai | Goa | Hyderabad

BIRLA INSTITUTE OF TECHNOLOGY AND SCIENCE, PILANI

2024

BIRLA INSTITUTE OF TECHNOLOGY AND SCIENCE, PILANI

CERTIFICATE

This is to certify that the work reported in the Ph.D. thesis entitled "**Thin Films of Nanomaterials at Interfaces and their Applications**", submitted by **Amrit Kumar**, with ID. **2019PHXF0063P** at the Physics Department, BITS Pilani, Pilani campus for the award of the degree of Doctor of Philosophy (Ph.D.), is a bonafide record of his original work carried out under my supervision. This work has not been submitted elsewhere for any other degree or diploma.

(Prof. Raj Kumar Gupta)

Professor, Department of Physics
BITS - Pilani, Pilani Campus, Rajasthan, India.

Date:

Dedicated to ...
my mother, my father and my teachers

ACKNOWLEDGEMENTS

I want to start by sincerely thanking my advisor, Prof. Raj Kumar Gupta, for his unwavering support of my Ph.D. research, for his inspiration, passion, and immense knowledge, and for granting me the opportunity in the adept environment. I could not have imagined having a better advisor and mentor for my doctoral study.

In addition to my advisor, I am grateful to the remaining members of my thesis review committee: Prof. Manjuladevi V and Prof. Anshuman Dalvi. Their motivating support, perceptive observations, constructive critique, and valuable suggestions throughout the progress review and thesis drafting process are sincerely appreciated.

I sincerely thank Prof. Manjuladevi V., Head of the Department for her persistent support. Also, I wish to express my gratitude to all the past HODs, DRC conveners, and faculty members of the physics department for their kind support from time to time. A special thanks to Prof Manjuladevi V. for her kind support and training on various experimental techniques particularly in impedance based measurements. Thanks to Prof. Jayendra N. Bandyopadhyay for fostering a memorable and enjoyable teacher-student bond. Additionally, I extend my appreciation to Prof. Navin Singh for igniting the theoretical aspect in my doctoral research journey. The technical staff of the department, Rajeev Ji, Shrikant Ji & Kundan, are also gratefully thanked for their help.

I would humbly express my regards to the Vice-Chancellor, Director and Deans of Birla Institute of Technology & Science (BITS), Pilani, for allowing me to pursue my doctoral studies by providing the necessary facilities and financial support. I extend my heartfelt gratitude to Associate Dean of AGSRD Prof. Shamik Chakraborty and all other staff members of AGSRD are also gratefully thanked for their help.

I would like to express my gratitude to (Dr.) Shivaraja S.J. and (Dr.) Shweta R Mishra, Dr. Neelakshi, Dr M.Dinachandra Singh, Dr Ram and Dr Nikita whose companionship and friendship have enriched these years. I would especially like to thank Dr. Chandrachud, Anju, Akash, Shristi and Chaitanya for all the support they have provided me during my toughest times here at BITS Pilani.

In the same breath, I would also like to thank all the lab mates and colleagues who helped me during my journey. Thanks to (Dr.) Parul, (Dr.) Asutosh Joshi, Preeti, Garima , Mudit, Samarth, Parsoon, Ayush and Mayuri.

Last but not least, I want to express my heartfelt gratitude to my family. Their unwavering support has been the cornerstone of my journey, with special mention to my parents. Their constant belief in my aspirations and unending encouragement has been my guiding light. Over the years, they have imparted the invaluable lesson that diligence knows no bounds and that any goal is within reach through hard work. A special also goes to my brother and my sister in law, whose genuine and steadfast support has been a constant source of strength.

Finally, despite my love for physics, the work reported in this thesis would not have been possible without the financial support of DST-SERB project : CRG/2018/000755 and BITS Pilani Institute fellowship, for which I am grateful.

Amrit Kumar
BITS-Pilani, Pilani campus

ABSTRACT

In nanomaterials thin film research, understanding molecular arrangements at interfaces is crucial for customizing material properties. Materials can form ultrathin films at interfaces, allowing for the modification of their physicochemical properties. Amphiphilic molecules like fatty acids, cholesterol, lipids, and liquid crystals can be spread onto the water surface to create a stable monomolecular layer known as a Langmuir monolayer. At the air-water (A/W) interface, this monolayer exhibits various surface phases depending on surface density. These phases can be transferred to solid substrates using Langmuir-Blodgett (LB) or Langmuir-Schaefer (LS) techniques for device applications. These ultrathin LB films are valuable due to their stability and controllable nanoarchitecture, making them useful in sensors, electronic devices, and coatings. Nanomaterials, with at least one dimension smaller than 100 nanometers, exhibit unique properties due to quantum confinement effects, increased surface area to volume ratio, and novel nanoscale interactions. These properties differ significantly from their bulk counterparts and can be exploited for advanced applications in electronics, energy, catalysis, sensing, and biomedical fields. Aligning nanomaterials in ultrathin films enhances their properties and performance. Nanomaterials can be tailored for specific analyte interactions by engineering their composition and morphology. Research has focused on nanostructured carbon allotropes like carbon dots, carbon nanotubes (CNT), graphene, and fullerene due to their unique properties and diverse applications. CNT and graphene, with their exceptional electrical and mechanical properties, are promising for sensing applications, offering superior sensitivity and biocompatibility due to $\pi - \pi$ interactions.

Pristine-CNT are hydrophobic and tend to aggregate at A/W and air-solid (A/S) interfaces. Functionalizing CNT improves their dispersion in organic solvents and processability. Functionalization stabilizes the Langmuir monolayer at the A/W interface and enhances analyte interaction during sensing, improving sensitivity and selectivity. In gas sensing, particularly for acetone detection, metal-oxide-based platforms have been widely studied but exhibit drawbacks like high power consumption and elevated temperature operation. These platforms typically use resistance as an output parameter, which is temperature-

dependent. Hence, there is a need for a gas sensing platform capable of detecting acetone over a wide concentration range with a low detection limit at ambient temperatures.

This thesis proposes the use of octadecylamine-functionalized carbon nanotubes (ODA-CNT) for acetone sensing. Investigations reveal that ODA-CNT can sense acetone across a broad concentration range (1-300 ppm) with a low detection limit (0.5 ppm) at room temperature. The surface π-electrons of CNTs enhance gas molecule affinity, and even minor perturbations can disturb the conjugated π-electron system upon interaction with analytes. CNTs operate effectively at room temperature with minimal power consumption, making them suitable for diverse applications in environmental monitoring, industrial safety, and healthcare diagnostics.

Graphene, a 2D carbon nanomaterial, is another promising candidate due to its high electrical conductivity, exceptional mechanical strength, and excellent thermal conductivity. It has a plethora of surface π-electrons for bioconjugation, making it suitable for applications in electronics, sensors, energy storage, and composite materials. The thesis explores ultrathin films of ODA-functionalized graphene (ODA-gr) at different interfaces and uses LB films for E. coli sensing. E. coli is a major source of water/food contamination, leading to chronic diseases and deaths in developing countries. Early and low-level detection of E. coli is crucial. Existing pathogen sensing techniques in potable water are often time-consuming, expensive, label-based, and require pre-processing. Thus, a label-free, easy-to-operate sensing mechanism is needed. This thesis proposes ODA-functionalized graphene for label-free and selective E. coli detection using Electrochemical Impedance Spectroscopy (EIS), achieving a detection limit of 2.5 colony-forming units/mL (cfu/mL).

Label-free measurements in sensing technology are essential as they reduce dependence on fluorescent tags that may interfere with molecular interactions. Various techniques like electrochemical, capacitive, resistive, optical, piezoelectric, magnetic, and calorimetric are known. Surface plasmon resonance (SPR) offers high-precision, label-free measurements, making it valuable in bio-sensing and bioanalysis. In order to improve selectivity and sensitivity of SPR based sensors, often the metallic layers are functionalized with suitable ligands. The strength of the plasmon field decays exponentially in the sensing medium. Bio-ligands are in general very thick and thereby the perceptibility of SPR device due to binding of analytes with such ligands are poor. There-

fore, it is essential to optimize the film thickness and the nature of material for enhanced sensing using SPR phenomenon. In this thesis we have addressed some of the important issues related to sensing using SPR which are not investigated elsewhere. We present our research on the role of anisotropy in ultrathin film on the SPR response and present a calibration curve displaying the effect of film thickness, optical anisotropy on the SPR response. The calibration curve was employed to estimate the optical birefringence in ultrathin LB film of organic materials. This study was the first of its kind. In general, whenever ultrathin film is developed for sensing using SPR, it lacks uniformity over a large length scale. In such cases, the film can be considered as a sub-monolayer where the surface coverage (S_o) is less than 1. In this thesis, we present our investigation by simulating the SPR phenomenon using finite domain time difference (FDTD) methods by considering the sub-monolayer of silver nanoparticles as a function of surface coverage. Interestingly, we report insulator-metal transition above a critical surface coverage of the silver nanoparticle in the sub-monolayer regime. The similar system was verified experimentally and we report a good agreement of simulation and experimental findings. Additional simulations were carried out to consider anisotropy in ultrathin films with variable surface density, examining SPR spectra and plasmonic fields based on nanotube alignment. These studies provide valuable information for development of advanced functionalized layers for SPR-based sensing. The thesis also investigates the plasmonic characteristics of graphene systems, demonstrating their capability to generate plasmonic fields in the terahertz frequency range. Graphene exhibits strong bio-affinity, enhancing its potential for sensitive biological material detection. The thesis evaluates the sensing performance of monolayer, bilayer, and twisted bilayer graphene systems, with twisted bilayer graphene near the magic angle showing the highest sensitivity of 29,120 nm/RIU due to strong interlayer coupling. This research contributes to the development of advanced SPR sensors with dual functionality for bio-sensing and plasmonic applications.

Contents

List of Figures

List of Tables

LIST OF ABBREVIATIONS/SYMBOLS

A/W	air-water
2D	Two Dimensional
A/S	air-solid
LB	Langmuir-Blodgett
LS	Langmuir-Schaefer
CNT	Carbon nanotubes
BAM	Brewster angle microscopy
$FESEM$	Field emission scanning electron microscopy
SPR	Surface plasmon resonance
FOM	figure-of-merit
π	Surface pressure
E	Elastic modulus
λ	wavelength
RA	Resonance angle
SPP	Surface plasmon polaritons
DFT	Density Functional theory
$FDTD$	Finite Difference Time Domain
ODA	Octadecylamine
S/V	surface to volume ratio
ppm	parts per million
PCA	Principal components analysis

Z_{imag}	imaginary component of the impedance
Z_{real}	real component of the impedance
C	Capacitance (Farads)
R	Resistance (Ohms)
cfu/mL	colony forming units/milliliter
$CdSA$	Cadmium stearate
$8CB$	4′-octyl-4-biphenylcarbonitrile
S_o	Surface coverage
RIU	Refractive index units
MLG	Monolayer graphene
BLG	Bilayer graphene
$T-BLG$	Twisted bilayer graphene

CHAPTER 1

Introduction

In the field of nanomaterials research, the interface plays an important role in defining the properties and behaviors of materials at the nanoscale. An interface refers to the boundary or region where two different phases meet, such as solid-liquid, liquid-liquid, or gas-liquid interfaces. These interfaces are dynamic and often exhibit unique properties distinct from those of the bulk phases. The molecules at the interface undergo unique arrangements due to the influence of surface effects and interactions with neighboring phases. Understanding this molecular arrangement at the interface is critical for customizing the material property. The unique molecular arrangement can be utilized for a variety of technological and scientific disciplines, including chemistry, physics, and materials science. Interface energy governs critical phenomena like adhesion and phase transformations, governing the stability of interfaces, spreading, and bonding processes. The comprehensive understanding of interface energy enables the prediction and control of material behaviors, facilitating the development of tailored adhesives, coatings, and materials. Interfaces also serve as hosts for defects, such as vacancies, dislocations, and grain boundaries, which significantly impact mechanical, electrical, and optical properties. Understanding defects at interfaces is crucial for optimizing material performance and reliability across various applications. Moreover, molecules at interfaces exhibit unique electronic and optical properties due to quantum confinement and interfacial charge transfer effects, offering advancements in optoelectronics and photonics.

1.1 Air-water (A/W) interface

Among the various interfaces, studying the molecular arrangement at the air/water (A/W) interface is of great importance. It is easier to create and control disturbances at the A/W interface. The various advantages of A/W interfaces are well recognized in supramolecular chemistry and materials science research. The A/W interface can provide opportunities for the fabrication of thin films of organic semiconductor, 2D carbon nanomaterials, metal–organic frameworks (MOFs), covalent organic frameworks (COFs)[1]. In a recent article by Wan et al.[2], authors have reviewed fabrication of various 2D films at a A/W interface and their applications in many fields such as photoelectric conversion, fluorescence, electronic devices, chemical sensing, electrocatalysis, and molecular separation. Further, on the water surface, the difference in environment between surface molecules and those in the bulk results in excess free energy of water. The hydrogen bonding in water creates loosely defined networks that are constantly modified near the surface. Therefore, certain molecules when dispersed at the A/W interface try to orient themselves at the interface to minimize their energy. If the molecules are neutral, then the forces between them will be short range and the layer will be of one or two molecules thick. This monomolecular thick two dimensional layer of the self arranged molecules are termed as Langmuir monolayer[3]. The Langmuir monolayer formed at the A/W interface shows variety of phases depending on the molecular arrangement and ordering. Numerous application of Langmuir monolayer at the A/W interface has been reported[4, 5]. There are variety of organic molecules that posses both hydrophilic head group and non-polar hydrophobic tail group. Such molecules are known as amphiphillic molecules. These molecules are mixed with a volatile polar solvent to form a homogeneous solution which can be spread at the A/W interface. As the solvent gets evaporated, a uniform single layer of molecules is formed, which is termed as Langmuir monolayer. In the monolayer, the head group of the amphiphilic molecules are anchored to the water surface due to electrostatic interactions, such as ion-dipole or dipole-dipole interactions (including hydrogen bonds). The hydrophobic tail part experiences repulsive interactions with water and van der Waals interaction with each other. The balance between the hydrophillic and hydrophobic interactions leads to the stabilization of the film[3, 6, 7].

Amphiphiles such as fatty acids, cholesterol and its derivatives, lipids and phospholipids have been extensively studied in the past at the A/W interface due to their biological relevance. The compression and expansion of such molecules on the A/W interface has helped in understanding the working of biological membranes[6].

The compression of the monolayer using the mechanical barriers in the lateral direction gives rise to various phase transitions and control over the nanoarchitecture of the ultrathin film. With the increase in the surface density, the monolayer undergoes phase transitions depending on the nature of molecule-molecule and molecules-water interactions.

1.2 Air-solid (A/S) interface

Studying monolayers at the A/W interface yields valuable insights into surface phases which are governed by intermolecular forces. Such phases from the A/W interface can be transferred to solid substrate via techniques such as Langmuir-Blodgett (LB) or Langmuir-Schaefer methods. The transferred Langmuir monolayer on to the solid substrate is interpreted as ultrathin films at the air-solid (A/S) interface. The A/S interface, serves as a platform for investigations of various properties and molecular behaviors which are essential for the design of efficient functional layers. The key parameters for investigating ultrathin film at A/S interface are surface morphology, molecular packing, and interactions. These information are crucial for understanding surface science leading to the development of innovative technologies in fields such as sensors, electronic devices, and coatings. The phases of Langmuir film can be transferred on to the solid substrates by the vertical dipping mechanism known as Langmuir-Blodgett (LB) technique[8, 9]. The monolayer at the A/W interface is held at a given phase and through the vertical motion of the substrate the film is transferred. The key advantage of the LB technique is the ability to precisely control the deposition of molecules onto the solid substrate. This control enables the creation of well-ordered uniform films with tailored properties. Additionally, by varying parameters such as the dipping speed, angle, and number of deposition cycles, the structure and morphology of the transferred film can also be manipulated.

Langmuir-Schaefer (LS)[10] technique is a variation of the LB method. In the LS technique, the solid substrate is horizontally withdrawn from the A/W interface, allowing the monolayer to deposit onto the substrate. The LS technique is applicable to the cases where molecules have poor adsorption capability to the substrate. Inverse Langmuir-Schaefer (ILS) technique is another variation where the solid substrate placed under the water before the formation of Langmuir monolayer. The substrate is lifted upward after the formation of monolayer on the water surface. The substrate is tilted a few degrees with respect to the horizontal for facilitating the drainage of entrapped water[1].

Recently the advancement in material research has largely shifted towards nanomaterials due to their exceptional properties and it would be interesting to study different types of nanomaterials at the A/W and A/S interface.

1.3 Nanomaterials

Nanomaterials refer to materials that have at least one dimension in the nanoscale, generally ranging from 1 to 100 nanometers. They are pivotal in scientific research due to their unique properties and wide applications. These materials play a crucial role in various fields like medicine, electronics, energy, and environmental science. Nanomaterials are of different types based on quantum confinement in dimensions: zero-dimensional (0D), one-dimensional (1D), two-dimensional (2D), and three-dimensional (3D). In 0D nanomaterials, such as quantum dots, confinement occurs in all three dimensions, leading to discrete electronic states. 1D nanomaterials, like nanowires and nanotubes, exhibit unique properties due to confinement along two dimensions. Prominent examples of 2D nanomaterials include graphene, which consists of a single layer of carbon atoms and posses exceptional physiochemical properties. 3D nanomaterials, while maintaining bulk properties, offer enhanced surface-to-volume ratio, making them ideal for number of applications.

Nanomaterials often serve as valuable functional layers in sensing devices due to their high surface area-to-volume ratio. This property enhances interactions with target substances, improving sensitivity and selectivity in detection[11]. The composition and morphology of nanomaterials can be precisely tailored to interact with specific analytes, significantly enhancing their sensing performance.

The fabrication of ultrathin films from nanomaterials offers a larger surface area for interaction with analytes. This increased surface-to-volume ratio enhances sensitivity, allowing for the detection of trace amounts of substances. This capability is crucial for sensitive applications such as medical diagnostics and environmental monitoring. Overall, nanomaterial-based ultrathin films represent a promising field for advanced sensing technologies with improved efficiency and reliability[12, 13].

1.3.1 Carbon Nanomaterials

Over the last two decades, there has been extensive research into nanostructured allotropes of carbon due to their distinctive hybridization characteristics and susceptibility to alteration during synthesis, facilitating precise control over material properties [14]. Notably, the chemical, mechanical, thermal, and electrical attributes of these allotropes are closely linked to their structural configuration. The most widely studied carbon allotropes are Carbon dots, Carbon nanotubes (CNT), Graphene and fullerene. Carbon dots are 0D nanomaterials, whereas CNT are 1D, graphene has a 2D structure and fullerene are considered to be 3D or bulk form of carbon nanomaterials. The discovery of fullerenes, CNT, and graphene has led to a active research in different fields like nanotechnology, electronics, materials science, energy, drug delivery, bioimaging, field emission devices and medical diagnostics[15, 16].

Carbon nanomaterials, especially CNT and graphene, exhibit unique structural, electrical, and chemical properties that makes them interesting systems to study. CNT, with their one-dimensional nanostructures and high aspect ratio, offer exceptional electrical conductivity and mechanical strength. Similarly, graphene, a two-dimensional carbon allotrope, shows remarkable electronic and mechanical properties, along with a large surface area, making it an attractive candidate for various applications[17–19].

CNT and graphene also have pleothra of surface π electrons which enhances their sensitivity towards external perturbation, making them valuable materials for sensing applications [20–23]. In graphene, the hexagonal lattice structure provides an extensive surface area with a high density of delocalized

π electrons, which can readily interact with molecules adsorbed on its surface. This interaction can induce changes in the electronic properties of graphene, such as conductivity or band structure, which can be measured to detect the presence or concentration of specific analytes.

Similarly, CNT possess a high aspect ratio and a large surface area, along with π-electron rich surface. This configuration allows them to interact strongly with molecules or species adsorbed on their surface, leading to changes in their electronic/optical properties.

1.3.2 Advantages of sensing with carbon nanomaterials

- **Superior sensing merit:** Sensing using carbon nanomaterials offers several distinct advantages over conventional sensing platforms [24, 25]. Their inherent sensitivity enables the detection of target analytes at extremely low concentrations, surpassing the detection limits of traditional sensing technologies. This enhanced sensitivity is particularly beneficial for applications requiring early disease diagnosis [26, 27] or trace-level pollutant detection [28, 29].

- **Biocompatibilty:** Carbon nanomaterials exhibit excellent biocompatibility, making them suitable for interfacing with biological systems without inducing adverse effects. This attribute is particularly advantageous for healthcare applications, such as biosensing and medical diagnostics [30, 31], where compatibility with biological samples is critical. Moreover, the stability of carbon nanomaterials ensure reliable and long-term sensing performance, essential for real-world applications in harsh or dynamic environments.

- **Multifunctional Sensor:** The versatility of carbon nanomaterials allows for the development of multifunctional sensors capable of detecting multiple analytes simultaneously or performing complex sensing tasks, further expanding their utility across diverse applications [32, 33]. Thus, sensing with carbon nanomaterials offers a promising pathway towards the development of advanced sensing technologies with enhanced performance, reliability, and functionality.

1.4 Fabrication of ultrathin films

There exist numerous methods for fabricating ultrathin films of carbon nanomaterials. Some of these include chemical vapor deposition (CVD)[34, 35], chemical exfoliation[36, 37], mechanical exfoliation[38], self-assembly[39, 40], and the LB technique[22, 41–43]. While all these methods are widely used, the LB technique has proven to be particularly effective for producing ultrathin films of nanomaterials due to its cost-effectiveness and ability to precisely control the structure. Although, LB method was conventionally employed for the deposition of amphiphilic molecues, in the diverse landscape of material science research, a significant category of materials exists that lack amphiphilic properties has emerged. Instead some of these molecules display purely hydrophobic characteristics. Consequently, there has been a gradual shift in focus within LB research towards investigating such hydrophobic molecules. The recent upsurge in interest in this area is propelled by the diverse potential applications rising from the optical and electrical properties of these films, alongside their facile functionalization and enhanced physical properties.

The absence of hydrophilic headgroups presents a challenge regarding the stability of Langmuir monolayers formed by such non-amphiphilic molecules at the A/W interface. The general understanding is that the presence of a polar head group in amphiphiles is crucial for anchoring the molecule to the water surface, while attractive forces between the long-chain tails drive their self-assembly. However, with non-amphiphilic molecules, monolayer stability at the A/W interface may be achieved due to entropic considerations. The interplay between van der Waals and hydrophobic interactions could potentially contribute to stabilizing the monolayer in such cases.

The advancements in the material science research and employment of carbon nanostructures in wide variety of applications, led to its investigation in 2D systems. Carbon nanostructures such as CNT and graphene, even they are completely hydrophobic have been found to be able to form somewhat stable monolayer at the A/W interface. The ultrathin LB film of CNT have been extensively studied from fundamental and application point of view. Pristine-CNT are often dispersed in organic solvents like N-Methyl-Pyrrolidinone (NMP) and Dimethylformamide (DMF), for the formation of Langmuir film at the

A/W interface. However, due to strong van der Waals attractive forces between the nanotubes, the pristine-CNT gets agglomerated on the water surface. To overcome this, functionalization of the CNT with organic ligands is preferred. Functionalized CNT can easliy be dispersed in organic solvents like dichloroethane (DCE) or chloroform, which are ideal for dispersing on the water surface and for the formation of stable Langmuir film. The stable Langmuir film of functionalized CNT ensures good quality LB film for any device fabrication. In a study conducted by Valli et al.[44], LB technique was employed to achieve a well-organized structure of CNT bundles on different substrates. They further showcased the application of these organized CNT bundles as photo cathodes in a photoelectrochemical cell. Choi et al.[45] proposed a single-walled CNT patterning technique, achieved through soft lithography and the LB method. They suggested potential applications of the patterned CNTs for wide applications such as flexible high-speed transistors, high-efficiency solar cells, and transparent electrodes. In recent times, LB film of CNT have also been employed for gas sensing and health monitoring applications. In a study, Abdulla et al.[46] have reported the formation of highly ordered ultrathin films of polyaniline-functionalized multiwalled carbon nanotubes (PANI/MWCNT)using the LB technique . The films exhibited enhanced sensing properties for ammonia gas. The surface functionalization of MWCNT with polyaniline allowed for an oriented assembly of nanotubes. The resulting LB films demonstrated exceptional sensitivity to NH3 due to direct electron transport and fast analyte diffusion through the oriented assembly. The findings suggest the potential for fabricating high-performance NH3 gas sensor arrays using this large-scale alignment technique. Penza et al.[47] proposed the fabrication LB film of cadmium arachidate functionalized SWCNT for a high frequency acoustic gas sensor with high sensitivity for acetone, ethylacetate, and toluene at room temperature

Recently, the focus of gas sensing has been shifted towards sensing volatile organic gases such as acetone, ethanol, hexane, ketanone, ammonia etc for healthcare diagnostics. Acetone being one of the important biomarker for diabetes in the human body. Acetone is measured in the exhaled human breath and based on the concentration of the ketonic group, diabetes can be monitored. Acetone molecules in breath are a byproduct of fat metabolism. As the liver metabolizes free fatty acids in the body, it converts them into AcetylCoA. Depending on glucose levels, AcetylCoA can undergo enzymatic degradation, leading to the formation of acetone. Due to its small size, acetone easily enters the bloodstream and diffuses into the air spaces of the lungs. Therefore, acetone is expelled from the body through exhaled breath, providing a measurable indicator of ketone production and thus glucose levels. The reported level of acetone in human breath for diabetic patient is above 1.8 ppm. According to the recent WHO report; the prevalence of diabetes has witnessed a concerning escalation, surging from 108 million individuals in 1980 to a staggering 422 million by 2024. The implications of this global health issue are profound, with diabetes emerging as a significant contributor to various complications including blindness, kidney failure, heart attacks, stroke, and lower limb amputation. Although there are several diabetes detection devices or mechanism such as blood glucose monitoring, urine testing and haemoglobin A1 test, but all the techniques are either invasive where blood/urine are extracted from the patient body, time taking, costly and fails to provide regular monitoring. Thus, monitoring acetone from exhaled breath proves to be safer, quick, inexpensive and non-invasive technique for the diabetes monitoring. There are several scientific reports available which have reported acetone detection for the potential employment as breath sensor in diabetes monitoring. Fan et al.[48] reported acetone sensing for diabetes monitoring using thin film of Co_3O_4. The proposed resistive sensor showed best performance in the range of 1-50 ppm at 200°C. Salehi et al.[49] proposed SnO_2/Multiwalled CNT nanocomposite synthesized by ultrasonic-assisted deposition–precipitation method for acetone detection in exhaled breath for diabetes monitoring. They observed high dependency of humidity and due to formation of a hetero-junction at the interface between p-type MWCNT and n-type SnO2 semiconductor, sensitivity of acetone was enhanced. They observed lowest detectable concentration of 0.5 ppm at 200°C. Similarly, there are other reports which have proposed sensing platforms for diabetes monitoring via acetone sensing.

However, low level detection of acetone at room temperature is still a major challenge. Most of the studies present on acetone detection are either performed at high temperature or resistive based measurements. The resistive based sensing mechanism are highly susceptible to humidity, temperature and high power consumption. The sensor utilizing ultrathin film of CNT are found to have high sensitivity, wider detectable concentration range, minimal response time at room temperature.

Graphene is another important hydrophobic carbon nanomaterial which has been extensively studied. Since its discovery in 2004, exploration and advancement in the graphene related system have presented numerous potential applications[1, 50]. The LB films of graphene are particularly significant due to their ability to control alignment, high surface-to-volume ratio, and tunable properties. Furthermore, the characteristics of graphene can be customized by altering their composition and structure. Applications of LB films composed of graphene span across diverse fields including electronics, sensors, catalysis, energy storage, and optoelectronics, offering adaptable solutions to various challenges. Li et al. [51] proposed a technique for the fabrication of high-quality single-layer graphene sheets (GS). The process commenced with the exfoliation of commercial graphite, followed by intercalation with oleum and tetrabutylammonium hydroxide (TBA). The intercalation expanded the gaps between graphene layers which can lead to the production of GS with a stable suspension in organic solvents, exhibiting remarkable electrical conductivity at both ambient and cryogenic temperatures. Additionally, the authors have demonstrated the layer-by-layer assembly of large transparent conducting films of GS using the LB technique. These GS films displayed high transparency (93 %) and low resistance (8 kΩ) at room temperature for the potential application in transparent conductive films and solar cells. Furthermore, the LB film of SnO_2/graphene oxide nanocomposite showed potential as anode materials in Li-ion batteries [52]. In this approach, graphene oxide layers were transferred onto copper foil deposited with SnO_2. The resulting nanocomposites were employed as anode materials in Li-ion batteries, demonstrating impressive energy storage capacities, with an initial discharge capacity of 1091 $mAhg^{-1}$. The columbic efficiency remained stable at 62.5% after 20 cycles, indicating good cyclic stability. The ordered layer architecture of the nanocomposite contributed to enhanced storage capacity and stability, highlighting the effectiveness of the LB method in electrode fabrication for energy storage devices. The ultrathin LB graphene film has also been widely used in biosensing applications. Poonia et al. [53] fabricated monolayers of acid-terminated graphene (G-COOH) and utilized them for urea sensing. The LB film of G-COOH exhibited a significantly lower detectable concentration of urea (8.3 μM) compared to the spin-coated film (41.6 μM). Sensitivity measurements, conducted using a quartz crystal microbalance, revealed that the LB film displayed approximately three times higher sensitivity (42.5 ng/cm^2/ μM) than the spin-coated film (12.9 ng/cm^2/ μM). The same sensing protocol applied to detect urea in milk showcased approximately five times greater sensitivity with the LB film of G-COOH compared to the spin-coated film, highlighting its potential as an extremely sensitive urea sensor capable of detecting low concentrations.

Apart from the conventional sensing related studies, the LB film of graphene can potentially be employed for water quality monitoring. In the second world countries, the potable drinking water has many impurities such as heavy metal ions, industrial effluents, pesticides, pathogen and bacteria. Due to the presence of such impurities, huge risk persists on the population in this region. Biosensors based on bacterial detection in potable water has experienced exponential growth in recent years. Globally, bacterial contamination in water remains a primary cause of hospitalizations and fatalities [54, 55]. Despite ongoing efforts, the annual reduction in deaths attributed to pathogenic bacterial infections stands at only 1%, with a projected 13 million deaths by 2050[56]. Additionally, the potential use of pathogenic bacteria as biological weapons is a significant concern in the scientific community[57, 58]. Therefore, there is a great need for cost effective, reliable and efficient sensing platform for pathogens.

The LB film of graphene offers high surface to volume (S/V) ratio and precise control over the thickness and morphology of the graphene film, allowing for tailored sensor designs optimized for specific analytes. The surface π electrons in ultrathin films of graphene interacts with the bio-membrane of the pathogens. The bio-membrane of pathogens includes proteins and nucleic acids which contain aromatic amino acids. These aromatic rings interact through $\pi - \pi$ stacking with the aromatic rings of graphene. These interactions alter the physical properties of the graphene film, which is suitable for measurement during bacteria sensing. The LB films of graphene can also be integrated into compact and portable devices due to their small size and low power requirements. This miniaturization allows for rapid detection in remote or resource-limited areas.

Numerous reports are available based on water borne pathogen detection from graphene as a functional layer. However, to achieve selective detection using graphene as a functional layer, the layer was further modified with antibody of the pathogenic bacteria to be detected. In a report by Karuppiah et al. [59], a label-free biosensor for the detection of Escherichia coli (E. coli) in water using screen-printing paper electrode of nanoarchitectured graphene oxide (GO) was proposed. The graphene coated electrode was immobilized with Concanavalin A (ConA) lectin as a biorecognition element. The performance of the biosensor was evaluated in real water samples, including sludge and beach water, using electrochemical impedance spectroscopy (EIS). The charge-transfer resistance of GO-ConA exhibited a linear increase with bacterial concentration within the range of 10–10^8 colony forming units milliliter $^{-1}$ (cfu mL^{-1}), achieving a limit of detection (LOD) of 10 cfu mL^{-1}. Similarly, Hernandez et al.[60] introduced a potentiometric aptasensor utilizing chemically modified graphene oxide (GO). GO and reduced graphene oxide (RGO) served as the foundation for constructing two versions of the aptasensor for detecting complex microorganisms like Staphylococcus aureus (S. aureus). DNA aptamers were covalently attached to GO and non-covalently to RGO. Both systems achieved selective detection of a 1 cfu mL^{-1} of S. aureus in near real-time assays. RGO-based aptasensors exhibits lower noise levels compared to those made with GO. These novel aptasensors offer ultra-low detection limits and rapid response times for microorganism detection. Thus, functionalization plays a crucial role in selective sensing. By modifying the surface of graphene with specific functional groups or biomolecules, researchers can tailor the sensing platform to enhance the selectivity. Overall, LB films of graphene combined with appropriate functionalization strategies can promise opportunities for the development of highly sensitive, label free and selective bacteria sensors. These sensors are useful in environmental monitoring, public health, and water quality assessment. While there are many reports on bacteria sensing using graphene as a functional layer and further modified with aptamers and DNA. The LB-fabricated functionalized graphene sheets have not been significantly explored for bacteria sensing. Based on the type of functionlization, these ultrathin film of graphene has the potential to be employed for wide range and selective detection of pathogens.

With the developing technology, sensing techniques have also evolved. There are several transducers available which works on different type of measurements such as electrochemical, capacitive, resistive, optical, piezoelectric, magnetic and calorimetric. Each method has their own advantage and application. However, optical methods of detection offer high precision and the label-free concept. Optical biosensor platforms leverage inherent optical properties of biomolecules, enabling precise and direct detection without the need for additional labeling steps. This label-free approach streamlines assay procedures, reduces experimental complexity, and minimizes the risk of assay interference or artifacts.

Among the various optical techniques like surface plasmon resonance (SPR), absorbance, photoluminescence, and surface-enhanced Raman spectroscopy, SPR emerges as the next generation of sensing devices for widespread applications. SPR stands out as a optical phenomenon in bio-sensing and bioanalysis due to its label-free detection capability with exceptional sensitivity and resolution. Typically employed as a refractive index (RI) measurement technique, SPR can detect the adsorption of even minute quantities of analytes on the active area of sensor. In 1983, Liedberg et al.[61] group was the first to identify SPR for biosensing application. They proposed the sensing mechanism for antibody based detection of different Immunoglobulins. They reported the lowest detected concentration in nanomolar range. Chang et al.[62] proposed zinc oxide coated gold films for the detection of breast cancer markers using SPR. Carbohydrate antigen 15.3 (CA15-3), a tumor marker for breast cancer, was chosen as a model analyte. They tested samples with concentrations ranging from low to high and found a strong response in the linear range from 1 to 40 units per milliliter, with a very low detection limit of 0.025 units per mL.

Compared to traditional gold/chromium layers, a significant improvement in signal intensity and sensitivity was observed. Chabot et al.[63] proposed the combination of living cells and SPR to monitor the effects of different molecular stimuli on cellular activity. Several metallic layers, including silver, copper, aluminum, and gold, have been explored for SPR measurements. Nonetheless, gold stands out as the predominant choice as it offers several practical benefits, such as chemical inertness, easy functionalization, and excellent stability in aqueous environments. Several reports have reported functionalization of gold surface for enhanced and selective detection of bioanalytes. However, the pure gold surface has a lower affinity towards many bio-analytes. Further, sensing utilizing SPR rely on various factors, including appropriate functionalization of the active area and optimization of optics[64]. To improve the specificity and sensitivity of the sensor, the gold surface is functionalized with bio-affinitive layers such as graphene. The extended π electron system of a graphene sheet increase the binding affinity with bio-analytes via $\pi - \pi$ interactions. Wu et al.[65] reported that the functionalization of gold layer with single layer graphene has enahnced the sensitivity upto 3-4 orders of the magnitude. While functionalization can enhance analyte adsorption capabilities, it diminishes the figure-of-merit (FOM). Moreover, the weak physical bonding between metal and bio-affinitive layer decrease the device stability[66]. The functionalization also increases the thickness of the active layer of the SPR configuration which can hinder the interaction between the plasmonic waves and analytes which will reduce the device performance.

Several fundamental issues are also present due to the functional layer which can alter the SPR response. The density and relative tilt of molecules of the functional layer over the metallic film alters the SPR responses. Some of the fundamental issues are listed:

- **Anisotropy in the functional layer:** SPR measurements are highly sensitive to even a minute change of refractive index even in the order of $10^{-8} RIU$. The refractive index can be altered by minimal perturbation due to ordering and alignment of the molecules in the functional layer. In case of ultrathin film of anisotropic materials, the refractive index is found to be different in orthogonal directions. SPR is a tool for measuring RI at a very high precision. The measurement of RI using SPR is dependent on the relative angle between the plane of incidence and plane of anisotropy of the functional layer. As a result, reference measurements are extremely difficult. Thus, it is essential the study the electric field pattern of the plasmonic field and its dependencies on different degrees of anisotropy of the thin film.

- **Surface density of the functional layer:** In the ultrathin film regime functional layer do exhibit non uniformity in terms of defects. Such layers can be considered as sub-monolayer. Functional layer of metallic nanoparticles often have been used to increase the sensitivity of the SPR[67]. Metallic nanoparticles induce localized surface plasmons to enhance the sensitivity and increase the FOM of the SPR. However, the deposition mechanisms employed for deposition of such metallic nanoparticles on the SPR chip often fails to deposit a homogeneous layer. The deposited layer are rather in sub-monolayer regime with number of defects. Therefore, it is of importance to investigate the sub-monolayer with different surface coverage of the SPR chip. Other functional layers which have high affinity towards bio analytes are also to be investigated with respect to the surface density and alignment. In this thesis we have investigated the effect of surface density and the alignment of single walled CNT on the SPR response.

In SPR, several reports have suggested the deposition of active functional layer over the metal surface to enhance the sensitivity and selectivity of the bio sensor. However, there are several issues are need to be addressed before employment as SPR based sensing platform. The major issue is the thickness of the functional layer and its biocompatibility. The films of bio-ligands which are used for functionalization are usually very thick. The thicker layer are less sensitive towards the adsorption of analytes when measured using SPR. Therefore, it is essential to explore a functional layer which can generate plasmonic field and act as a good biocompatible layer. Graphene being one such material that has shown to be effective as good bio affinitive layer. Further, it can also generate plasmonic field in terahertz regime[68]. The group of Thomas et al.[69] have studied the generation of surface plasmon waves in graphene layer. They proposed an all-optical plasmon coupling scheme to generate surface plasmons in a planar graphene sheet. They used frequency wave mixing to match both the wavevector and energy of the surface wave. Further, by controlling the phase matching conditions, they proposed graphene layer can excite surface plasmons with a defined wavevector and direction across a large frequency range. In an another article by Maleki et al.[70], the authors have proposed a gas sensor based on double layer graphene nanograting fabricated over a dielectric substrate. They were able to observe the device sensitivity of 430 nm/RIU for incident radiation of wavelength in the range of 1–2 μm. Thus, employment of graphene as both plasmon generation layer and active layer for bio sensing is an interesting avenue to investigate. The employment of graphene as plasmonic and bio affinitive layer requires the in depth understanding of the optical and electronic properties of graphene. The optical property of graphene is dependent on the unique electronic structure, which further depends on the stacking of the graphene layers. In single layer configuration graphene has linear band structure. Interestingly in the bilayer configuration, the band structure changes. In the past few years, in plane twisting of the bilayer graphene has added another dimension in the study of graphene systems[71]. The twisted bilayer graphene (T-BLG) structure with a relative in-plane twist between the two layers has a very complex band structure[72]. The band structure and the optical properties of T-BLG are dependent on the relative in-plane twist angle. Based on the in plane twist between the graphene layers the interlayer interaction changes the optical properties. Thus, it will be interesting to investigate the incorporation of twisted bilayer graphene systems for different twist angles in SPR for biosensing. In this thesis, we have studied the dependency of sensitivity on the various relative in plane twists.

1.5 Research gap and Objective

The main motivation behind the thesis is to investigate the realm of A/W and A/S interface for various sensing applications. Metal oxide sensors are commonly used in gas sensing research as they exhibit better sensing responses. However the sensing response of such metal oxide sensors are best at higher temperatures. On the other hand, current research suggests that CNT used in gas detection can provide excellent accuracy and operational efficiency even at room temperature. In the past few years volatile gas detection such as acetone has been one of most important areas of research due to its application in diabetes monitoring via human breath analysis. However, the available breath analyzer either support low level detection or room temperature detection. Most low level detectors working with metal oxide based sensors have high operating temperature. The available room temperature sensors lack low level detection of acetone with high accuracy. Also the commonly proposed parameter is usually resistance which is a highly temperature dependent parameter. Therefore, the need of the scientific community is to have sensing platform operating at room temperature and offers low level detection with high accuracy.

The another area of research that has garnered huge attention in the scientific community is detection of pathogens in food/water. The pathogens have been one of the major cause of death in developing parts of the world. The available sensing mechanism for pathogen detection are label based, expensive and time taking. Thus, rapid and label free and point-of-care sensing platform is required.

Biosensors based on optical techniques have gathered attention for their label free and highly sensitive measurement. One of the major techniques for biosensing and bio-anlaysis is based on SPR. The SPR phenomenon is extremely dependent on the nature of the functional ultrathin film. The SPR phenomenon for the anisotropic ultrathin film with varying surface density and alignment have not been studied. These parameters are essential for assessing the quality of SPR based sensing device.

In typical SPR-based biosensors, graphene is often used to enhance the sensitivity. However, while sensitivity improves, the FOM decreases. The weak binding between gold and graphene affects the lifetime of the sensing platform. Therefore, there is a need to explore a system where FOM and bioaffinity remains high in SPR-based biosensors. Thus, investigating graphene as both a plasmon-generating layer and a biorecognition element is essential for future advancements in SPR-based biosensors.

1.6 Outline of the Thesis

In this thesis, we report our studies on nanomaterials at the A/W and A/S interfaces. We present our investigation on some major sensing applications of the ultrathin film deposited at extremely controlled condition. Primarily we have performed the sensing application of acetone and bacteria. We also addressed some of the major practical issues related to sensing using SPR phenomenon.

Chapter 1 introduces the system and present a comprehensive literature review of the topic. The research gap and objective of the thesis have been discussed.

Chapter 2 presents the methodologies and experimental techniques used in the thesis.

In chapter 3, we proposed a sensing mechanism for acetone sensing, focusing on the utilization of ODA-CNT as ultrathin LB film and drop cast film. The sensing measurement was performed using impedance spectroscopy and several parameters were recorded as function of frequency. Among the different other parameters, capacitance is found to be most suitable. We report limit of detection (LOD) of 0.5 ppm and wider detectable concentration range (1-300 ppm) at room temperature.

In Chapter 4, we report the detection of pathogenic bacteria which are commonly available in food/water. We have employed LB film of ODA-functionalized graphene to identify different types of water-borne bacteria. The chapter investigates the selective response observed for E. coli and demonstrates the use of machine learning algorithms for improved analysis. Importantly, the sensing platform shows a very low LOD of 2.5 cfu/mL.

In, chapter 5, we have investigated the role of optical anisotropy and surface density of the ultrathin functional layer on the SPR measurement. The ultrathin film of various thickness and different in-plane birefringence was studied using FDTD method and a calibration plot was proposed. Further, the calibration plot was employed to predict the in-plane birefringence values of ultrathin LB film of cadmium stearate (CdSA) and octylcyanobiphenyl (8CB). Further, we investigated the effect of surface density of nanoparticles in the functional layer on SPR response. We employed silver nanoparticles and single walled CNT for our investigation. Interestingly, we found insulator-metal transition at surface coverage $\geq 40\%$. In case of CNT, the SPR response was found to be alignment dependent. In parallel alignment of CNT, the 2D plasmonic field showed response similar to that of metallic film whereas in perpendicular alignment, we observed a stratified field response.

In chapter 6, we have proposed the utilization of graphene as the dual purpose layer in SPR. Graphene can be employed as plasmon generating layer as well as the bio-recognition layer. We investigated the plasmonic characteristics of monolayer, bilayer, and twisted bilayer graphene (MLG, BLG and T-BLG) systems, demonstrating their capability to generate plasmonic fields in the terahertz frequency range. Graphene exhibits strong bio-affinity, enhancing its potential for sensitive biological material detection. The thesis evaluates the sensing performance of MLG, BLG and T-BLG systems, with twisted bilayer graphene near the magic angle showing the highest sensitivity of 29120 nm/RIU due to strong interlayer coupling.

In chapter 7, we conclude the thesis work and present the future scope of the thesis.

CHAPTER 2

Methodology

This chapter outlines the methodology employed for the study of ultrathin films at A/W and A/S interfaces. It includes both experimental and simulation techniques used to study the ultrathin films.

2.1 Experimental Technique

2.1.1 Surface Manometry

Molecular interactions at the interface between the amphiphilic molecule and underlying water molecules plays a crucial role in stabilizing the interface. Due to the interaction, the surface tension and surface Gibbs free energy of water reduces. Surface tension is measured through the Wilhelmy method, which involves employing a plate at the A/W interface connected to a balance. The plate is usually made up of hydrophilic material, such as filter paper, mica, or platinum to achieve a null contact angle. Filter papers are particularly advantageous as they rapidly saturate with water. The Wilhelmy equation is then employed to calculate the surface tension γ.

$$\gamma = \frac{F}{l cos\theta} \tag{2.1}$$

Here, F represents the force exerted by the surface, pulling the plate downward while excluding the mass of the plate. The parameter l denotes the wetted perimeter of the contact line between the interface and the plate, with no consideration for the buoyancy of the plate in contact with water. The angle θ signifies the contact angle between the water phase and the plate. As the molecules are dispersed at the A/W interface, the subphase exerts a comparatively weaker force on the molecules, which leads to a reduction in the surface tension of water. The reduction in the surface tension is measured as surface pressure (π). This surface pressure is analogous to the force exerted by the surface along its perimeter. Surface pressure is proportional to the reduction in the surface tension of water due to the addition of amphiphilic molecules, therefore it is defined as:

$$\pi = \gamma_o - \gamma \tag{2.2}$$

γ_o is the surface tension of the pure water, and γ is the surface tension of the water in the presence of the amphiphilic molecules. Surface manometry is the technique used to measure surface pressure as a function of surface density at a given temperature.

The investigation of Langmuir monolayer at the A/W interface requires an inert container known as Langmuir trough. Ideally, the Langmuir trough is hydrophobic which is easy to clean and capable of withstanding both organic solvents and inorganic acids. The most commonly used material is polytetrafluorethylene (PTFE), usually called Teflon. The monolayer formation at the interface highly depends on the purity of the subphase (water) and the trough. Thus, a frequent and thorough cleaning procedure is employed. The trough is repeatedly cleaned with chloroform and de-ionized water.

Further, a stock solution of the molecule is prepared in an appropriate volatile solvent. The solvent must have a positive spreading coefficient Sc, defined as:

$$S_c = \gamma_{w/air} - \gamma_{s/air} - \gamma_{w/s} \tag{2.3}$$

where, $\gamma_{w/air}$, $\gamma_{s/air}$ and $\gamma_{w/s}$ are the interfacial tensions for the air/water, organic solvent/air, and water/organic solvent, respectively. The surface Gibbs free energy at the interface of area A is γA, and as the organic solvent starts covering the water surface, the interfacial tension ($\gamma_{s/air}$ and $\gamma_{w/s}$) decreases allowing for spontaneous spreading. The most commonly used solvents are chloroform and acetone. In certain cases if the molecules are not soluble in such solvents, other appropriate solvents such as ethanol and dimethylformamide (DMF) can be used.

The solution of such molecules in the volatile solvent is spread at the A/W interface using a micro syringe (Hamilton). The system is then left undisturbed for some time to allow the solvent to evaporate. As the solvent is completely evaporated, the molecules homogeneously spread over the interface and form a mono-molecular two-dimensional film.

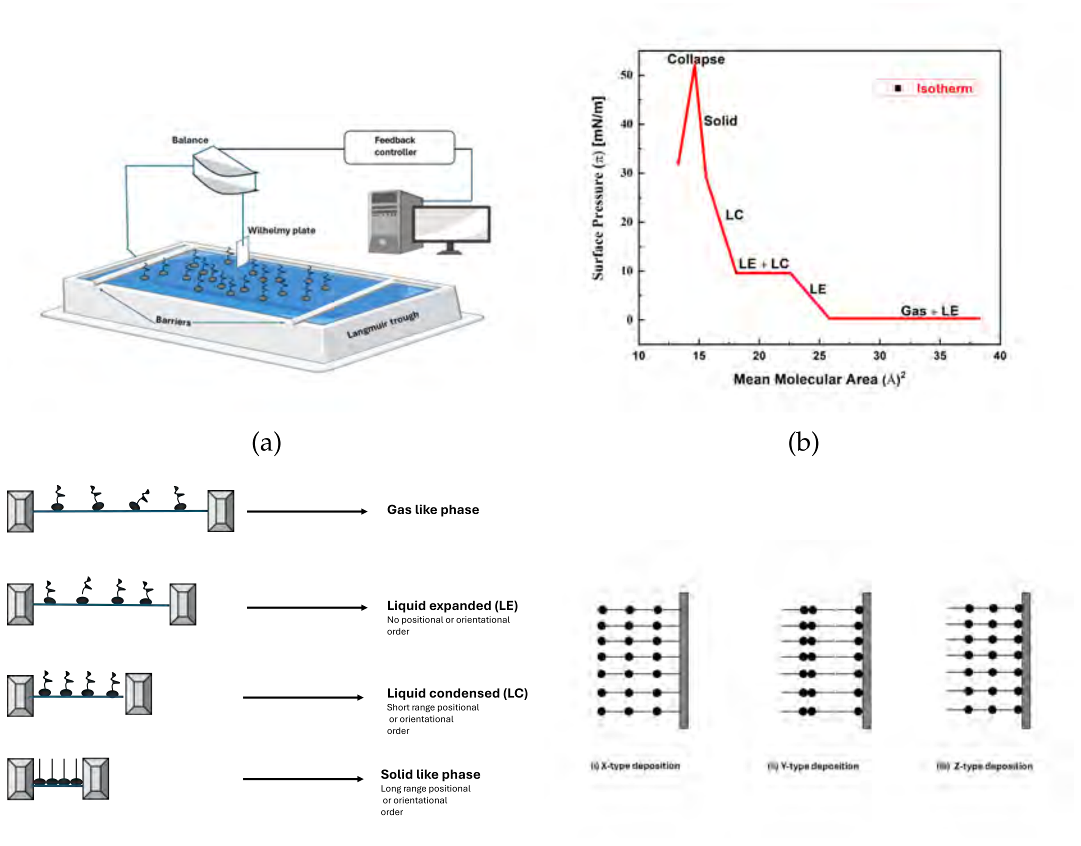

(a) (b)

(c) (d)

Figure 2.1: Schematic of (a) conventional Langmuir trough, (b) Isotherm of Langmuir monolayer, (c) possible arrangements of the molecules at the interface at different surface phases and (d) different types of multilayer in LB film.

In a Langmuir trough, barriers made up of Teflon slide across the trough to compress or expand the monolayer at the A/W interface. When the available area for the molecules is sufficiently large, the monolayer will spontaneously expand, resulting in negligible interactions between the molecules. This state is known as the gas-like phase.

Fig:-2.1 (b) shows the schematic of surface pressure-area isotherm. The kink and the plateau regions indicate the phase transition. The plateau regions Fig:-2.1 (b) signify the first order phase transition with the coexistence of two phases (here, LE and LC). The kink represents weak first order phase transition. The possible arrangement of molecules in different phases are shown in Fig:-2.1 (c). As the Langmuir film is compressed using the mechanical barriers, the area per molecule decreases and the molecules begin to interact. The monolayer transforms from gas to liquid expanded (LE) phase. The molecules in LE phase do not possess any positional and orientational order. On further compression the LE phase transforms into liquid condensed (LC) phase followed by a solid-like phase. The molecules exhibit short range positional and orientational order in LC phase and quasi long range positional and orientational order in solid-like phase. On further compression the monolayer destabilizes and goes to collapse state.

The identification of physical states and phase transitions in a Langmuir monolayer can further be described by a parameter known as the in-plane isothermal elastic modulus (E).

$$|E| = \left| -\frac{1}{A}\frac{d\pi}{dA} \right| \tag{2.4}$$

The parameter E reflects the elastic nature of the monolayer and reveal the weak phase transitions in the Langmuir monolayer at the A/W interface. Based on the values of the in-plane elastic modulus, the phases of Langmuir monolayer can be identified. The E value is the range 0-10 mN/m, 10-50 mN/m, 50-250 mN/m and above 250 mN/m may indicate a gas-like phase, liquid-like phase, liquid-condensed phase, and solid-like phase, respectively.

2.1.2 Brewster Angle Microscopy (BAM)

BAM is used to obtain a more comprehensive understanding of phase transitions in Langmuir monolayer at the A/W interface. BAM serves as an ideal technique for the non-destructive imaging of Langmuir monolayers at the A/W interface. This method facilitates real-time examination of phase transition, any optical anisotropy, and domain formations. The working principle of BAM is based on Brewster's law. The p-polarized light source is directed towards the water surface at the Brewster angle for A/W interface, resulting in zero light reflection and capturing a dark background image by the detector camera. Subsequently, any molecular domain entering the region of incident light due to monolayer compression causes a shift in the refractive index, leading to a deviation from the Brewster angle. Thus, the light gets reflected from the interface which can be collected by the detector to provide the image of the monolayer. The intensity observed in BAM is influenced by various factors, including surface density, molecular orientation, and film thickness. In this thesis, we have employed KSV NIMA Micro-BAM to observe the Langmuir monolayer phases and domain formations. The instrument is equipped with a monochromatic laser of wavelength 659 nm and power 30 mW. The resolution of the BAM images is 12 μm.

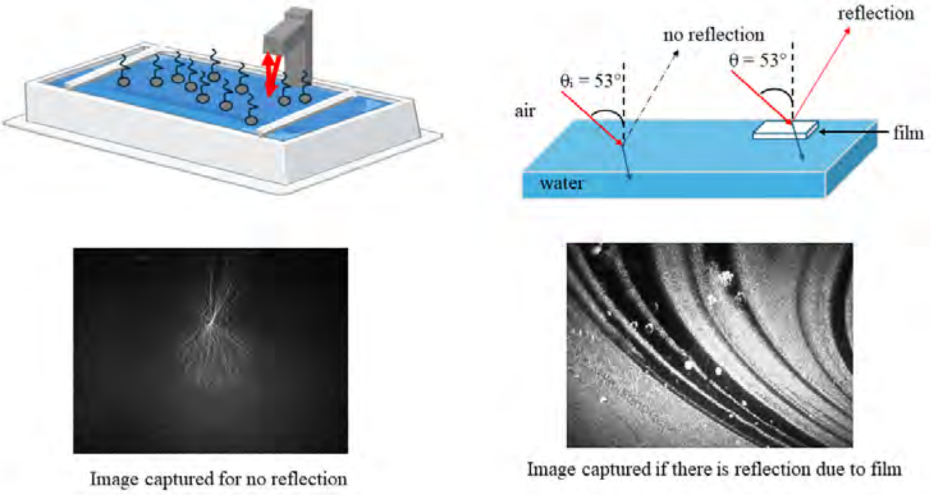

Image captured for no reflection

Image captured if there is reflection due to film

Figure 2.2: Schematics of a Brewster angle microscopy. BAM image captured for (c) pure water surface and (d) monolayer domains. The size of the image 3.6 mm × 4 mm.

2.1.3 Langmuir-Blodgett and Langmuir-Schaefer technique for ultrathin film deposition

Katherine Blodgett introduced the technique of transferring Langmuir monolayers from A/W interface onto solid supports[8, 9]. This process involves vertical movement of the substrate through the insoluble monolayer at the A/W interface. This vertical dipping mechanism is termed as Langmuir-Blodgett (LB) technique (Fig:-2.3). In LB technique, the choice of substrate for the transfer of the monolayer is significant, as it influences the adhesion of the monolayer to the solid surface. The standard transfer procedure for the first layer includes compressing the Langmuir monolayer to a target surface pressure and withdrawing the hydrophilic substrate from the aqueous subphase. In the case of hydrophobic substrate, the transfer process begins by immersing the substrate from air to the subphase. The multilayer can be deposited by the immersion or emersion of the substrate repeatedly. The dipping speed of the substrate was kept at 1 mm/min for the entire work. The surface pressure decreases during transfer due to material loss from the liquid interface to the solid interface. The feedback mechanism controls the target surface pressure by the lateral movement of the barriers to ensure successful deposition. The transfer ratio (Eq:-2.5) indicates the decrease in the monolayer area divided by the covered solid support area. Transfer ratios close to one indicate uniform transfer.

$$Transfer\ ratio\ (TR) = \frac{Area\ of\ the\ monolayer\ transferred}{Area\ of\ the\ substrate} \tag{2.5}$$

The success of LB film transfer relies on various factors, including molecular interaction, subphase composition (including pH and ionic strength), dipping rate, substrate, and target surface pressure. These parameters influence the structure of the transferred layer. While the first monolayer is usually easy to transfer, the deposition of subsequent layers depends on the nature of interaction between the molecules and the substrate. Weak adhesion may result in the removal of a previously transferred monolayer from the substrate, leading to a negative transfer ratio.

The ultrathin film can also be transferred via Langmuir–Schaefer (LS) technique. In this method, a hydrophobic substrate is allowed to touch the Langmuir monolayer from air medium. Due to hydrophobic interaction a single layer is transferred onto the substrate. Multilayers can be transferred by repeated touching and lifting the substrate. In such transfer the interaction between the substrate and the molecules plays a crucial role.

It is expected that the transferred LB/LS films retain the alignment or tilt of the molecules present in a given phase at A/W interface. The characterization and spectroscopic measurements can be performed on the transferred films

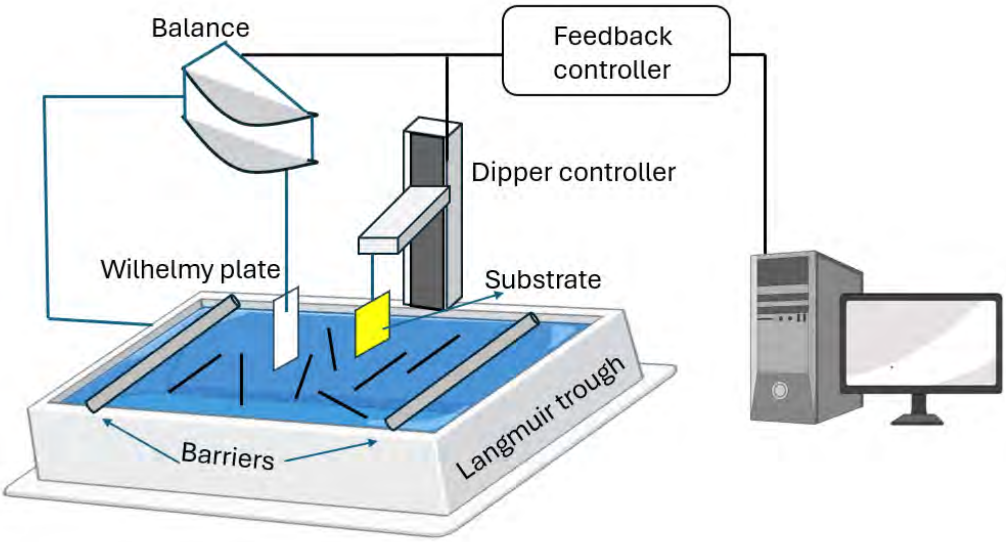

Figure 2.3: Schematic of a Langmuir-Blodgett deposition technique.

to understand the molecular architecture. In this thesis we have employed the KSV NIMA LB trough for the study of Langmuir monolayer at the A/W interface and deposition of ultrathin films .

2.1.4 Characterization Techniques

2.1.4.1 Field emission scanning electron microscopy (FESEM)

FESEM is a powerful imaging technique used in nanotechnology and materials science to achieve high-resolution images of samples. Unlike traditional optical microscopes, FESEM utilizes electrons instead of light for imaging, allowing for much higher magnification and resolution. It has ability to achieve nanoscale resolution due to its small wavelength, allowing it to overcome the diffraction limit of light. In this process, a strong electric field (0.5 kV to 30 kV) is applied to the tip (diameter $\sim$ 10-100 nm) of field emission gun which high density of electrons. The emitted electrons are then accelerated towards the sample surface by an electric field. The electron beam can be maneuvered using electromagnetic lens. The emitted electrons propagate through high vacuum ($\approx\ 10^9\ Torr$) in the microscope column for imaging. As the electron beam scans across the sample, interactions occur between the electrons and the

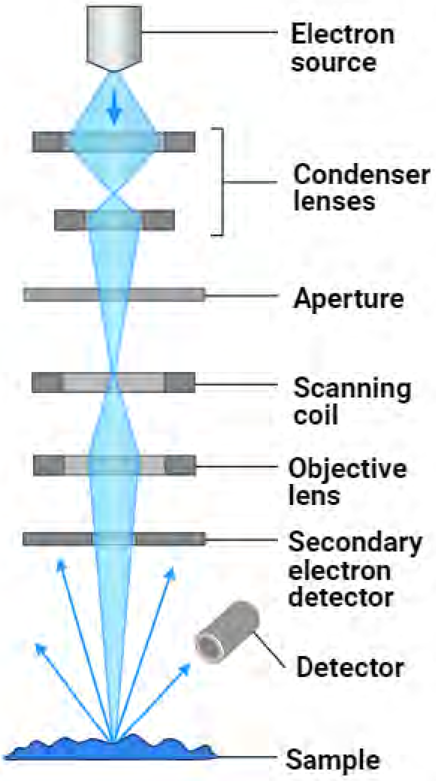

Figure 2.4: A schematic of field emission scanning electron microscope.

atoms in the sample. Due to such interactions there are emission of secondary electrons, backscattered electrons and Auger electrons. For high resolution images normally secondary electrons are detected. The emission of X-ray can be used for elemental analysis. Moreover, the electron beam can be precisely controlled, enabling the acquisition of images from various angles to create three-dimensional reconstructions of the sample. FESEM is particularly suitable for studying materials with intricate surface structures, such as nanoparticles, biological specimens, and advanced materials. It provides insights into surface morphology, particle size distribution, and composition.

We have used FEI Apreo LoVac FESEM instrument manufactured by Thermo-Fisher. It has a retractable STEM3+ detector and DBS detector along with Aztec standard EDS system having a resolution of 127 eV. Before imaging, a thin layer of gold is coated on the sample using Leica ultra microtome EM UC7 sputtering unit to avoid accumulation of charges and to improve the contrast of the image. A schematic of FESEM showing its major components is shown in Fig:-2.4.

2.1.4.2 X-ray diffraction

X-rays scattering methods provide valuable information about the arrangement of atoms/molecules within a material and are widely used to study the structural properties of ultrathin films. The thickness of the ultrathin LB films are of the order $1 - 10\ nm$. Therefore, the electron density for scattering x-rays is very low. Thus, high intense X-ray source is needed to probe the ultrathin film. The scattering interaction can be further improved by incidenting the X-ray beam at grazing angle ($\sim\ 0.4^\circ - 1^\circ$)[73, 74]. We have employed Rigaku Smart Lab II X-ray diffractometer with Cu-kα as the X-rays source with wavelength of 0.154 nm. It has as 3 kW sealed X-ray tube with CBO optics and a D/teX Ultra 250 silicon strip detector.

2.1.4.3 Grazing incidence X-ray diffraction (GIXD)

GIXD requires a very high intense x-ray beam which is incident on the sample slightly above the critical angle, typically around 0.2 °. At grazing incidence the evanescent waves penetrate into the interface just a few monolayers deep. Consequently, this wave interacts and scatters off the LB film. Such scattering events lead to diffraction patterns which can be analyzed to get the structural information. In ultrathin LB films, periodic structures are absent along the normal to the surface plane (the z-direction). Consequently, constructive interference of scattered waves cannot occur in this direction. However, diffraction can occur within the surface plane (the xy-plane). In LB films, the domains with unique orientations and structural patterns are present in the parallel (x-y) plane of the substrate; therefore in-plane diffraction measurements are usually performed for LB monolayers. However, monolayers do not truly represent homogeneous two-dimensional (2D) systems. In most cases, they are composed of long-chain molecules, and the orientation of these chains plays a significant role in the diffraction phenomenon. When the chain axes align perpendicular to the surface, diffraction spots are positioned within the xy-plane. However, if the chains deviate from the normal orientation, the diffraction spots shift along the z-direction. The magnitude of this shift can be employed as a measure to calculate the tilt angle of the chains. The diffraction patterns from LB films can be observed by scanning with a position sensitive detector and collimator aligned normal to the film plane.

2.1.4.4 X-ray Reflectivity (XRR)

For X-ray, medium other than vacuum or air, the refractive index is less than unity. Thus, there is a phase shift of 180° in the Thompson scattering of X-ray. Hence, X-ray show total external reflection from any flat material surface for a glancing angle below the critical angle. It results in total external reflection with no penetration of the X-ray into the film. Thus, XRR is an efficient characterization technique for studying the surfaces of ultrathin films fabricated using LB technique. The incident angle is varied based on the electronic density of the material. A higher incident X-ray angle relative to the critical angle results in a deeper penetration of X-ray into the material. In the case of a material with an ideally flat surface, reflectivity experiences a sudden decrease at angles beyond the critical angle. Also, if the ultrathin films have high surface roughness, there is a higher chance of reduction in reflectivity. When a substrate is uniformly coated with another material possessing a distinct electronic density. The reflected X-ray from interface between the substrate and the thin film and the free surface of the thin film can either constructively or destructively interfere, leading to the emergence of an oscillation pattern in data. The intensity scattered by the sample interface is directly related to the square of the modulus of Fourier transform of electron density. Consequently, the electron density profile can be inferred from the measured intensity pattern, facilitating the determination of both vertical properties (layer thicknesses) and lateral properties (roughness). Similarly, the film thickness can be derived from the periodicity of the oscillation in data, while information regarding the surface and interface is obtained from the angular dependency of the amplitude of the oscillation pattern. For multiple interface system such as ultrathin film deposited on a substrate or multilayer system on a substrate, the X-ray reflectivity is calculated using Parrat's formalism[75]. According to Parrat's formalism, the electric field vectors of the incident, reflected and refracted X-ray beam at any grazing incidence angle θ at a distance z perpendicular to the interface can

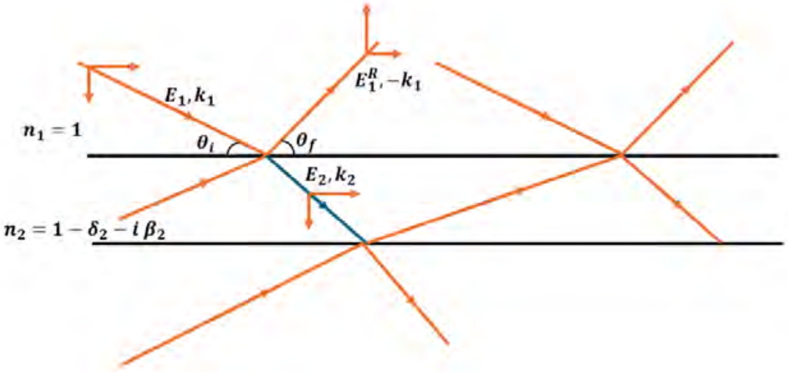

Figure 2.5: Graphical representation of X-ray reflectivity and transmission at any interface. A plane X-ray with electric field E_1 with wave vector k_1 is reflected from air-film interface at an incident glancing angle (θ_i) and leaving the surface at an angle (θ_f) with electric field vector E_1^R with wave vector $-k_1$. The transmitted wave passes through the film and reflects back from the film-substrate interface and finally comes out.

be expressed as

$$E_1(z_1) = E_1(0)exp[i\omega t - (k_{1,x}x_1 + k_{1,z}z_1)] \tag{2.6}$$

$$E_1^R(z_1) = E_1^R(0)exp[i\omega t - (k_{1,x}x_1 + k_{1,z}z_1)] \tag{2.7}$$

$$E_2(z_2) = E_2(0)exp[i\omega t - (k_{2,x}x_1 + k_{2,z}z_2)] \tag{2.8}$$

Where, $k_1 = \frac{2\pi}{\lambda_2}$, $k_2 = \frac{2\pi}{\lambda_2}$ are wave vectors in air and in the medium as shown in the Fig:-2.5.

Further, for the unpolarized X-ray region the Fresnel coefficient of reflectivity is defined as:

$$R_{1,2} = \frac{\theta - \sqrt{\theta^2 - \theta_c^2}}{\theta + \sqrt{\theta^2 - \theta_c^2}} \tag{2.9}$$

Where, θ is the incident angle and θ_c is the critical angle. Replacing the angle from wave vector and further solving for a thin film of finite thickness d (i.e two interfaces), Reflectivity is expressed as:

$$R_1 = \frac{R_{1,2} + R_{2,3}}{1 + R_{2,3}} \tag{2.10}$$

Where, $R_{1,2}$ and $R_{2,3}$ are the reflectivity from the air-film and film-substrate interface respectively. Applying Parrat's formalism and recursive relations in to the above reflectance from rough interface is expressed as:

$$R_{n-1,n} = R^F_{n-1,n} exp(-0.5 q_{n-1,z} q_{n,z} \sigma_n^2) \tag{2.11}$$

Comparing the experimental XRR profiles with the simulated profile(eq-2.11), in plane electron density and thickness can be calculated.

2.1.5 Sensing Techniques

2.1.5.1 Impedance Spectroscopy

Impedance spectroscopy (IS) is a valuable technique in gas sensing applications, offering a comprehensive analysis of the electrical behavior of gas-sensitive platforms. An alternating current is applied as a function of frequency, and resulting multiparameter output are measured. It provides insights into material properties like resistance and capacitance. This method allows for selective detection as different analytes uniquely alter the electrical characteristics. The real-time monitoring capability of IS captures dynamic changes in analyte interactions, which also helps in understanding the kinetics. The sensitivity of IS facilitates the detection of low analyte concentrations, while multiparmeter output provides multiple parameters for detailed analysis. IS is useful for studying the electrical response of the sensing plastforms under diverse conditions which is crucial for optimizing sensor performance. IS focuses on low-frequency behavior to understand long-term stability for the development of advanced gas sensors for applications ranging from environmental monitoring, industrial safety and healthcare. IS is divided into two categories based on the interface type: (a) Liquid Electrolyte-based and (b) Vapor Phase Electrolyte-based. The conventional Liquid Electrolyte-based IS, known as Electrochemical Impedance Spectroscopy (EIS), is widely used to analyze interfacial surface characteristics between the sample and electrolyte. In contrast, Vapor Phase Electrolyte-based IS is a measurement conducted in a vapor environment and called as Electrical Impedance Spectroscopy. Electrical impedance spectroscopy lays the groundwork for the characterization of gas sensing platforms. The gas sensing performance of the device is directly influenced by changes in its depletion area and variations in permittivity. In this thesis, we have employed Keysight, E4990A impedance analyzer for our measurements. It gives numerous parameters such as real and imaginary impedance, capacitance, resistance, quality factor, phase difference, current etc as function of frequency. The impedance measurement accuracy for the employed instrument is of $\pm 0.08\%$. We have employed the system for acetone vapors sensing measurements for a wide range of concentrations at room temperature. Multiparameter response for a frequency range of 10 kHz-10 MHz was observed for wide range of acetone concentration.

2.1.5.2 Electrochemical impedance spectroscopy

Electrochemical impedance spectroscopy (EIS) is another impedance based spectroscopic technique employed for sensing measurements. EIS is a powerful technique used for the analysis of interfacial properties related to interaction occurring at the electrode surface. Thus, EIS could be exploited in several important biomedical diagnosis and environment monitoring applications. During a standard EIS, the electrochemical system at equilibrium or in a steady state undergoes disturbance by applying a sinusoidal signal, either alternating voltage or current, across a wide range of frequencies. The subsequent step involves monitoring the system response to this perturbation. The typical electrochemical arrangement involves a 3-electrode system comprising the working electrode (WE), reference electrode (RE), and counter electrode (CE), all connected to a potentiostat. The working electrode serves as the electrocatalytic surface for a redox reaction occurring at a desired potential. If no current passes through the reference electrode, potential remains constant. The potentiostat gauges the potential difference between the working and reference electrodes, rectifying any deviation from the user-set value by directing a current between the working and counter electrodes. The interaction of the

WE with the electrolyte gives information about the concentration of electroactive species, charge-transfer phenomena, mass-transfer from the bulk solution to the electrode surface, and the resistance of the electrolyte. Each of these aspects is defined by an electrical circuit comprising resistances, capacitors, or constant phase elements in parallel or series arrangement. Consequently, EIS serves as a valuable tool for investigating mass-transfer, charge-transfer, and diffusion processes. In case of EIS based biosensors, the working electrode serves as a electroactive surface on which the reaction takes place. The development of functionalized electrode through the incorporation of nanomaterials to modify the transducer surface and the attachment of receptors or recognition elements represents a key approach in constructing electrochemical sensors. Depending on the specific material of interest, a broad range of nanostructured materials has been extensively utilized to enhance the surface area of the sensor. For electrochemical based impedance measurement, we employed Palm Sens 4 which operates in frequency range of 10 μHz-10 MHz, with an accuracy of 99% between the impedance measurement of 1 Ω-1 GigaΩ, with current and voltage accuracy below 1%. The sensing measurements were further analyzed via circuit fitting of the observed impedance response. In this thesis we have employed octadecylamine functionalized graphene to modify the gold working electrode for sensing pathogenic bacteria, commonly found in food and water sources.

2.1.5.3 Surface Plasmon Resonance

Surface plasmon polaritons (SPP) are generated due to the interaction of incident photons with the free electrons present at the metal-dielectric interface. SPP are the collective electron oscillations at the interface at the optical frequency. The SPP wave can be excited by a polarized light wave incident onto the metallic layer (e.g. gold film) via a coupling high refractive index medium (e.g. glass prism). At surface plasmon resonance (SPR), the component of wavevector of incident light planar to the interface matches to that of surface plasmon wave resulting in the absorption of energy of the reflected beam. SPR phenomenon is observed due to the wave matching condition between the wave vector of SP (K_{sp}) and the respective wave vector of incident light (K_i).

$$\vec{K_{sp}} = \vec{K_i} \tag{2.12}$$

The wave vector of the SPP wave is dependent on the dielectric constant of the metal and the medium over the metal. The wave matching condition is easily perturbed by the minute changes in dielectric environment surrounding the metal surface. This characteristic of SPR phenomenon enables it as a sensitive and label free sensing method. The amplitude of the wave-vector is inversely proportional to its wavelength and the direction is given in terms of cosine of angle of incidence (Eq:-2.13).

$$\frac{2\pi cos\theta_{SP}}{\lambda_{SP}} = \frac{2\pi cos\theta_i}{\lambda_i} \tag{2.13}$$

The wave vector matching condition given in Eq:-2.13; shows that the resonance condition can be achieved by varying the incident angle θ_i of the electromagnetic beam with the constant wavelength (λ_i) or vice-verse. Based on the parameter variation, the working principle behind SPR is divided in to two categories:

Angular interrogation: This is the most popular mode of SPR sensor as it provides high sensitivity towards analyte even for very low concentration. In angular interrogation method, the angle of incidence of a monochromatic light is varied and the reflected intensity is collected. The dip in intensity at a particular angle indicates the resonance. The angle of incidence at which SPR occurs is known as resonance angle (RA). Any adsorption on the sensing element causes a shift in the resonance angle. The angular interrogation can be achieved either by rotating prism-assembly or by rotating source and detector, simultaneously.

Wavelength interrogation: Wavelength interrogation based SPR instrument records the drop in intensity in the wavelength spectrum of the total internal reflected beam from the sensor assembly when it is illuminated by collimated polychromatic light. The incident optical wave and the surface plasmon wave in the metal couples at a particular wavelength with respect to the coupling condition as discussed earlier. At SPR, the reflected intensity

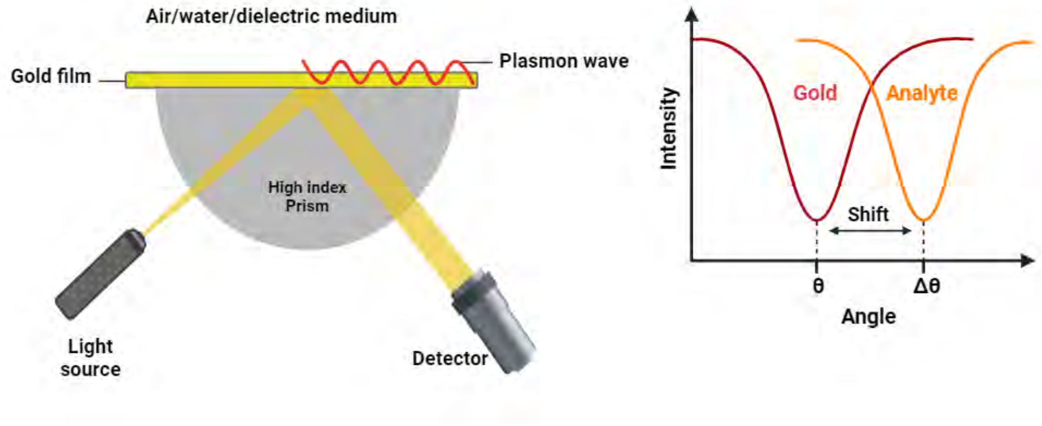

Figure 2.6: Schematic representation of Krestchmann configuration SPR.

at a particular wavelength extinguishes from the spectrum. The change in the dielectric medium over the metal surface causes change in the SPR condition and thereby a shift in the resonant wavelength is observed in the spectrum. Therefore, the variations in the refractive index of the sensing medium can be detected by measuring the change in resonant wavelength. The sensitivity of such a system is defined as the ratio of shift in resonance wavelength on analyte adsorption to RI variation of medium containing the analyte.

In this work, we have used home built SPR setup Optronix for the measurements. The Kretschmann configuration instrument [76] utilizes a 5 mW laser of wavelength 635 nm, coupling prism (RI=1.51) and a segmented photodiode as detector. The resolution and sensitivity of the equipment are 1.9μRIU and 53°/RIU respectively. The SPR chips were fabricated by depositing 50nm gold film on a 0.5 mm thick BK7 glass substrate through sputtering technique. The angle interrogation based measurements were carried for studying the optical properties of dielectric and metallic ultrathin films.

2.2 Data Analysis methods

2.2.1 Machine Learning

Machine learning (ML) is a subset of artificial intelligence (AI) specifically designed for the examination of data. This approach to data analysis involves the automatic construction of analytical models. The fundamental concept behind ML is that systems have the capability to learn from data, recognize patterns, and autonomously make decisions, reducing the need for extensive human intervention. In the context of sensing response studies, ML is a powerful tool set to determine complex patterns and relationships within experimental data. Traditional methods of data analysis often fall short when dealing with large and intricate data sets generated by modern scientific experiments. Unlike manual analysis, ML algorithms can automatically identify patterns, extract relevant features, and establish complex relationships within the data. This ability is particularly crucial when studying the sensing response, as it allows for a more subtle and comprehensive understanding of the underlying phenomena.

Types of Machine Learning Algorithms:

Machine learning can be broadly categorized into two main types: supervised learning and unsupervised learning.

Supervised Learning: In supervised learning, the algorithm is trained on labeled datasets, where the input data is paired with corresponding output labels. This type of learning is particularly useful when predicting or classifying specific outcomes. In the context of sensing response analysis, supervised learning can be employed to model and predict the behavior of sensors based on known input-output relationships.

Unsupervised Learning: Unsupervised learning involves working with unlabeled data, aiming to identify inherent patterns and structures within the dataset. Common techniques in this category include clustering and dimensionality reduction.

In the subsequent chapters of this thesis, the integration of ML techniques plays a pivotal role in the analysis of sensing responses. Chapter 3 utilizes PCA, an unsupervised learning technique, to extract essential features and reduce data dimensionality in the context of identifying best physical parameters from the multiparameter output response of impedance measurements employed for acetone sensing. In Chapter 4, various ML algorithms are explored for the observation of selective sensing of E. coli. The ability of ML to find subtle patterns and relationships within the experimental data enhances the analytical depth and contributes to a better understanding of the sensing mechanisms involved. The machine learning algorithms were written using the scikit-learn and keras package of Python.

2.3 Simulation methodology

2.3.1 Density Functional theory (DFT)

Density functional theory (DFT) renders the quantum-mechanical depiction of materials in their ground state accessible for simulations at a reasonably modest computational expense. DFT in principle, is an exact reformulation of the electronic structure problem in terms of the electronic density $n(r)$ rather than the many-body wave function $\psi(r_1\sigma_1, r_1\sigma_1...r_N\sigma_N)$. The approach of DFT requires a universal functional which is in general unknown and must be approximated. The basis of DFT is the work by Hohenberg and Kohn[77]. In their first theorem they proposed that all physical observables can be expressed as functional of the electronic charge-density. In their second theory they stated that the minimum value of the total-energy functional E[n(r)] is the ground state energy of the system, and the density which yields its minimum value is exactly the single particle ground-state density. Later, Kohn and Sham proposed a simpler method to approach and solve the many-body problem. They mentioned that for any interacting ground state density n_o(r), a corresponding non-interacting system in some effective potential V_s is constructed such that the non-interacting Hamiltonian H_s = T + V_s produce the same ground state density n_o(r).

$$E_s[n] = T_s[n] + \int v_s(\mathbf{r})n(\mathbf{r})d\mathbf{r}. \tag{2.14}$$

From HK theory we have

$$\begin{aligned} E[n] &= \int v_{ext}(\mathbf{r})n(\mathbf{r})d\mathbf{r} + \frac{1}{2}\iint \frac{n(\mathbf{r})n\left(\mathbf{r}'\right)}{\left|\mathbf{r}-\mathbf{r}'\right|}d\mathbf{r}d\mathbf{r}' + G[n] \\ &= \int v_{\text{ext}}\left(\mathbf{r}\right)n(\mathbf{r})d\mathbf{r} + U_H[n] + G[n] \end{aligned} \tag{2.15}$$

and we now write the universal functional as

$$G[n] = T_s[n] + E_{xc}[n].$$

where T$_s$[n] is the kinetic energy of a system of non-interacting electrons with density n(r) and E$_x c$[n] is the definition of the exchange and correlation energy of the corresponding interacting system. Over the years, various approximations for E$_x c$[n] have been formulated through different methodologies, each offering distinct levels of accuracy and/or computational efficiency. In this thesis, we have employed generalized gradient approximations (GGA) which adds the dependence on the local density gradient. In GGA the exchange correlation function is written as shown in Eq:-2.16;

$$\begin{aligned} E_{xc}^{GGA} &= \int d\mathbf{r}\varepsilon_{xc}^{GGA}(n(\mathbf{r}), |\nabla n(\mathbf{r})|) \\ &\equiv \int d\mathbf{r}\varepsilon_{xc}^{unif}(n(\mathbf{r}))F_{xc}(n(\mathbf{r}), |\nabla n(\mathbf{r})|) \end{aligned} \tag{2.16}$$

Different GGA exchange function F$_{xc}$, have been developed for different application. For this work we have employed Perdew, Burke and Enzerhof (PBE) functional as it provides a good balance between accuracy and computational efficiency. In this thesis we have employed GGA-PBE to calculate the optical properties of the monolayer, bilayer graphene (AA and AB stacking) and twisted bilayer graphene with AA and AB stacking for small and large twists for its potential application in biosensing via SPR. Fo the DFT calculations, we employed the CASTEP (Cambridge Sequential Total Energy Package), an ab initio quantum mechanical program to simulate the optical properties of monolayer and bilayer graphene structures. The optical properties, specifically the refractive index (RI), were calculated for a unit cell belonging to the P3/MMC/93 hexagonal crystal family. In monolayer calculations, a two-atom unit cell was used, while for bilayer systems, a four-atom unit cell was assumed with an interlayer distance of 0.342 nm. The study considered both AA stacking and AB stacking. For AA stacking, the second layer was positioned directly above the first layer, aligning the lateral coordinates of carbon atoms in each layer. In AB stacking, the second layer was shifted in the y-direction by one bond length of C atoms in graphene (0.142 nm).

A relative in-plane twist was applied to the bilayer system, and the RI was calculated for both small and large angular twists. The RI calculations employed ultrasoft pseudopotentials which represents the ionic cores. Total energy minimization was conducted through convergence tests, including lattice relaxation, energy change, maximum force, and stress in the unit cell, to achieve the ground state energy. The optimization comprised 101 iterations, with the total energy per atom converging up to 10^{-4} nm and 0.05 GPa, respectively. The calculations utilized a Brillouin zone with a $4 \times 4 \times 1$ k-point mesh of the Monkhorst–Pack (MK) scheme. The kinetic energy plane wave cutoff was set at 700 eV for single-layer systems and 1000 eV for bilayer systems. RI calculations were performed within the energy range of 0.03–15 eV.

2.3.2 Finite difference time domain (FDTD) method

Finite difference time domain method (FDTD) is a 3D electromagnetic simulation technique extensively employed in nanoplasmonic simulations. It is a state of the art method for solving Maxwell's equations in complex geometries. It can provide a direct solution performing Fourier transformations in time and space offering a unique insight into electromagnetic and plasmonic nanostructures. Therefore, it can serve as a robust numerical technique for theoretical investigations into the SPR mechanism, offering high sensitivity and resolution. In FDTD approach, space and time are discretized, with space divided into box-shaped "cells". The electric fields are situated on the edges of the boxes, while the magnetic fields are positioned on the faces, allowing for detailed and accurate modeling of electromagnetic phenomena. The arrangement of fields as described is commonly referred to as the "Yee cell" or "Yee grid" in the context of the FDTD method. Within this method, time is discretized into small steps, with each step representing the time it takes for the electromagnetic field to traverse from one cell to the adjacent one. This temporal discretization allows for an efficient and accurate simulation of the dynamic behavior of electromagnetic fields in the computational domain. The basic principle of FDTD is to solve the Maxwell's differential equation;

$$\Delta \times E = -\frac{\partial B}{\partial t} \tag{2.17}$$

$$\Delta \times H = J + \frac{\partial D}{\partial t} \tag{2.18}$$

where E, D, H, B, J represent the electric field, electric displacement, magnetic field, magnetic induction intensity and current density, respectively. Taking the function $f(x, y, z, t)$ to denote the electric or magnetic field in the coordinate system, we have the form $f(x, y, z, t) = f(i\Delta x, j\Delta y, k\Delta z, n\Delta t) = f^n(i, j, k)$. Then $f(x, y, z, t)$ can be discretized via the central difference approximation in both space and time:

$$\begin{aligned}
\left.\frac{\partial f(x,y,z,t)}{\partial x}\right|_{x=i\Delta x} &\approx \frac{f^n\left(i+\frac{1}{2},j,k\right)-f^n\left(i-\frac{1}{2},j,k\right)}{\Delta x}\\
\left.\frac{\partial f(x,y,z,t)}{\partial y}\right|_{y=j\Delta y} &\approx \frac{f^n\left(i,j+\frac{1}{2},k\right)-f^n\left(i,j-\frac{1}{2},k\right)}{\Delta y}\\
\left.\frac{\partial f(x,y,z,t)}{\partial z}\right|_{z=k\Delta z} &\approx \frac{f^n\left(i,j,k+\frac{1}{2}\right)-f^n\left(i,j,k-\frac{1}{2}\right)}{\Delta z}\\
\left.\frac{\partial f(x,y,z,t)}{\partial t}\right|_{t=n\Delta t} &\approx \frac{f^{n+\frac{1}{2}}(i,j,k)-f^{n-\frac{1}{2}}(i,j,k)}{\Delta t}
\end{aligned} \tag{2.19}$$

Solving the above equations using numerical methods, electric and magnetic fields associated with each Yee cell can be obtained. In this thesis, we have used Ansys Lumerical FDTD software to solve the equations. Ansys Lumerical is graphical user interface based commercially available software package with well matched progressive conformal mesh with dispersive and high RI difference materials with extreme accuracy. The detailed setup and arrangement is mentioned in the subsequent chapters.

CHAPTER 3

Ultrathin film of carbon nanotubes for acetone sensing

In this chapter, we discussed the formation of stable Langmuir film of functionalized CNT at the air-water interface. The Langmuir monolayer of pristine and octadecyl amine functionlaized CNT (ODA-CNT) at the A/W interface was studied. Although the monolayer of pristine-CNT displays highly elastic liquid phase compared to that of ODA-CNT, the degree of aggregation of the pristine-CNT is much higher as compared to ODA-CNT. The Langmuir monolayer of ODA-CNT shows uniform liquid like phase with less aggregation as observed through BAM and FESEM images. Further, we discussed the application of ultrathin films of CNT at the A/S interface for acetone sensing. The sensing response of LB film of pristine and ODA-CNT were compared with bulk CNT. Here, thin films of CNT was formed on interdigitated gold electrodes and was employed for the acetone vapor sensing using the impedance spectroscopy (IS) at room temperature. The LB film deposited in liquid-like phase of the Langmuir monolayer of ODA-CNT revealed aligned nanotubes whereas pristine-CNT showed random alignment. Being a reducing agent, acetone interacts readily with the CNT through the transfer of electrons. Using IS, multiparameters were measured with respect to both frequency and acetone vapor concentration. Principal component analysis (PCA) of the IS data revealed capacitance as the most suitable parameter for acetone vapor sensing. In the ODA-CNT film, we were able to observe a very low limit of detection (0.5 ppm) and a wide detectable concentration range (1-300 ppm) for acetone sensing at room temperature. The 2D calibration map revealed that the sensing performance of acetone using LB film was much better as compared to that of drop-cast film of ODA-CNT and LB film of pristine-CNT. The superior sensing performance of the LB film of ODA-CNT is attributed to the uniform and aligned nature of the nanotubes, leading to a coherent behavior due to interaction with the acetone molecules. This study shows the potential of LB films of ODA-CNT for sensitive and low level detection of acetone vapor at room temperature.

3.1 Introduction

CNT have been considered as one of the interesting and widely investigated material for numerous industrial [78, 79] and sensing applications [80, 81]. CNT exhibit extraordinary electrical, mechanical, and chemical properties, making them ideal for sensing applications. Their high surface area, sensitivity to environmental changes, and exceptional electrical and optical attributes enable precise detection of various substances ranging from gases to biomolecules. CNT-based sensors offer enhanced sensitivity, rapid response times, and low detection limits, holding great promise for advancements in environmental monitoring, medical diagnostics, and industrial safety. For the development of a sensor, it is essential to address the fundamental issues such as efficient binding and perceptible change in the physicochemical properties which can be measured at a high resolution using a physical transducer. CNT offers excessive surface π-electrons which assist the adsorption of organic molecules through π-π stacking interaction. The perturbation of the π-electrons of CNT due to adsorption of foreign analytes can change the physical properties remarkably. Thus, it is considered as one of the efficient material for sensing application [80–82]. The enormous S/V ratio of the CNT ensures a high density of adsorption sites for gas molecules which in-turn enhance the signal-to-noise ratio when measured through the transducer.

In general practice, CNT are employed as a functional layer in sensing devices. It offers several advantages over conventional metal-oxide based sensing platforms. The sensing capability of metal-oxide layers require high temperature operation and high power consumption. Additionally, the required low concentration sensitivity for medical diagnosis using metal oxide sensors is not appreciable. However, several reports [83, 84] have found CNT to have high sensitivity, low power consumption, low response time and improved charge transport even at room temperature.

Further, the coherent behavior of the aligned CNT has been proved to enhance the device performance. The aligned CNT have several applications; it can act as source of field emission electrons [85, 86], gas sensors [87–89], energy conversion and storage devices [90, 91]. CNT can be aligned on the surface of a device using chemical vapor deposition (CVD), field assisted alignment, and liquid phase induced assembly techniques. Liquid phase assembly such as LB technique is not only low cost solution but also offers several advantages such as control over the surface density, surface phases and number of layers. If CNT are deposited as a functional layer in the ultrathin regime using the LB technique, it can offer a highly efficient active surface by providing a enormous gain in S/V ratio, and aligned nanotubes for coherent activities [92, 93]. There are numerous reports on the LB film of CNT in the ultrathin regime and its enhanced sensing application. LB film of CNT has found its applications in various chemical sensors[94], biosensors[95], heavy metal sensing[96], sensors for health monitoring[97] and gas sensing[47, 98]. It has been observed that LB film employed for gas sensing applications has enhanced sensing performance compared to the bulk films of CNT. Abdulla et al. [99] have presented the fabrication of highly ordered ultrathin films of polyaniline-functionalized CNT using the LB technique, resulting in improved ammonia gas sensing capabilities. The interfacial assembly process can align the CNT composite into organized blocks and subsequently forms a well-defined and oriented monolayer. These tailored LB films exhibited exceptional room temperature sensitivity for NH_3 due to directed electron transport and rapid analyte diffusion within the aligned structure, holding promise for high-performance gas sensors. Several other reports based on gas sensing applications for ultrathin films of CNT fabricated using LB technique are highlighted in a review article by Cao et al. [1, 100].

Recently, the focus of gas sensing has been shifted towards sensing volatile organic gases such as acetone, to improve their sensitivity, portability, power consumption and limit of detection [101]. Many of these studies have been directed towards detecting acetone in the breath of diabetic patients. Studies have shown that the normal acetone concentration ranged from 0.2 to 0.8 ppm in healthy adults and diabetes patients exhibited levels above 1.8ppm [101, 102]. Additionally, research has extended to other health conditions, such as

Sensing platform	Sensing mechanism	Operating Temp (°C)	Concentration range	Reference
Co3O4	Resistive	200	0.1-50 ppm	Fan et al.[48]
Bi0.4Sr0.6FeO3	Mixed Potential	600	2-50 ppm	Liu et al.[104]
Au/SnO_2	Resistive	220	5-50 ppm	Li et al[105].
PdAu/SnO2	Resistive	250	0-2 ppm	Li at al[106].
$NiFe_2O_4$	Chemiresistive	200	1-100 ppm	Zhang et al.[107]
WO_3 nanofibers	Resistive	350	0.4-5 ppm	Kim et al.[108]
ZnO QDs	Gas chromotography	430	0-5 ppm	Jung et al.[109]
Graphene QD/ZnO	Resistive	320	0.5-2 ppm	Liu et al.[110]
C-doped WO_3	Voltage-based	300	0-5 ppm	Xiao et al.[111]
MWCNT/SnO2	Resistive	200	0.5-5 ppm	Salehi et al.[49]

Table 3.1: Recent studies on acetone sensing as a biomarker for diabetes detection.

lung cancer, where breath acetone concentrations varied between healthy subjects and patients. Considering the global prevalence of diabetes, which is expected to rise significantly, effective monitoring and diagnosis are crucial. Acetone gas, being a promising breath biomarker for diabetes, is to be established for its potential invasive, real time and continuous monitoring[103]. Acetone gas is also considered as a harmful substance, with specified exposure limits in industrial settings. Prolonged exposure to such high concentration of industrial acetone (100-400 ppm) can lead to several ailments such as drowsiness, respiratory depression, gastrointestinal problems, hyperglycaemia, ketoacidosis, acidosis, hepatic and renal damage. Monitoring acetone concentrations in such environments is essential for ensuring environmental safety and health compliance. Therefore, the research on acetone gas sensors spans various aspects, from medical applications in diabetes diagnosis to environmental safety in industrial settings. In the available literature, the proposed acetone sensing have higher limit of detection and are functional at high temperature. Few of the reports are mentioned in the Table-3.1

From the Table-3.1, it is evident that although few of the sensing platforms have been proposed for low level detection of acetone and can potentially employed as a diabetes bio marker via breath analysis, but their operating temperature is too high to be fabricated as point of care device. Other sensing platforms, that are available and shows decent response for acetone at room temperature fails at low level detection. Further, most of the sensors available in literature are resistance based measurements, which are highly sensitive to temperature and humidity. Thus, there is a need to have a acetone sensing platform for wide range of concentration at room temperature and to identify the parameter that is less prone to physical constants such as temperature and humidity. The development of reliable, non-invasive approaches for detecting acetone for a wider concentration range such as few ppm to hundreds of ppm is required to address a wider application from medical diagnosis to industrial pollution[112, 113] is required.

The state-of-art sensing technology may require multiparameters for efficient performance and reliable decision making [114, 115]. In general, the multiparameters measuring device essentially measures several physical parameters using a set of integrated transducers. Single transducer with multiple channels can be utilized for measuring a single parameter viz electrical or optical but with different functional layers. Such systems are electronic nose [116, 117] and surface plasmon resonance imaging devices [118, 119]. Impedance Spectroscopy (IS) is an emerging sensing platform for measuring several parameters viz real and imaginary part of impedance, capacitance, output current, phase difference and quality factor from a single channel consisting of a common functional layer. The sensing using IS simplifies the analysis as the sensing environment and the functional layer does exhibit a common nature of interaction for all the measured IS parameters.

In this chapter, we demonstrate that the organic functionalization of CNT through ODA can yield a stable Langmuir film at the A/W interface which can be transferred to solid substrate using LB technique for sensing application. For LB film fabrication, the CNT are to be dispersed in organic solvent and then spread at the A/W interface. However, the dispersion and spreadability of pristine-CNT at the A/W interface is difficult. Therefore, it is often essential to functionalize the CNT with organic ligands so that it can be easily dispersed and spread at the A/W interface for LB film processing. Additionally, the functionalization with organic ligands can enhance the adsorption capability of the CNT due to specific interaction. Here, we have utilized ODA-CNT for the fabrication of ultrathin LB films and used it for sensing acetone vapors at the room temperature. The sensing performance of LB film of ODA-CNT was compared with the LB film of pristine-CNT as well as randomly aligned ODA-CNT for better understanding. IS was used for sensing acetone vapor at room temperature. The multiparameters from IS were recorded as a function of frequency and the concentration of acetone vapor. Our observations using principal component analysis (PCA) showed that capacitance is the most reliable parameter for sensing acetone. The LB film of ODA-CNT exhibited efficient sensing as compared to LB film of pristine-CNT and drop casted film of ODA-CNT. In case of LB film of ODA-CNT, the limit of detection (LOD) and the range of concentration of acetone was found to be 0.5 ppm and 1-300 ppm, respectively.

3.2 Experimental section

Pristine single-walled carbon nanotubes (pristine-CNT, cat.# P2-SWCNT) and octadecylamine single-walled carbon nanotubes (ODA-CNT, cat.# P5-SWCNT) were purchased from Carbon Solutions Inc. The organic solvents, chloroform, and acetone were purchased from Sigma Aldrich. Chemicals were used without any further purification. Gold interdigitated electrodes (IDE) were purchased from NanoSPR, USA. The Langmuir monolayer and LB films were prepared using an LB trough (KSV-NIMA). The IS measurements were performed using an impedance analyzer (Keysight, E4990A). The IDE were cleaned by treating them with cold piranha solution (conc $H_2SO_4 : H_20_2$ as 3:1 by volume) followed by successive rinsing with ion-free water and ethanol several times. A stock solution of pristine-CNT and ODA-CNT with a concentration of 0.03 mg/mL was prepared in high performance liquid chromatography (HPLC) grade dimethyl formamide (DMF) and chloroform solvent, respectively. The Langmuir films at the A/W interface were formed by spreading the CNT solution (150 μL for ODA-CNT and 1250 μL for pristine) on the water surface between the two barriers of Langmuir trough (KSV NIMA). The trough was then left undisturbed for 90 minutes to allow the solvent to evaporate. The amount of CNT dispersion were found after multiple trials. The sample for which homogeneous dispersion and phase transitions of Langmuir monolayer are observed, the sample volume is finalized. After the volume spread was finalized, fresh samples were again dispersed after cleaning and the Langmuir film was compressed by symmetric lateral movement of the barriers, and corresponding surface pressure (π) as a function of area was recorded. The surface pressure was recorded using a pressure sensor which is connected with a Wilhelmy paper with an accuracy of 0.01 mN/m. The surface phases of the Langmuir film were observed using a Brewster angle Microscope (BAM, KSV NIMA Micro-BAM). The microscope was equipped with a 30 mW, 659 nm laser yielding 12 μm spatial resolution in images. The Langmuir film at the a/w interface was transferred onto the IDE via the LB technique at a target surface pressure (π_t) of 10 mN/m. The substrates with gold deposited IDE were cleaned using cold piranha solution for about 1 minute. The substrates were rinsed successively with ultrapure water and ethanol. The substrates were dried using a jet of nitrogen gas. The substrates were immersed initially before the spread of monolayer and a single layer of LB film was deposited by the upstroke of the dipper. The dipper speed was maintained at 1 mm/min. The deposition was performed under the feedback mechanism where the barrier position was adjusted automatically to maintain π_t. This ensures a high quality LB film. The physical adsorption between the ODA-CNT and the substrates was weak to support multilayer formation by the LB deposition mechanism. Drop cast films of the CNT over the IDE were formed by spreading 50μL of ODA-CNT stock solution using a micro pipette and were allowed to dry in ambient for ≈1 hour. The film deposited electrodes were stored in a vacuum desiccator which were later used in sensing measurements. The acetone sensing measurement were performed using the impedance analyzer setup (Fig:-3.4) in the frequency range of 10 kHz - 10 MHz. The concentration of acetone was varied by spreading a given volume of liquid acetone in the sensing chamber. To obtain a homogeneous dispersion of acetone vapor, around 30 mins time was allowed before performing the measurements. After the sensing measurements were performed, the sensing chamber was flushed with nitrogen gas for about 30 minutes. The impedance measurements were performed again after flushing. For the drop cast film, the capacitance curve showed some hysteresis $\approx 25\%$ whereas in case of LB film, there was a minimal hysteresis less than 1%. All the experiments were performed at room temperature ($\sim 25 \pm 2°C$).

3.3 Results and discussion

The Langmuir films of the pristine-CNT and ODA-CNT were formed separately at the A/W interface in the Langmuir trough and the corresponding surface pressure (π) vs area per μg of the CNT (A_w) isotherms were recorded (Fig:-3.1(a)). The area available for the CNT in the Langmuir trough was normalized by the mass of the CNT spread on the water surface. The isotherm of pristine-CNT has lower startup area per unit μg as compared to ODA-CNT which states higher aggregation in pristine-CNT at the a/w interface. The surface pressure remains negligible upto $30\ cm^2/\mu g$ for ODA-CNT and $4\ cm^2/\mu g$ for pristine-CNT. The region for negligible surface pressure in both isotherms may indicate the gas like phase. The gas like phase is observed where there is minimal interaction in the molecules spread at the A/W interface. On further compression of the film, the surface pressure starts to rise sharply and monotonically till the film is completely compressed in the trough. The rise in the surface pressure showed liquid-like phase of the Langmuir monolayer. There are minor changes in the slope of both the isotherms at 24 $cm^2/\mu g$ for ODA-CNT and 4 $cm^2/\mu g$ for pristine-CNT which might indicate the initiation of the collapse of the film. In case of Langmuir films of nanomaterials, it is difficult to observe a clear collapse in the isotherm. This might be due to poor amphiphilicity of the nanomaterials as compared to the classical monolayer forming organic molecules such as stearic acid, DPPC etc. The slow collapse in the Langmuir monolayer of nanomaterials can be due to folding, wrinkling or 3D stacking on the water surface. The minor change in the slope can be conveniently detected by calculating the in-plane isothermal elastic modulus (E) using the relation: $|E| = \left|-\frac{1}{A}\frac{d\pi}{dA}\right|$ The E is a convenient parameter to assess the elastic nature of the monolayer in a given surface phase and to detect the discontinuity in the isotherm due to weak phase transition [89]. The variation of E as a function of A_w is shown in Fig:-3.1(b). On compression, liquid like phase appears in both the cases as indicated by the steep rise in the E. The maximum value of E in the liquid like phases of pristine-CNT and ODA-CNT was found to be around 50 and 25 mN/m, respectively. The decrease in the value of E on further compression may indicate the initiation of the collapse of the monolayer. Due to the absence of hydrogen bonding between the pristine-CNT and

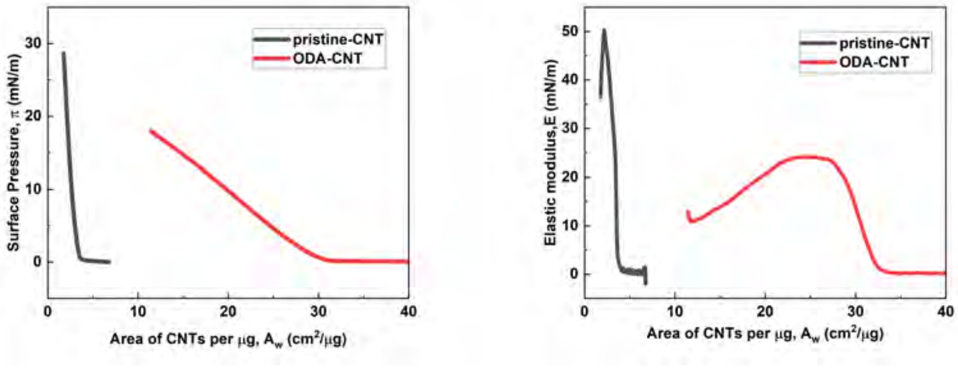

(a) (b)

Figure 3.1: (a) Surface pressure (π)-area per μg of the CNT (A_w) isotherm of the Langmuir film of pristine-CNT and ODA-CNT at the air-water interface. (b) The isothermal in plane elastic modulus of pristine-CNT and ODA-CNT.

water, the homogeneous spreading of pristine-CNT is compromised which results in higher degree of aggregation on the water surface. On the other hand, ODA-CNT behave amphiphilically and thus spreads uniformly over the water surface. It is therefore expected to obtain a uniform film with aligned ODA-CNTs when deposited on substrates using the LB technique.

The Langmuir film of the pristine-CNT and ODA-CNT at the a/w interface were observed using BAM (Fig:-3.2). In the BAM images, the dark region represents the gas like phase whereas the bright region represents the liquid like phase. It is clear from the images captured at different surface pressure during compression of the film that the liquid like phase exhibited by the ODA-CNT is more uniform (Fig:-3.2(c)) as compared to that of pristine-CNT (Fig:-3.2(f)). The Langmuir film of pristine-CNT shows aggregates (very bright domains) at surface pressures of 3 and 9 mN/m (Fig:-3.2(e)-(f)).

The domains observed in the BAM image of the Langmuir monolayer of ODA-CNT in the liquid like phase appears fluidic and mobile. Additionally, the maximum magnitude of elastic modulus in this phase is $\sim$ 25 mN/m which also suggest the phase to be liquid like. The classification of surface phases of Langmuir monolayer based on elastic modulus suggests the E value in the range 12-50 mn/m to be liquid like phase and 100-250 mN/m to be liquid condensed phase [120, 121].

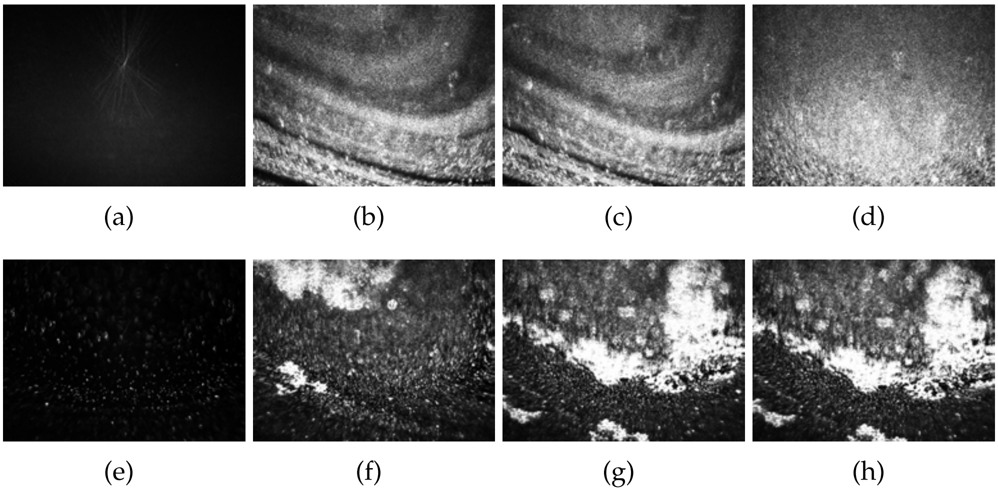

Figure 3.2: BAM images of Langmuir film of ODA-CNT (a-d) and pristine-CNT (e-h) at different surface pressures (a,e) 0mN/m, (b,f) 3mN/m, (c,g) 6mN/m and (d,h) 10mN/m. The size of the images are $3.5{\times}4\ mm^2$.

The Langmuir film of ODA-CNT and pristine-CNT was transferred onto silicon substrates at a target surface pressure of $10\ mN/m$ using LB technique. The transfer ratio for both the films were $\approx\ 0.85$. Field emission scanning electron microscope (FESEM) was employed to study the morphology of the transferred film. In the ODA-CNT film transferred via LB technique (Fig:-3.3(a)), the nanotubes appear to align on an average direction as indicated by the arrow. This alignment of the CNT on the substrate surface depends on the relative orientation of the substrate with respect to the barrier motion. As, the ODA-functionalization helps in homogeneous dsipersion of the CNT on the water surface, the amount of aggregation on the transferred film is very low. However, in case of pristine-CNT, the nanotubes appear to aggregate and randomly distributed even in the LB film due to its non-homogeneous dispersion at the interface (Fig:-3.3(b)). The FESEM study indicated that the uniformity and ordering in LB film of ODA-CNT is much better as compared to that of LB film of pristine-CNT and drop cast film of ODA-CNT. Fig:-3.3(c) shows the FESEM image of drop cast film of ODA-CNT. The drop cast film showed random arrangement of the nanotubes.

The effective surface area of CNT enables a substantial number of adsorption sites for the gas molecules to get adsorbed. When a reducing gas such as acetone comes into contact of the CNT surface, it results in an increase in elec-

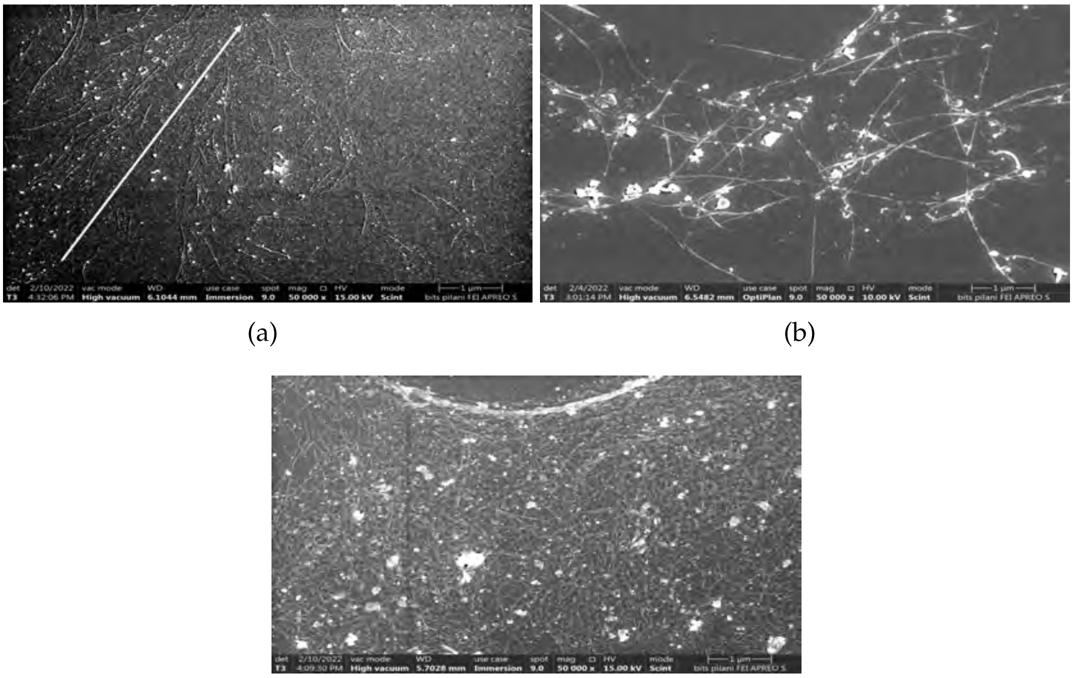

(a)

(b)

(c)

Figure 3.3: Field emission scanning electron microscope images for (a) LB films of ODA-CNT (b) LB film of pristine-CNT and (c) drop cast film of ODA-CNT. The scale bar of each image is 1 μm. The bright domains in the image represent the gold-cluster. The sample was deposited with gold (2-3 nm) prior to FESEM imaging to enhance the contrast and reduce surface charging.

tron concentration. Due to p-type semi-conducting behavior of CNT [122], it has been reported by Young et al. [123] that as the gases with electron-donating nature are adsorbed on its surface, there is reduction in the number of holes which results in a subsequent increase in the impedance of CNT. Thus, the impedance spectroscopy with multiple parameters directly or indirectly related to the adsorption of analytes. Therefore, impedance spectroscopy can be a relevant technique for sensing such gasses using CNT.

Further, we have discussed the sensing of volatile organic solvent viz. acetone using functional layer of LB film and drop cast film of ODA-CNT through the impedance spectroscopy technique. The home built setup used for the sensing is shown in Fig:-3.4.

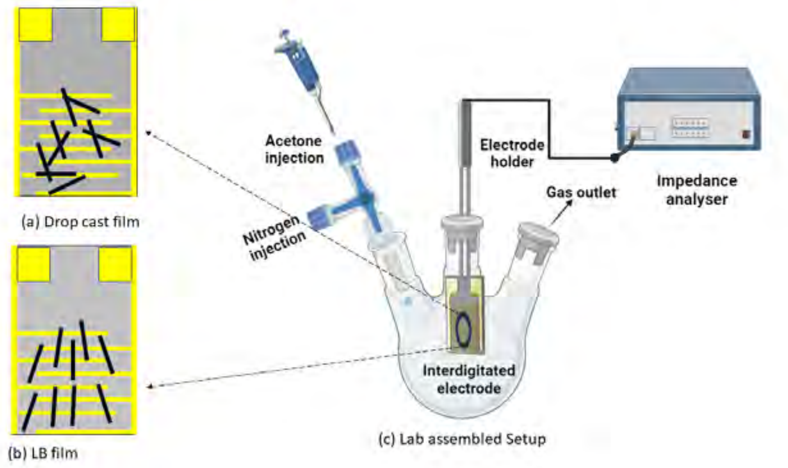

Figure 3.4: A schematic of lab assembled setup for acetone sensing at room temperature.(a) shows the randomly aligned CNT for the drop cast film, (b) vertically aligned CNT for LB film and (c) Lab assembled setup for measurement.

A set of parameters viz. real and imaginary part of the impedance, capacitance, conductance, phase difference etc were collected during sensing of the acetone using the film of CNTs. It is noteworthy that some of the parameters are redundant which do not add any value in decision making during sensing. It is therefore, essential to analyze the parameters obtained from a given sensor and select the most relevant for reliable sensing. The principal component analysis (PCA) is an unsupervised learning technique in machine learning algorithm which can be used to reduce the dimension of the parameter space

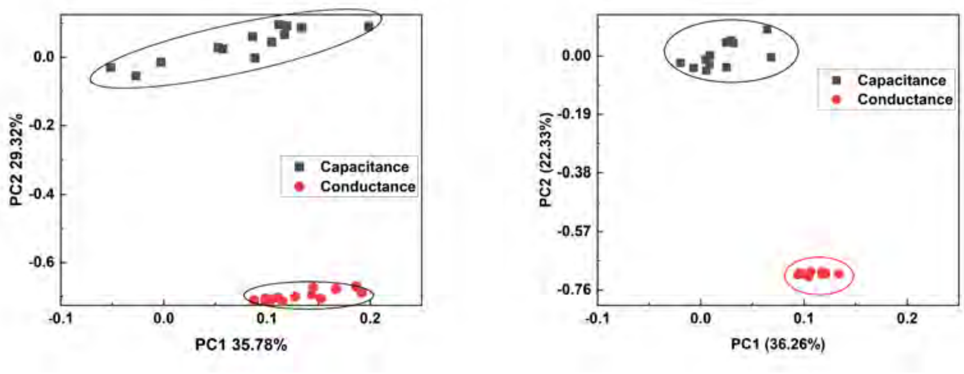

(a) (b)

Figure 3.5: Principle components (PC1 and PC2) plot for capacitance and conductance with respect to different concentrations of acetone for (a) LB film of ODA-CNT (b) drop cast film of ODA-CNT.

and identify the high variance parameters for making reliable decision during sensing.

In PCA, firstly a covariance matrix is computed, revealing relationships between input variables. Eigenvalues and eigenvectors are then derived, representing variance and component directions. Eigenvalues are sorted, and components capturing most variance are selected, and the original data is projected onto these components. Here, the output parameters as the function of frequency for each concentration of the acetone vapor was analyzed using the PCA. The higher variance parameters were found to be capacitance and conductance. Large variance parameter during sensing is preferred as it can cause significant change in the values due to minor change in the concentration. It was observed that approximately 65 percent of data was explained by two parameters capacitance ($\approx 35\%$) and conductance ($\approx 30\%$) for each concentration of the acetone vapor. The principle components PC1 and PC2 for capacitance and conductance for different concentration of acetone sensed using LB film of pristine and ODA-CNT and drop cast film of ODA-CNT are shown in Fig:-3.5.

Fig:-3.5 shows comparison between the principle components of capacitance and conductance of LB film and drop cast films of ODA-CNT with respect to acetone concentration. It was observed that PCA response for LB film of ODA-CNT had higher variance in for both capacitance and conductance as compared to that of drop cast ODA-CNT film. Therefore, for sensing applications PCA shows that LB films of ODA-CNT are more suitable choice. Further for LB ODA-CNT film, the capacitance and conductance values were also compared and it was observed that capacitance shows higher variance due to change in concentration of acetone as the spread in data points is larger. (Fig:-3.5(a). Such spread indicates large variance due to small change in the concentration of the acetone. This is preferable for high performing sensor. Therefore, it is evident that capacitance is the more suitable parameter to observe for sensing acetone.

Henceforth, a two dimensional calibration map (surface contour plot) of capacitance as a function of frequency and acetone concentration was plotted Fig:-3.6. For comparison, the calibration maps of the LB film of ODA-CNT, the LB film of pristine-CNT, and the drop-cast film of ODA-CNT are shown in Fig:-3.6 (a), (b), and (c), respectively.. It can be observed that in both drop cast and LB films, the capacitance decreases with frequency at a given acetone concentration. However, in LB ODA-CNT film the decrease in capacitance at the given acetone concentration is comparatively more prominent. The contour plot (Fig:-3.6(b)) clearly indicates that in case of LB film of pristine and drop cast film of ODA-CNT, the variation in capacitance value as a function of concentration at a given frequency does not show any trend and the magnitude of the capacitance shows minute change. Interestingly, in case of LB film of ODA-CNT (Fig:-3.6(a)) a clear trend in variation in the capacitance value with the concentration of acetone at a given frequency is seen. The limit of detection(LOD) and the range of concentration of acetone sensing using LB film of ODA-CNT were found to be 0.5 ppm and 1-300 ppm respectively.

In low frequency range 10 kHz -2 MHz, the capacitance of LB film with respect to acetone concentration is more prominent and the decrease is monotonic. The monotonic decrease was found to be linear for the entire frequency range $10kHz - 10MHz$. The slope of such linear trend can be related to the sensitivity of the sensor[89]. The range of sensing concentration and sensitivity appears decreasing with increasing frequency. Therefore it is suggested that in order to have efficient acetone sensing based on LB film of ODA-CNT, ca-

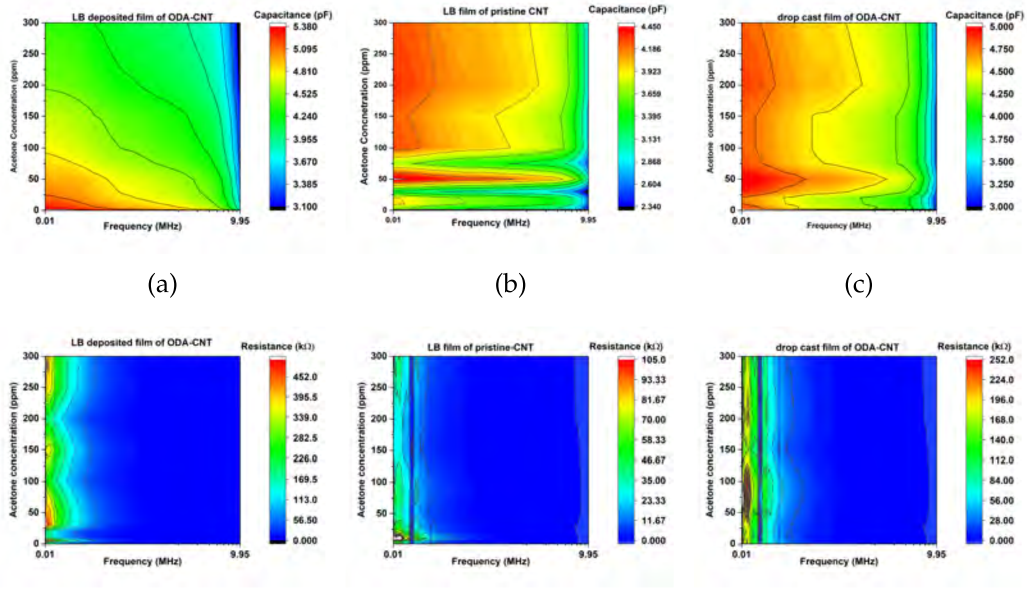

(a) (b) (c)

(d) (e) (f)

Figure 3.6: 2D calibration maps (surface contour plot) of capacitance as a function of frequency and the concentration of acetone vapor obtained from the (a) LB film of ODA-CNT, (b) LB film of pristine-CNT and (c) dropcast film of ODA-CNT. 2D representation of resistance as function of frequency and the concentration of acetone vapor obtained from the (d) LB film of ODA-CNT, (e) LB film of pristine-CNT and (f) dropcast film of ODA-CNT

.

pacitance can be used as the optimal sensing parameter in the frequency range of $10-500\ kHz$. Such studies are useful in determining the required concentration range of the analyte and the optimal sensitivity. The parameter resistance is found to be random for varying concentration and frequency (Fig:-3.6 (d) (e) and (f)).

IS is an useful technique which provide insights into the detection mechanism of acetone sensing. The capacitance from the impedance response can also be accounted for fitting the data through an equivalent circuits (Fig:-3.7 (c)). Using the circuit, Nyquist plot was simulated for $100\ Hz - 10\ MHz$ for both drop cast and LB deposited films of ODA-CNT as shown in inset of Fig:-3.7 (a) and (b).

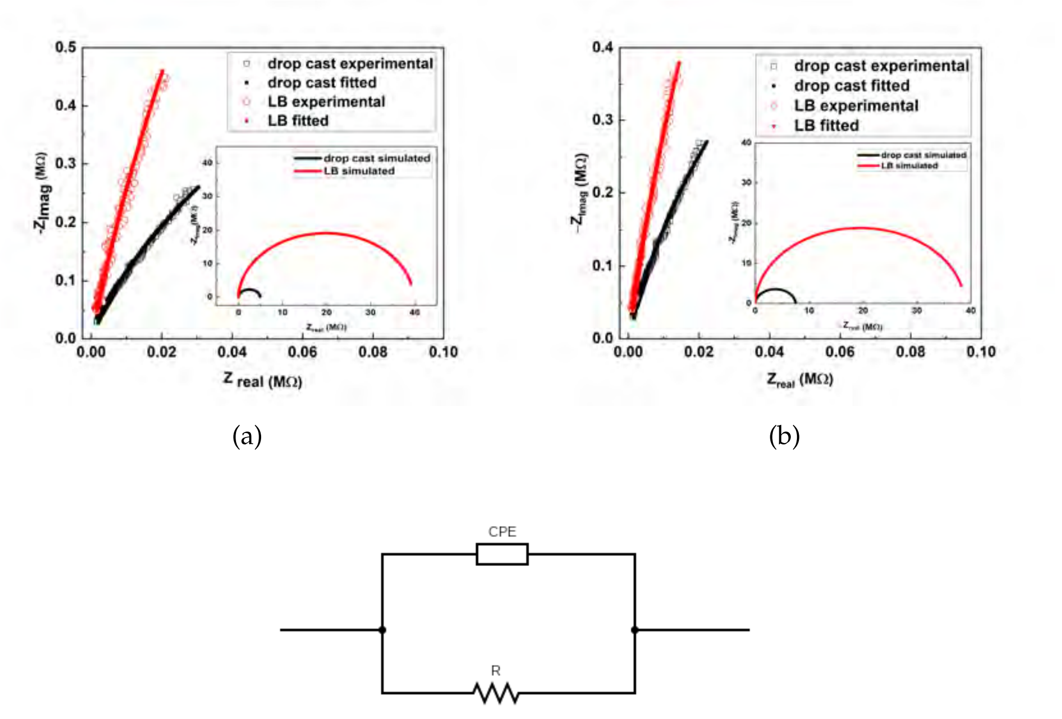

(a)

(b)

(c)

Figure 3.7: Nyquist plots for drop cast and LB films of ODA-CNT (a) in absence of acetone (b) in presence of acetone (25 ppm) (c) Circuit used in the IS software for Nyquist plot data fitting.

Fig:-3.7 (a) and (b) shows the Nyquist plot comparison of drop cast and LB film of ODA-CNT at 0 and $25\ ppm$ acetone concentration, respectively. The imaginary component of impedance in the LB deposited film is relatively

Concentration (ppm)	**drop cast ODA-CNT film**				**LB ODA-CNT film**			
	C (pF)	C_m $(pF/\mu g)$	**R (MΩ)**	R_m $(M\Omega/\mu g)$	**C (pF)**	C_m $(pF/\mu g)$	**R (MΩ)**	R_m $(M\Omega/\mu\ g)$
0	4.089	0	23.06	0	5.358	0	48.175	0
1	4.371	0.00918	22.16	0.03613	5.297	0.94384	48.175	1.55749
2	4.325	0.02572	23.25	0.03959	5.262	1.16082	48.075	2.10608
5	4.355	0.02859	24.06	0.04082	5.235	1.68427	48.125	2.05921
10	4.394	0.03345	22.06	0.04141	5.183	1.88245	48.185	2.13889
25	4.364	0.03691	22.86	0.04298	5.145	1.94619	48.225	2.09848
30	4.384	0.03691	22.16	0.04406	5.097	2.09886	48.455	2.11024
50	4.371	0.03691	23.45	0.04374	5.053	2.22021	48.465	2.02731
75	4.398	0.0346	23.34	0.04307	4.985	2.51946	48.485	2.33232
100	4.387	0.0346	23.90	0.04507	4.944	2.61716	48.456	2.08197
150	4.327	0.0346	23.46	0.04406	4.865	2.8106	48.459	2.11641
200	4.390	0.0323	24.06	0.04406	4.854	3.15409	48.464	2.03585
300	4.406	0.03322	24.26	0.04406	4.852	3.85107	48.555	2.38045

Table 3.2: Comparison of capacitance and resistance values obtained after fitting the Nyquist plots for each acetone concentration for drop cast film of ODA-CNT and LB film of ODA-CNT film.

larger compared to drop cast film. The larger diameter of semicircle observed in simulated Nyquist plot for LB film is attributed to high impedance value. This is because of the ultrathin film nature and low aggregation as compared to the randomly oriented drop cast film. The impedance value depends on charge carrying ability of deposited CNT due to its interaction with analytes.

However, further analysis of the Nyquist plot was performed for different acetone concentration. It was observed that the overall response has capacitive nature as the constant phase (n) was observed to be $\approx\ 0.96$ for drop cast film of ODA-CNT and $\approx\ 0.987$ for LB film of ODA-CNT. The normalized response for capacitance (C_m) and resistance R_m were calculated (Eq. 3.1) and a comparison as shown in Table 3.2.

$$C_m = |\frac{C - C_o}{m}|, \quad R_m = |\frac{R - R_o}{m}| \tag{3.1}$$

Here, C_o and R_o are the initial capacitance and resistance, respectively in the absence of analyte, C is capacitance, R be resistance for a given acetone concentration and m is the mass of ODA-CNT deposited on the electrode via drop cast and LB technique.

The data presented in Table 3.2 show zero concentration response in the capacitance (C) for both drop cast film and LB deposited film of ODA-CNT. However, further analysis for different acetone concentrations shows lack of consistency and an erratic behavior in the capacitance response of drop cast film of ODA-CNT. Therefore, due to the unpredictable nature of the obtained results, drop cast film of ODA-CNT are not suitable for acetone sensing, whereas, a systematic monotonic decrease in the capacitance (C) with increasing acetone concentration is observed in case of LB film of ODA-CNT. The resistance values for drop cast film of ODA-CNT also showed a high initial response but as the concentration is increased irregular response was observed. In case of LB deposited ODA-CNT film, the resistance value showed merely $0.7\ \%$ change. Thus, the parameter resistance is not a suitable choice for acetone sensing.

In case of LB films of ODA-CNT deposited on IDE, the nanotubes are aligned in the direction of the field (Fig:-3.8(a)). This can be treated as a combination of capacitors in series (Fig:-3.8 (a)) with aligned nanotubes. In the presence of electric field, the charge distribution and charge conduction pathways are coherent due to the aligned nanotubes. Hence, under this condition all the capacitor segments can record a similar increase in the capacitance value due to increase in acetone concentration. Therefore, the effective capacitance of the IDE deposited with LB film of ODA-CNT decreases with increasing concentration of acetone. However, in case of randomly oriented nanotubes in the drop cast film (Fig:-3.8 (b)), the charge conduction pathways and the charge

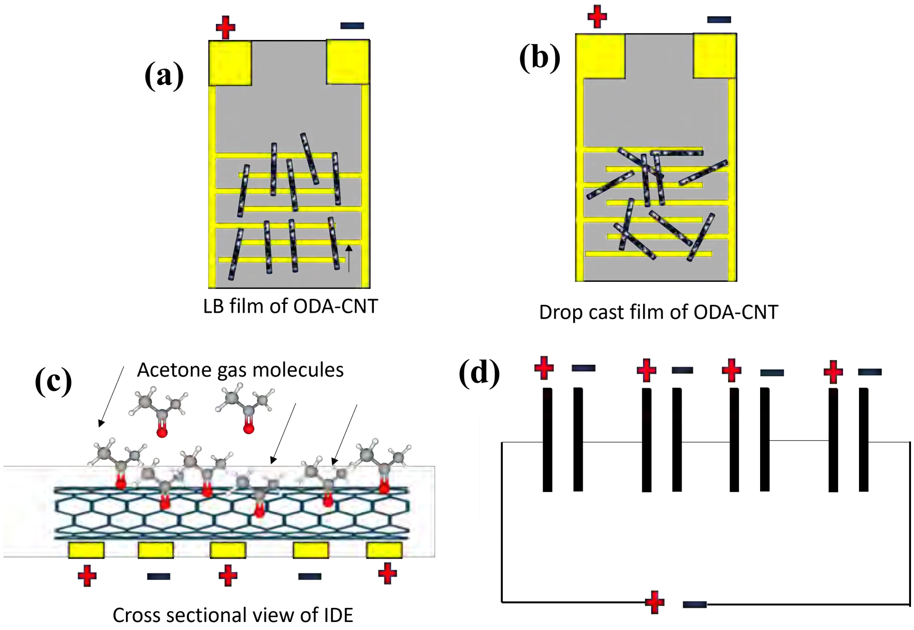

Figure 3.8: Schematic of sensing mechanism. (a) LB film of ODA-CNT aligned on the IDE, (b) drop cast film of ODA-CNT with random orientation on IDE, (c) cross sectional view of IDE with aligned nanotubes, (d) IDE modeled as capacitors in series.

distribution on the surface of nanotubes are random. Therefore, the change in the capacitance value from each capacitor segment is not coherent and hence, the effective capacitance was found to be random due to adsorption of the acetone. Therefore, we observed random change in the capacitance value in case of drop cast film of ODA-CNT as shown in Table-3.2

In order to further investigate the electrical characteristics of drop cast film and LB film of ODA-CNT, the normalized capacitance (C_m) and resistance (R_m) values for different concentrations of acetone is plotted and compared as shown in Fig:-3.9. The C_m values obtained LB film of ODA-CNT increases monotonically and significantly with increasing concentration of acetone vapor as compared to that of drop cast film of ODA-CNT and LB film of pristine-CNT. The adsorption of acetone molecules is efficient on the surface of CNT in the LB film. Further, R_m from the simulated Nyquist plot was also compared and shown in Fig:-3.9 (b) for drop cast and LB film. The change in R_m values for all the films was found to be random and negligible and thus cannot be taken forward as a parameter for sensing measurement. The change in capacitance and the resistance responses from LB film of pristine-CNT were found to be minuscule (Fig:-3.9). Thus it can be inferred that although the same deposition mechanism, the ordering and uniformity of nanotubes in the LB film plays crucial role in yielding superior sensing performance towards sensing

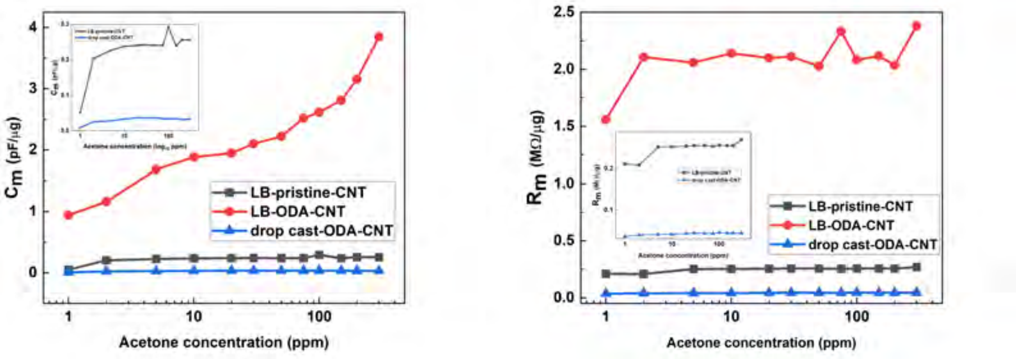

(a) (b)

Figure 3.9: Comparison of (a) normalized capacitance (C_m) and (b) normalized resistance (R_m) of drop cast ODA-CNT, LB-ODA-CNT and LB pristine-CNT films with respect to different concentrations of acetone.

acetone vapor. Further, we also performed the recovery test for drop cast and LB film of ODA-CNT. The capacitance as function of frequency was measured after the sensing measurements were completed. The used IDE chip was kept in open environment for 15 minutes and the gas chamber was flushed with nitrogen gas jet. The impedance measurement were once again performed and the observed capacitance value is shown in the Fig:-3.10 for LB and drop cast film of ODA-CNT.

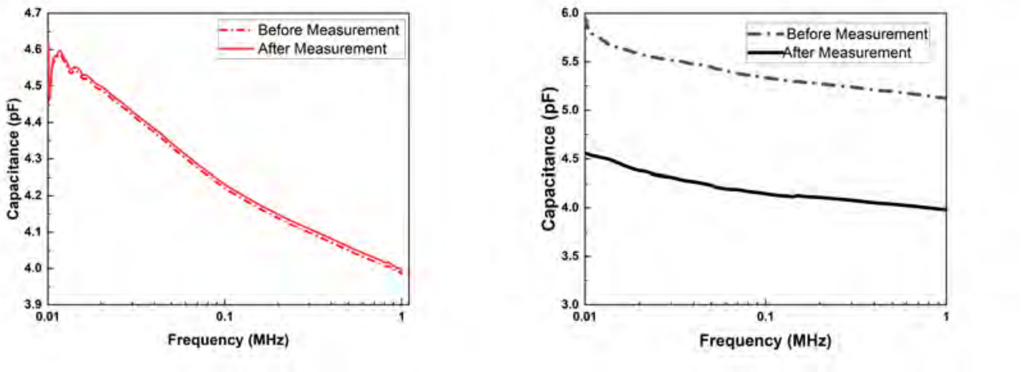

(a) (b)

Figure 3.10: Comparison of capacitance data before and after the sensing measurement (a) LB film (b) drop cast film of ODA-CNT.

From Fig:-3.10 it can be observed that the capacitance values for LB film of ODA-CNT are recovered and negligible hysteresis of 2% was observed, whereas in case of drop cast film the hysteresis was about 25% of the reference value. Thus, it can clearly be stated that the LB films can be used multiple times for acetone sensing.

3.4 Conclusion

The Langmuir monolayer of ODA-CNT at the A/W interface was found to be very stable and it exhibited gas and liquid-like phases. A single layer of LB film of the ODA-CNT deposited in the liquid like phase revealed aligned nanotubes at the A/S interface. Being a reducing agent, acetone can interact with CNT effectively through transfer of electrons. The single layer of ultrathin film of ODA-CNT can act as a suitable functional layer for the sensing of acetone vapor. The sensing of acetone using the LB film of ODA-CNT was compared with that of drop cast film of randomly oriented ODA-CNT. Using the IS, multiparameters viz. capacitance, conductance, impedance, phase difference and quality factors were recorded as a function of frequency for different acetone concentration. The PCA on the data revealed capacitance to be most appropriate parameter for efficient sensing of acetone using the LB film of ODA-CNT. The 2D calibration map of capacitance shows a systematic linear variation for the LB film of ODA-CNT as compared to that of drop cast and LB pristine-CNT film. The equivalent circuit was fitted and the estimated values of resistance and capacitance for drop cast and LB film was tabulated. This study indicated that the LB film of ODA-CNT can be potentially used for the sensing of acetone vapor even at the room temperature exhibiting a wider concentration range (1 - 300 ppm) with a LOD of 0.5 ppm. The superior sensing performance of the LB film of ODA-CNT is attributed to the aligned nanotubes on the IDE, leading to a coherent behavior due to interaction with the acetone molecules. Another interesting carbon based nanomaterial is graphene. In the next chapter, we study the ultrathin film of functionalized graphene and its capabilities for bacteria sensing. We retain the similar functionalization as that of ODA-CNT because the amine functionlization can interact efficiently with the harmful gram-negative bacteria.

CHAPTER 4

Ultrathin film of functionalized graphene for bacteria sensing.

In the previous chapter, we observed enhanced sensitivity of acetone vapors due to LB aligned ultrathin film of ODA-CNT as compared to randomly distributed ODA-CNT and LB film of pristine-CNT. Due to ODA functionalization, CNT were homogeneously dispersed at the A/W interface and aligned when transferred onto the substrate. The aligned film showed enhancement in sensitivity, due to larger number of adsorption sites for acetone molecules. Apart from gas sensing such as acetone and other volatile gases for health monitoring, carbon nanostructures have been significantly employed in bacteria testing for environment monitoring. Graphene, especially have been one of the major nanomaterials employed for bacteria sensing in water bodies and bio-hazard materials.

In this chapter we will discuss LB films of ODA-functionalized graphene in the ultrathin regime and its application for water borne bacteria sensing. We have employed electrochemical impedance spectroscopy for sensing measurement for both gram negative and gram positive bacteria. We have also employed machine learning on the raw impedance data for wide frequency range and observed selective response in case of E. coli.

4.1 Introduction

Graphene has outstanding electronic and physicochemical properties which has played key role in fabrication of biosensing devices and probes[26, 124]. Graphene possess extraordinary properties such as large specific surface area, biocompatibility, optical characteristics, electrical conductivity, and thermal conductivity[125]. The delocalized π electrons of the graphene can attract and trap the bio-molecules through $\pi - \pi$ interaction. Graphene exhibits the capability to interact with a diverse array of organic molecules through non-covalent forces such as hydrogen bonding, electrostatic force, van der Waals force, and hydrophobic interaction[126–128]. The sensing mechanism involves converting the interaction of target molecules, biochemical processes, physiological and pathological reactions to generate measurable outputs across the graphene surface[124]. This versatility is crucial in fabrication of wide array of sensors.

Pristine graphene is difficult to disperse in water due to its inherent hydrophobic nature. Therefore, it is often necessary to functionalize it with organic molecules to improve its dispersibility in aqueous solutions. Functionalization of graphene with various species, such as inorganic nanoparticles, organic molecules, and biomolecules which modifies the surface chemistry of graphene, also increases its biosensing efficiency[127, 129–131]. Few reports have showed enhanced sensing performance by single layer of graphene as compared to that of bulk films[53, 132]. Poonia et.al[53] observed that the ultrathin LB films of carboxyl modified graphene showed enhanced performance for urea in aqueous medium as compared to that of spin coated thick film. They proposed that the lowest detectable concentration of urea using LB film of G-COOH (8.3 M) is about 5 times lower than that of spin coated film (41.6 μM) and at the same time the sensitivity due to LB film (42.5 ng/cm^2/μM) is about 3 times better than that of spin coated film (12.9 ng/cm^2/μM).

Biosensors based on bacterial detection has experienced exponential growth in recent years, finding applications in diverse scientific fields such as environmental monitoring, food quality assessment, clinical diagnosis, and biological agent identification. Globally, bacterial contamination in various mediums remains a primary cause of hospitalizations and fatalities, surpassing other sources such as viruses and chemicals[54, 55]. Despite ongoing efforts, the annual reduction in deaths attributed to pathogenic bacterial infections stands at only 1$\%$, with a projected 13 million deaths by 2050[56]. Additionally, the potential use of pathogenic bacteria as biological weapons is a significant concern in the scientific community[57, 58]. Among the pathogenic bacteria, Escherichia coli (E. coli) is a quite important foodborne or water-borne infectious pathogen of global concern, as well as the most common and lethal serotype of enterohemorrhagic bacteria[133]. In addition, contamination of water sources with these pathogenic bacteria is a big problem in both developing and developed countries[134, 135]. Infants, children, immunocompromised individuals, and the elderly are the most vulnerable to waterborne infections. Ingestion of as few as 10 organisms can result in life-threatening symptoms. Also E. coli have been recommended as indicators of microbial contamination risk in water[136]. Therefore, establishing the effective and rapid detection of E. coli is really critical for diagnostic platform. The existing techniques for detecting E. coli, such as the colony-counting method, involve number of tiresome procedures, demand skilled personnel, and time taking[137]. After bacteria plating, a routine biochemical identification process ensues, involving a plethora of tests like the catalase test, citrate test, Gram staining, and methylene red staining. Newer molecular diagnostic methods based on amplification, such as polymerase chain reaction (PCR), have the potential to shorten assay times to a matter of hours. Nevertheless, these techniques still lacks the sensitivity required for detecting bacteria at low concentrations («1–100 colony-forming units per mL (CFU/mL) of the sample) and still involve considerable time and labor[138]. Newer technique such as labelled sensors where a biorecognition element such as DNA, antibodies, aptamers, antimicrobial peptides, and phages are coated over sensing material to improve the selectivity and sensitivity of the sensing analyte. It requires sample pre-processing procedure, which is time consuming, expensive and laborious[139, 140]. Optical techniques such as surface plasmon resonance, Localized surface plasmon resonance, surface-enhanced Raman scattering, surface-enhanced infrared absorption and/or surface-enhanced fluorescence spectroscopy have also been employed for bacteria sensing. However, the major drawback for these optical technique is possibility of peak deflection on encountering a strong EM field by a sensitive biological sample[141]. Also, these instruments are lab based and bulky instruments and may not be used on field. Therefore, an easy to use, label free, highly sensitive and selective sensing mechanism must be employed. EIS is one such technique. The powerful frequency function for measuring dielectric properties EIS is well received for possible label free procedures, high sensitivity and cost effectiveness. It relates the various important complex physical properties such as diffusion, double layer capacitance formation and interfacial interaction of the analyte with the electrode via fitting a circuit model. In a report by Jijje et.al[142], authors used gold electrodes modified with thin active layers of reduced graphene oxide/polyethylenimine/ pyrene-polyethyleneglycol (rGO/PEI/p-peg) and further was covalently modified with anti-fimbrial E. coli antibodies to detect $10^1 - 10^4$ cfu/mL E .coli bacteria. They performed the sensing in presence of redox probe potassium ferrocyanide to enhance the charge transfer. Gupta et.al[143] proposed amino functionalized graphene oxide further the electrode was covalently modified with antibody and observed the sensing in the range of $2 \times 10^2 - 10^8$cfu/mL. Wang et al. used Au modified graphene on paper electrodes which immobilized with the antibodies to get the detection limit of 1.5×10^2. Thus, a label free and selective EIS sensing of E. coli for a wide range is still not significantly explored. Therefore, in this chapter we are proposing a label free and selective sensing of E .coli. We have employed LB films of Octadecylamine functionalized graphene (ODA-gr) deposited on gold electrodes for a wide range of concentration ($10^1 - 10^6$cfu/mL). The amine group on ODA binds with carboxyl groups on graphene, and enhance the electroactive surface area and facilitates in electrostatic interaction with pathogen[144]. We have performed the EIS measurements of 6 different bacteria, three from each gram negative and gram positive family to check the selectivity. The lowest detectable concentration observed in the case was 2.5cfu/mL for E. coli. In EIS usually, the sensitivity is characterized on the basis of the components used in circuit fitting. Although, it is necessary to understand the mechanism and interpret the interaction between the analyte and modified electrode, it is time consuming and require scientific personal to deal with the data procurement. Therefore, in addition to the EIS circuit fitting analysis we have also employed various Machine learning (ML) algorithms to aid selective detection of E. coli. ML based sensing data analysis offers quick and removes any fitting and human error while data analysis. Here, raw impedance magnitude with respect to the input frequency data for all the 6 bacteria for different concentrations was fed into the ML classification algorithms to check for the E .coli sensing response. This work is applied for Indian patent [145].

4.2 Experimental

LB film preparation: A stock solution of 0.05 mg/mL ODA-gr was prepared in absolute ethanol. The Langmuir film at the A/W interface were formed by spreading 500 μL solution on the subphase between the two barriers of Langmuir trough (KSV-NIMA). The system was left undisturbed for 30 minutes to allow the solvent to evaporate to get a homogeneous spreading of ODA-gr. Further, surface pressure-area isotherm was recorded . The surface phases of the Langmuir film were observed using KSV-nIMA Micro-BAM. The Langmuir film was then transferred on to the gold electrode via LB method at the target surface pressure(π_t) of 15 mN/m. The dipper speed was maintained at 1 mm/min. The target surface pressure was kept constant via controlled feedback mechanism of barriers for good transfer and homogeneous coverage of the film on the gold electrode.

Bacteria culture: The common and representative bacterial strains of bacteria as shown in Table:-4.1 were employed for sensing measurement.

Bacterial Strains	**Type**	**Source**
Staphylococcus aureus subsp. aureus MTCC1430T (S.A.)	Gram Positive	MTCC, IMTECH, Chandigarh, India
Bacillus cereus MTCC430 (B.C.)	Gram Positive	MTCC, IMTECH, Chandigarh, India
Bacillus subtilis MTCC121 (B.S.)	Gram Positive	MTCC, IMTECH, Chandigarh, India
Escherichia coli DH5 alpha MTCC1652 (E. coli)	Gram Negative	MTCC, IMTECH, Chandigarh, India
Pseudomonas fluorescens MTCC103T (P.F.)	Gram Negative	MTCC, IMTECH, Chandigarh, India
Legionella pneumophila subsp. pneumophila ATCC 33152-0211P (L.P.)	Gram Negative	Biomall

Table 4.1: Representative bacterial strains and their sources

The bacterial cultures were sub-cultured in suitable medium as per supplier's instructions. The viable cell count of each culture was determined using CFU count method and concentration of the culture was expressed as CFU/ml. Briefly, the freshly grown culture of bacteria was serially diluted and 100 μL of this culture was spread on solid media. After overnight incubation, the plates having a countable range of colonies were used for colony counting. The CFU number was further counted for each strain as per Sieuwerts et al.[146]. Further each bacteria culture were serially diluted to obtain a desired concentration for sensing measurements.

Sensing Measurement: EIS was utilized for sensing measurements in this study. LB deposited ODA-gr/Gold electrodes were served as the working electrode, while an Ag/AgCl electrode was employed as the reference electrode, and a Platinum wire as the counter electrode. The electrolyte utilized was a 10X phosphate-buffered saline (PBS). Subsequently, each bacterial culture was added sequentially to the electrolyte, and impedance measurements were conducted across a frequency range of 10 mHz to 1 MHz for each concentration.

4.3 Results and discussion

The Langmuir film of ODA-Gr was formed at A/W interface and corresponding surface pressure π vs area isotherm was recorded as shown in Fig:-4.1.

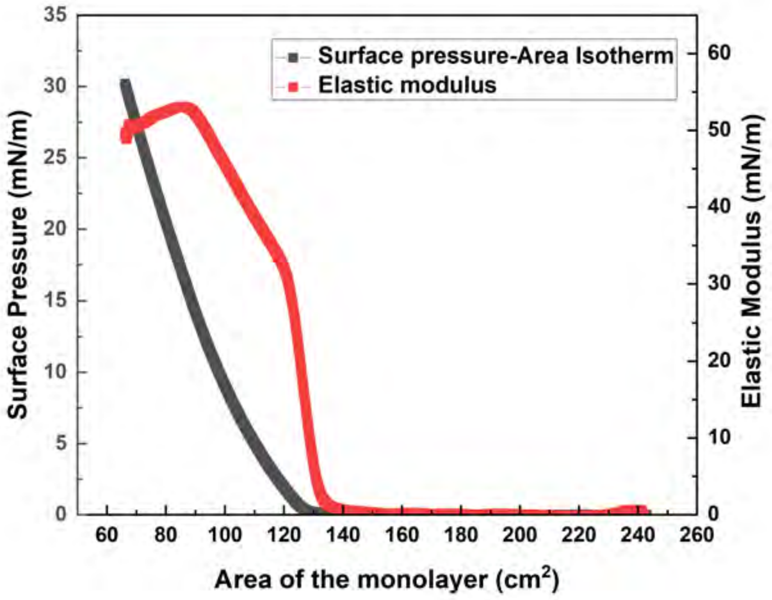

Figure 4.1: Surface pressure-area isotherm and in plane isothermal elastic modulus for ODA-gr.

The surface pressure remains negligible upto $127cm^2$. The region for negligible surface pressure indicates the gas like phase. On compression of the film below $127cm^2$, the surface pressure rises steeply. This is the onset of liquid-like phase. The classical signature of collapse was not observed in this case.

Isothermal in-plane elastic modulus was also calculated as per the relation: $|E| = \left|-\frac{1}{A}\frac{d\pi}{dA}\right|$

The elastic modulus is calculated to identify any weak phase transitions in the Langmuir monolayer at the A/W interface. It also reveals the elastic nature of monolayer at a given phase. From Fig:-4.1, a change in slope at area $\approx\ 130\ cm^2$ was observed. Further compression of the monolayer upto area $\approx\ 90\ cm^2$, again a slope change is observed in the elastic modulus. This might be the initiation of the collapse of Langmuir film of ODA-gr. Here the collapse is very weak to observe significant change in the surface pressure-area isotherm. The graphene layer may undergo stacking in the collapsed state.

Further, BAM was employed to study the surface phase of Langmuir film formed at the A/W interface. BAM images were captured at different surface pressures as shown in Fig:-4.2.

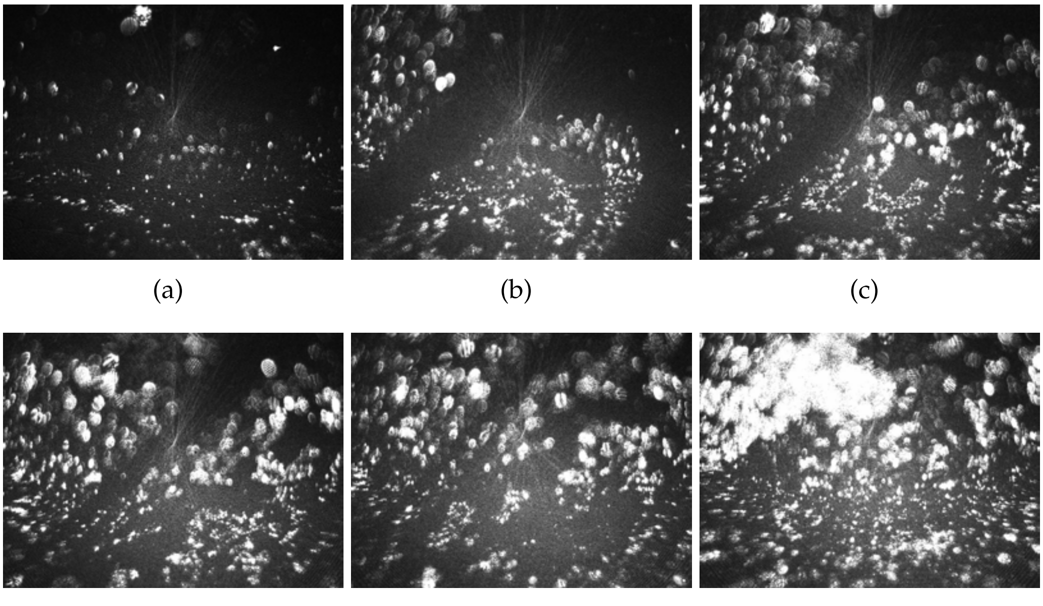
(a) (b) (c)

(d) (e) (f)

Figure 4.2: BAM images at surface pressure; (a) 0.5mN/m (b) 2mN/m (c) 5mN/m (d) 10mN/m (e) 15mN/m (f) 25mN/m. The size of the images is 3.5 mm × 4 mm.

A gray uniform texture is observed in the background with some bright domains were observed in almost all the BAM images. The brightness of the gray texture increases with increasing surface pressure. The bright domains are due to the stacking of graphene layer. As the surface pressure increase, number of stacked domain also increases. At 25 mN/m, very bright domains represent the highly stacked graphene layer.

Further, the Langmuir film was then transferred from the A/W interace at the target surface pressure of 15 mN/m on to the gold electrodes via LB method. The morphology of the LB depsoited graphene monolayer was studied via feild emission scanning electron microscopy (FESEM) as shown in Fig:-4.3. The FESEM image of the LB film of ODA-gr clearly indicates the domain corresponding to the graphene monolayer, whereas the drop cast film of ODA-gr reveals graphen flakes with random 3D network.

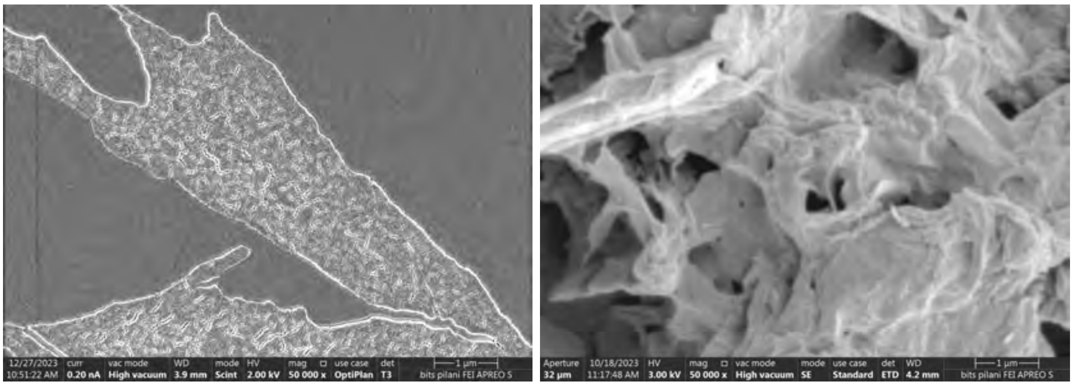

(a) (b)

Figure 4.3: FESEM images of (a) LB and (b)drop cast film of ODA-gr.

Further, fresh LB films of ODA-gr were used for sensing measurements of Gram-positive and Gram-negative bacteria using EIS. The EIS observations of the LB-fabricated ODA-gr film were recorded as a reference. The cultured bacteria were serially diluted in PBS. Bacteria were then introduced into the PBS electrolyte in increasing concentrations. For each sample injection, EIS measurements were recorded for different concentrations of the six bacterial cultures. Fig:-4.4 (a) shows the schematic representation of serial dilution process and (b) lab assembled EIS measurement setup.

The impedance response for different concentration along with the corresponding circuit employed for the fitting of the observed data for each of the bacteria is shown in Fig:-4.5.

The impedance observation showed unique response for E. coli as compared to rest of the bacteria. A complete semicircle is observed in rest of gram-

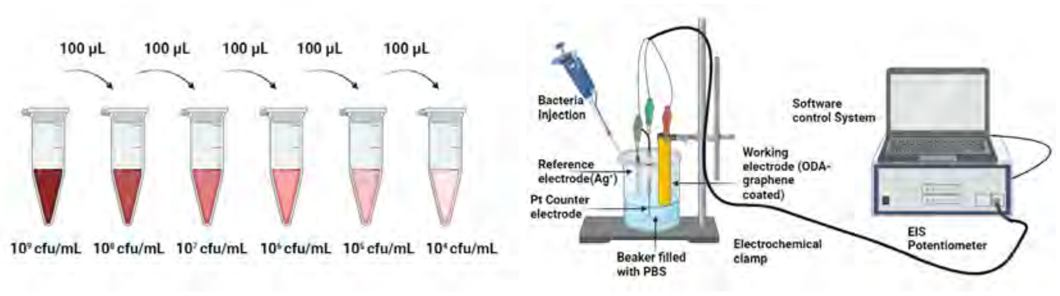

(a) (b)

Figure 4.4: (a) Serial dilution for freshly cultured bacteria.(b) Schematic of Lab assembled EIS setup for sensing measurements.

negative and gram-positive bacteria, whereas a half semicircle is observed in case of E .coli. In gram-negative bacteria(P.F and L.P), a small tail is also observed which is absent in the impedance response of gram-positive bacteria. Thus, the circuit employed for fitting the data of E. coli, other two gram negative bacteria (P.F and L.P) and the three gram positive bacteria are different. From Fig:-4.5, it was observed that the magnitude of impedance for E. coli(Fig:-4.5 (a) is 10^3 times greater than the impedance magnitude of rest of the bacteria. The impedance response for E. coli with respect to its concentration is also systematically decreasing. Although, E. coli belongs to gram-negative family the peptidoglycan layer in E. coli is mono-molecular thick when compared to the other gram negative bacteria($\approx 10\ nm$). Therefore, when E. coli comes close to graphene, due to the antibacterial property of graphene and the metabolic activity of E. coli, outer layer of the bacteria is ruptured. The outer layer breakdown releases weak organic acids in its extra cellular environment. Such acids alters the pH in the nanoregime gap between the E. coli bacteria and graphene layer. Due to the rupture of outer membrane, inner constituents of the bacteria deposit a conducting layer over the graphene surface which in turn increases the conductance of graphene film . As the concentration of E. coli is increased , the thickness of the resultant layer also increases which ultimately is observed as a systematic increase in the conductance of graphene film. The resistance and capacitance of the resultant layer is modeled as $R1$ and $C1$ respectively in circuit shown in Fig:-4.5 (a). Apart from the metabolic activity of E. coli that deposits a layer on the graphene, the long hydrophobic ODA-chain in

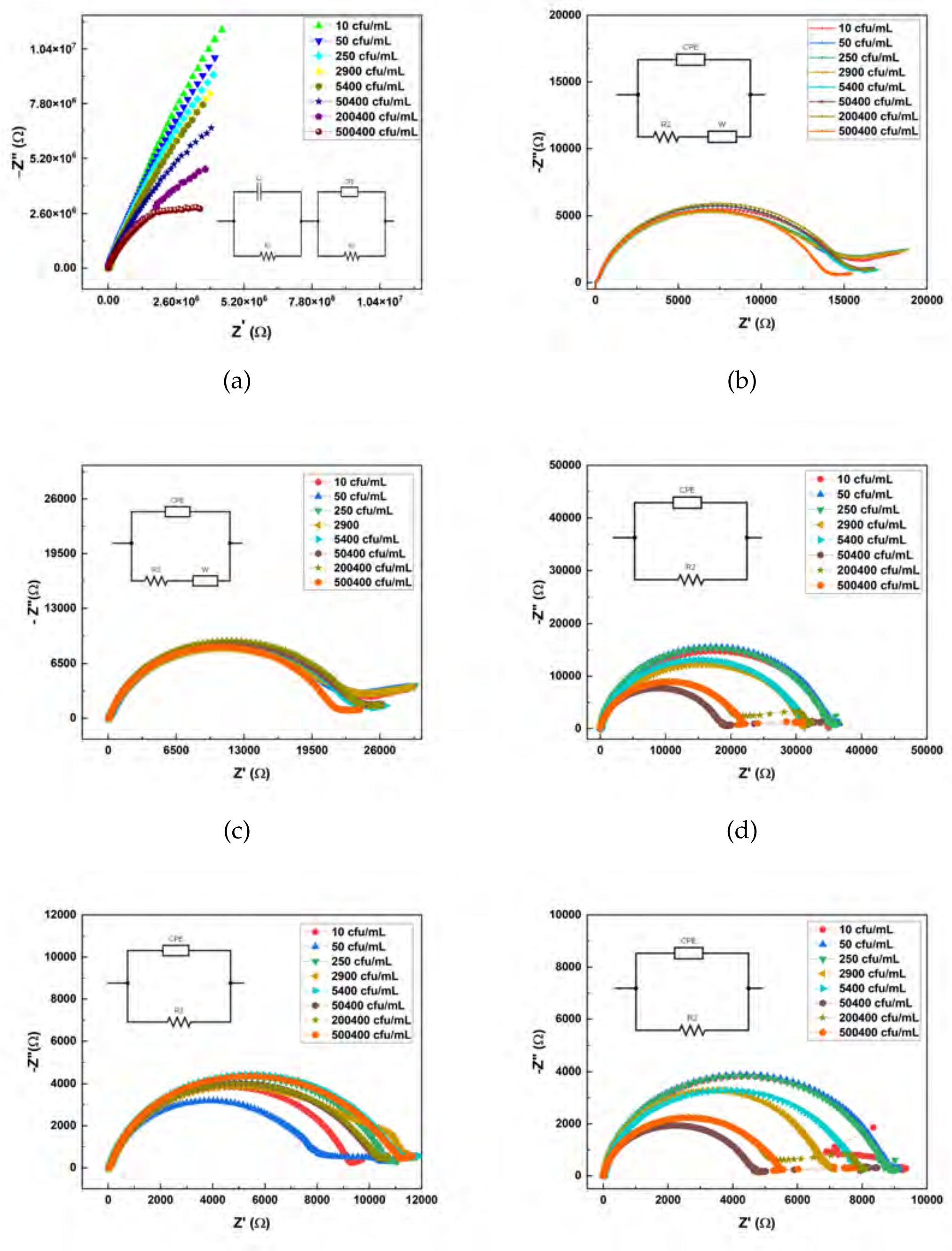

(a) (b) (c) (d) (e) (f)

Figure 4.5: Nyquist plot for wide range of concentration along with the circuit employed for data fitting(inset) for (a) E. coli (b) P.F. (c)L.P. (d) B.C. (e) S.A. and (f) B.S.

graphene has also an important role in the interaction. Due to the presence of negatively charged outer cell membrane in E. coli and highly negative zeta potential, electrostatic interaction takes place between the positively charged ODA-chain and the cell wall of the bacteria. Due to the electrostatic interaction a pseudocapacitance (CPE) formation also takes place. This electrostatic interaction also helps in the charge transfer ($R2$) of such bacteria in the electrolyte. Therefore, to model the two different types of interaction two parallel R-C circuits were employed to model the impedance response as shown in Fig:-4.5 (a). In the other two gram-negative bacteria, the outer memebrane is comparatively thick, thus only pseudocapacitance (CPE) formation and charge transfer (R2) occurs at the electrode surface. Thus, in Fig:-4.5(b, and c), a single parallel RC circuit is employed to model the electrostatic interaction.

Further, in case of P.F. and L.P, although they belong to gram negative strain family, a small tail at lower frequency is observed which suggests polarization of charged species. The tail part at the lower frequency is due to the redistribution of surface charges of the bacteria. In this case as the outer membrane was intact, the surface charge gets redistributed and contributed in the formation of polarization of charge only. Thus, the circuit employed for fitting them also has a Warburg element (W) to account for the diffusion of the charged species in the sensing environment.

In case of gram positive family (S.A., B.C. and B.S.) the Nyquist plot and the circuit employed for fitting suggest only the formation of pseudocapacitance and charge transfer. The gram positive bacteria undergoes electrostatic and hydrophobic interaction with the long ODA chain of graphene. Gram positive bacteria predominantly exists in large multicellular clusters. Hence, the unusual transitions in the impedance profile is most likely be attributed to clustering and biofilm formation, where correlation between the signal and CFU counts is completely lost due to loss of unicellularity. Furthermore, gram positive baceteria are mostly non-motile and gets accumulated on the sensor surface and tend to form islands of microcolonies, supplying negative charge to the ODA functionalized graphene thereby bringing the system closer to charge neutrality, which should lead to monotonic change in impedance response. However, the charge doping from the microcolonies is not spatially

Bact. conc. (c.f.u/mL)	E. coli				P.F.			L.P.			S.A.		B.C.		B.S.	
	R_1 (MΩ)	C_1 (μF)	C_{cpe} (μF)	R_2 (MΩ)	C_{cpe} (μF)	R_2 (kΩ)	W (kΩ)	C_{cpe} (μF)	R_2 (kΩ)	W (kΩ)	C_{cpe} (μF)	R_2 (kΩ)	C_{cpe} (μF)	R_2 (kΩ)	C_{cpe} (μF)	R_2 (kΩ)
10	74.30	1.62	1.27	8.66	4.00	15.30	0.69	2.56	23.9	1.09	2.50	9.36	1.57	35.0	2.50	8.91
50	56.00	2.12	1.37	8.32	4.26	14.80	0.81	2.73	23.10	1.27	7.13	10.26	1.54	35.7	7.13	8.92
250	51.6	2.34	1.36	7.60	4.77	15.2	0.82	3.05	23.7	1.29	3.39	10.79	1.53	35.30	3.39	8.82
2900	41.10	2.64	1.41	6.37	5.02	15.00	0.77	3.21	23.4	1.22	6.48	11.38	2.10	31.2	6.48	7.01
5400	34.30	2.7	1.47	6.21	4.08	15.20	0.33	2.61	23.70	0.52	5.48	11.43	2.34	31.8	5.48	7.95
50400	20.30	2.92	1.56	4.76	3.98	15.20	0.33	2.57	23.90	0.53	5.57	10.89	2.36	25.8	5.57	6.57
200400	9.66	3.06	1.81	2.10	3.62	15.4	0.34	2.32	23.99	0.54	5.98	10.50	2.84	21.8	5.98	5.42
500400	6.66	3.88	2.09	1.68	3.56	14.00	0.34	2.28	21.82	0.37	5.35	11.27	2.92	21.8	5.35	5.44

Table 4.2: The observed values of the circuit components used in fitting of Nyquist plot for all six bacteria culture. Here, C_{cpe} is the value of capacitance observed in the constant phase element (CPE) during EIS fitting.

uniform in graphene resulting in a non-linear response. Table:-4.2, shows the parameter values obtained after circuit fitting.

From the Table:-4.2 it is evident that in case of E. coli, the resistance (R_1) has monotonic decrease which states that with increase in bacteria concentration the conductance at the electrode interface increases. Therefore, it signifies that with the introduction of E. coli bacteria, conductance of the graphene film increases.

Further, we investigated different machine learning (ML) algorithms at disposal to check for the appropriate classification of the bacteria strain based on the raw impedance data. The algorithms were directly imported from the scikit learn python module. The raw data was split into training and testing sets, where 80% of the data was used for training a machine learning model, and 20% was used to evaluate its performance. Table:-4.3 shows all the tested ML algorithms for the classification and the prediction accuracy are compared.

Bagging classifier and Decision tree were comparatively more suitable algorithm for the classification for our data with *83 %* and *77 %* accuracy respectively. It is also evident that most of the ML classifiers predicted E. coli better compared to other five bacteria. The multiclass classification for the 6 bacteria for the best classifier is shown in the confusion matrix in Fig:-4.6.

Fig:-4.6 shows the confusion matrix for the best classification algorithm for our data i.e. Bagging classifier. In the confusion matrix obtained, we observed that E. coli has all true positive values and zero false positives, i.e 616 values were correctly classified in the class of E. coli and not a single data were

Classifier	Bacteria type	Precision	Recall	F1-score	Classification Accuracy
Random Forest	B.C.	0.44	0.47	0.45	71%
	S.A.	0.92	0.91	0.91	
	P.F.	0.59	0.54	0.57	
	E. coli	**1**	**1**	**1**	
	L.P.	0.84	0.78	0.81	
	B.S.	0.51	0.57	0.53	
Support Vector Machine	B.C.	0.06	0.01	0.01	20%
	S.A.	0	0	0	
	P.F.	0	0	0	
	E. coli	**0.86**	**0.29**	**0.43**	
	L.P.	0.15	0.08	0.1	
	B.S.	0.17	0.9	0.28	
K Nearest Neighbours	B.C.	0.19	0.37	0.25	35%
	S.A.	0.43	0.42	0.42	
	P.F.	0.24	0.23	0.24	
	E. coli	**0.95**	**0.62**	**0.75**	
	L.P.	0.41	0.21	0.27	
	B.S.	0.29	0.27	0.28	
Decision Tree	B.C.	0.55	0.56	0.55	77%
	S.A.	0.92	0.91	0.91	
	P.F.	0.68	0.65	0.66	
	E. coli	**1**	**1**	**1**	
	L.P.	0.85	0.81	0.83	
	B.S.	0.64	0.69	0.66	
Gradient Boost Accuracy	B.C.	0.28	0.26	0.27	67%
	S.A.	0.43	0.13	0.2	
	P.F.	0.31	0.28	0.29	
	E. coli	**1**	**0.49**	**0.66**	
	L.P.	0.23	0.42	0.29	
	B.S.	0.3	0.46	0.36	
Bagging Classifier	B.C.	0.69	0.7	0.69	83%
	S.A.	0.94	0.95	0.94	
	P.F.	0.73	0.73	0.73	
	E. coli	**1**	**1**	**1**	
	L.P.	0.93	0.94	0.93	
	B.S.	0.71	0.72	0.72	
Gaussian Naive Bayes	B.C.	0.52	0.18	0.27	26%
	S.A.	0.19	0.68	0.3	
	P.F.	0.08	0.01	0.02	
	E. coli	**0.93**	**0.25**	**0.4**	
	L.P.	0.27	0.34	0.3	
	B.S.	0.21	0.06	0.1	
Multilayer Perceptron Neural Network	B.C.	0.42	0.26	0.32	34%
	S.A.	0.27	0.58	0.37	
	P.F.	0.5	0.09	0.15	
	E. coli	**0.91**	**0.37**	**0.53**	
	L.P.	0.36	0.32	0.34	
	B.S.	0.25	0.46	0.32	

Table 4.3: Different ML classifiers and their prediction parameters for the raw impedance data for six bacteria culture.

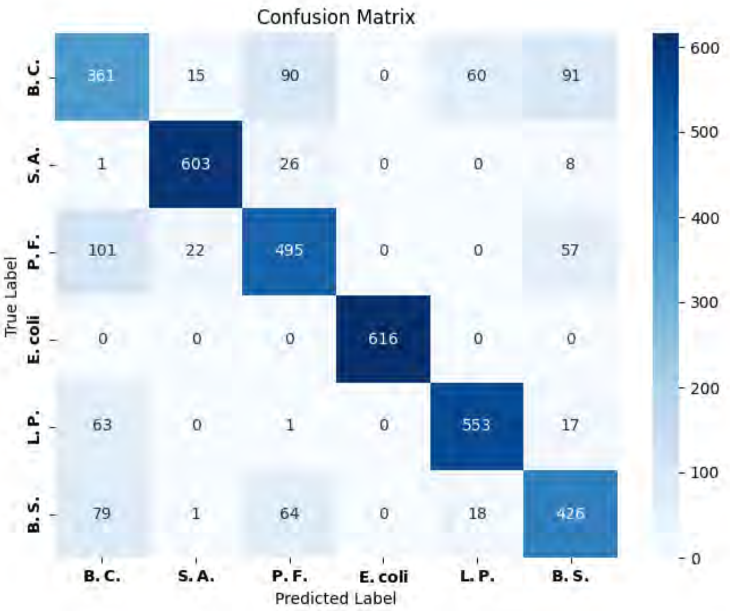

Figure 4.6: Confusion matrix for Bagging classifier

wrongly classified. The second best classification were observed for S.A where, 603 values were correctly classified, but 26 of the values were misinterpreted with P.F. which is from gram-negative family. The worst classification was for B.C. as it had least true positives predicted and it has false positives for all the bacteria except for E. coli. Thus, from Fig:-4.6 we can conclude that using machine learning also we can easily classify or selectively detect E. coli based on their raw impedance response. The application of ML algorithm will save the analysis time and the possibility human error if trained with data rigorously.

4.4 Conclusion

In this chapter we observed that ODA-graphene forms a very stable Langmuir monolayer at the A/W interface. The transferred LB film were homogenously distributed as flakes on the substrate which can increase its S/V ratio. The LB film was transferred onto the gold electrodes and were employed for bacteria sensing. The bacteria procured were freshly cultured in appropriate conditions and then serially diluted before sensing measurements. Six different bacteria, three from each gram-negative and gram positive family were tested. It was observed that the employed ultrathin film proved to be highly selective for E. coli for a wide range of concentration(10 -10^6 cfu/mL). The lowest detected concentration was 2.5 cfu/mL. We observed that due to the monomolecular thin outer cell wall of E. coli, when it comes in contact with graphene surface, the cell wall gets ruptured and the constituents gets adsorbed on the graphene surface and the conductivity of the film increases significantly. Thus we employed different circuit models to understand the physical phenomena of the interaction for all the six bacteria. We also employed different ML algorithms to verify our findings. We applied most of the unsupervised ML algorithms and observed Bagging classifier and Decision tree were best suited for the data observed. The ML algorithms can help in minimizing the analysis time and possibility of human error while circuit fitting and data extraction.

CHAPTER 5

Role of anisotropy, surface coverage and alignment of functional layer on SPR.

In the preceding chapter, we investigated the water borne bacteria sensing and observed that ODA-functionalized graphene has highly selective and sensitive response for E. coli. Apart from impedance based techniques, there are several other techniques which are employed for biosensing. Optical techniques such as SPR, offers label free and highly sensitive response for such bio analytes. In SPR, the required sample volume is very low and it records very minuscule changes in the refractive index at the metal/dielectric interface. The change in the refractive index depends on the bio affinity of the active layer. The typical metallic film such as gold offers low affinity towards biomolecules in aqueous environment and poor FOM. The immobalization of ligands on metallic surface enhances the affinity, however it reduces the perceptibility of the SPR sensor significantly. To overcome this, different types of suitable ultrathin film for the functionalization of gold film can be used for sensing using SPR. In this chapter we will discuss different types of ultrathin films and the effect of their intrinsic property on the SPR response.

5.1 Introduction

Surface plasmon resonance (SPR) is a widely used optical phenomenon known for its significant applications in sensing. SPR allows for highly sensitive and label-free detection of various biological and chemical analytes. The working principle of an SPR sensor involves detecting changes in the refractive index (RI) with high resolution due to molecular interactions. Surface plasmon polaritons (SPPs) are excited at a metal-dielectric interface by an incident electromagnetic wave traveling through a coupling medium with an RI greater than

1.0. Resonance occurs when the wavevectors of the incident wave and the SPP wave match, leading to maximum energy transfer from the incident wave to the SPP wave and resulting in the extinction of the characteristic incident electromagnetic wave from the spectrum.

The Kretschmann configuration is commonly used configuration in SPR, where a p-polarized monochromatic electromagnetic wave is directed at the metal surface through a coupling prism. To establish SPR, the angle/wavelength of incidence is varied, and the reflected intensity is recorded. At resonance, the reflected intensity reaches a minimum. This resonance angle/wavelength is unique for a specific metal-dielectric interface. During sensing, the adsorption of analytes at the metal-dielectric interface changes the dielectric properties and shifts the resonance condition. This shift can be precisely measured, allowing the corresponding change in RI to be calculated.

The sensitivity of SPR can be further enhanced by modifying the metal layer with a functional coating. This functional layer can improve both the sensitivity and, in some cases, the selectivity of the sensor. However, it is crucial that this functional layer is an ultrathin film. If the functional layer is too thick, SPPs generated at the metal interface might decay before they can interact with the biomolecules. This issue is especially pronounced for heavy biomolecules, such as proteins, as the SPP waves may not penetrate deeply enough to detect these molecules effectively.

Ultrathin films, usually just a few nanometers thick, enable the SPPs waves to interact directly with the target biomolecules without substantial decay. However, the intrinsic properties of these films can modify the SPR response. Therefore, it is crucial to thoroughly investigate these properties before incorporating ultrathin films as functional layers in SPR-based biosensors

In this thesis we have focused on two specific properties of ultrathin films that requires thorough investigation; anisotropy and surface density of the ultrathin film.

Anisotropy refers to the directional dependence of the physical properties of the ultrathin film. It can influence how the film interacts with incident p-polarizaed light. Anisotropic films might exhibit different refractive indices along different axes, leading to complex changes in the SPR response. Understanding these effects is crucial for optimizing the sensor's performance. SPR being highly sensitive for even a minute change in refractive index, the reference measurements become difficult. Thus, it is important to have detailed understanding about the effect of anisotropy of the ultrathin films on the SPR response before employing them for sensing studies.

Submonolayer coverage, on the other hand, involves the film being less than a full monolayer. This incomplete coverage can lead to non-homogeneous surface coverage of nanoparticles, creating hotspots or areas with varying density. While submonolayer films can enhance sensitivity by providing more reactive sites, they can also introduce inconsistency in the SPR signal. Therefore, it is important to investigate the dependence of surface density of nanoparticles in the submnolayer for reliable sensor response.

In the coming sections of this chapter, we will delve into the roles of anisotropy and submonolayer coverage in ultrathin films. We will explore how these properties influence the SPR response. By understanding these factors, we can better design functional coatings that enhance the sensitivity and selectivity of SPR-based biosensors, paving the way for more effective detection of biomolecules in various applications.

5.2 Role of anisotropy in ultrathin films for SPR measurements.

Anisotropy in thin film arises due to tilt of shape anisotropic molecules (e.g., rod-shaped calamitic liquid crystal molecules, organic molecules such as long chain fatty acids) with respect to surface normal which may yield in-plane nematic ordering. In a report by Devanarayanan et al.[147] the optical anisotropy in ultrathin films was estimated experimentally using the SPR phenomenon by measuring the shift in the resonance angle (RA) in directions perpendicular to each other in films that demonstrated varying degrees of optical anisotropy. The reported anisotropy in the ultrathin films was estimated from SPR angle measurements in randomly chosen orthogonal directions. The study showcased the importance of SPR in assessing the optical anisotropy of ultrathin films fabricated through conventional LB and self-assembly methods. The study shows the metallic and dielectric nature of the LB films of bundles of single walled carbon nanotubes (SWCNT) when the long axis of SWCNT are aligned parallel and perpendicular to plane of incidence, respectively. Furthermore, the Self-Assembled Monolayer (SAM) of Octadecyltrichlorosilane (ODT) with 30° tilt of the molecules demonstrated anisotropy in the real part of the refractive index, measuring approximately 0.24. On the other hand, the LB films of Cadmium Arachidate (CdSA) with 10° tilt, film exhibited anisotropy in the real part of the refractive index, approximately measuring 0.10.

The reports in the literature in general provide the value of birefringence of the bulk material; however, due to reduction of dimension of the material, the physical properties deviate largely from that of bulk. Therefore, measurement of physical properties of a material at the lower dimension is essential for material engineering followed by device fabrication. The physical properties of the low-dimensional materials like two-dimensional thin film depend on its thickness. Hence, a calibration curve is essential for quantifying the dependencies of a physical property on any such parameters. Since the SPR phenomenon can be potentially employed for the measurement of RI at a very high resolution, a small in-plane birefringence due to tilt of shape anisotropic organic molecules even in a single layer can be measured. Such film with tilted molecules may exhibit nematic ordering on the surface. Thus, we present a calibration surface showing the dependency of $\Delta\theta$ on Δn and thickness of the thin organic film. The calibration surface was obtained through simulation, and it was utilized for the estimation of Δn of single layer of LB films of cadmium stearate (CdSA) and 4'-octyl-4-biphenylcarbonitrile (8CB) molecules. The values of thickness and $\Delta\theta$ of the LB films of CdSA and 8CB were obtained from X-ray reflectivity and a home-built SPR instrument, respectively, and these values were used in the calibration surface for the estimation of the respective Δn.

5.2.1 Methodology

5.2.1.1 Experimental Methodolgy

The Kretschmann configured SPR instrument was developed in the laboratory [76]. The equipment utilizes 5 mW laser of wavelength 635 nm, coupling prism (RI=1.51) and a segmented photodiode as detector. The resolution and sensitivity of the equipment are 1.92 μRIU and 53°$/RIU$, respectively. The SPR chip consists of 0.5 mm glass plate (RI=1.51) deposited with 50 nm thick gold film through sputtering technique. The chemicals, stearic acid and 4'-octyl-4-biphenylcarbonitrile (8CB) were procured from Sigma-Aldrich. Both the molecules yield a very stable Langmuir monolayer at the A/W interface and are ideal systems for utilizing them for fundamental studies [73, 148, 149]. A single layer of LB film of CdSA deposited at 30 mN/m can yield an average molecular tilt of $\sim$10° with respect of surface normal [150] and similarly, that of 8CB deposited at 4 mN/m yields an average molecular tilt of $\sim$60° with respect to the surface normal [151]. A single layer of LB films of CdSA and 8CB were deposited onto SPR chips at target surface pressure of 30 and 4 mN/m, respectively using a LB trough (KSV-NIMA). The thickness of the LB films were measured by X-ray reflectivity (XRR) technique using a X-ray diffractometer equipped with thin film analysis unit (SmartLab, Rigaku).

5.2.1.2 Simulation Methodology

A finite difference time domain (FDTD) method was employed for the simulation of SPR phenomenon in the Kretschmann configuration using a commercial package of Lumerical [152, 153]. The FDTD method is highly reliable and advantageous over other techniques in solving Maxwell's equations for complex geometries of materials. The simulation setup is shown in the Fig:-6.1(a).

The simulation was carried out using a monochromatic plane wave source (L) having a wavelength of 635 nm. The perfectly matched layer (PML) boundary condition with steep angle profile of 12 layers was used in order to minimise reflection from the boundary as the wave enters into the layer. Linear discrete Fourier transform monitors were used to capture reflected and transmitted electric field at 350 nm away from the interface. The source was made to incident on the gold layer via glass medium at an angle of incidence of θ_i. In order to obtain the resonance angle, the incident angle sweep was generated from 40^o- 48^o with 251 iterations. The mesh override was selected in the propagation direction of the plane wave to get more precise results. The optical anisotropy was seen in case of a single layer of materials exhibiting geomet-

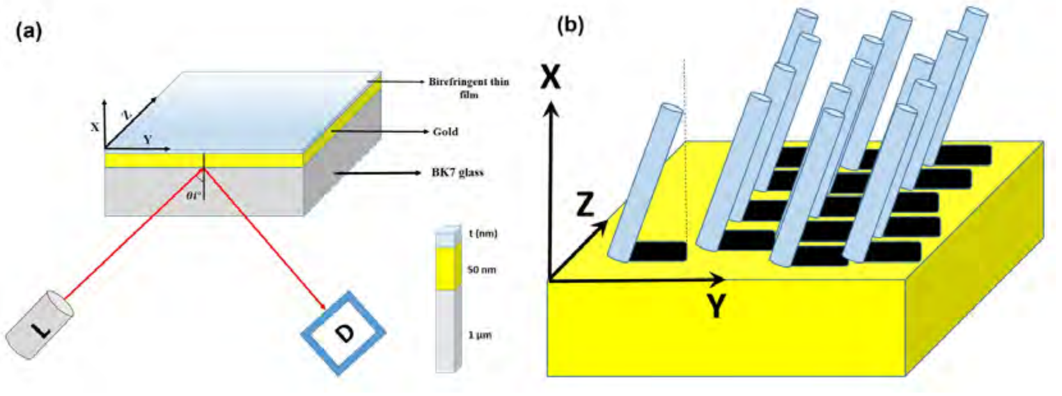

Figure 5.1: A schematic of (a) simulation setup showing the major components as depicted. The plane of polarization is XY. The angle of incidence of the monochromatic light (L) is θ_i, thickness of each material and detector (D) are shown and (b) a single layer of shape anisotropic molecules (rod shaped) tilted with respect to X-axis along Y-axis on the YZ plane. The projection of the molecules is shown in black. Such projection resembles nematic ordering on 2D plane with optic axis along Y-axis.

rical anisotropy at the molecular level. A common example of such system is shown schematically in Fig:-6.1(b). A single layer of rod shaped molecule (calamitic liquid crystal) tilted with respect to X-axis can have a projection on the YZ plane. If all the molecules are more or less tilted in the same direction (here it is along Y-axis), they exhibit a nematic-like ordering with optic axis (OA) parallel to the Y-axis. Another set of examples are single layer of self-assembled monolayer of rod shaped octadecanethiol or LB film of fatty acids [73]. To simulate such system of anisotropic material, we have modified our setup by integrating a rotation axis along X-direction, (Fig:-5.1) with a resolution of 0.1 degree to rotate the film deposited substrate and measure the SPR response in-situ as a function of angle of rotation of the film. This modification ensures alignment of optics for the measurement of birefringence.

5.2.2 Results

A p-polarized electromagnetic wave was incident at the glass-gold interface, as illustrated in Fig:-5.1. The resulting evanescent wave within the gold film has the potential to excite surface plasmon polaritons (SPP). Fig:-6.2(a) displays the surface plasmon resonance (SPR) curve for the gold-air interface, reveal-

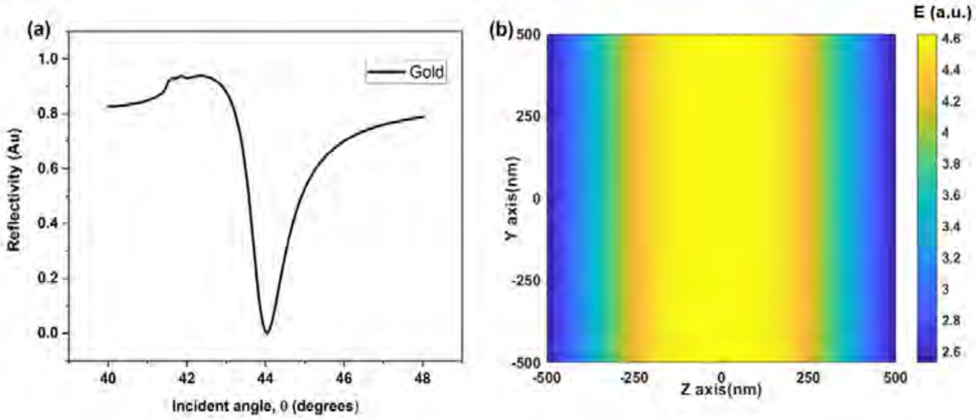

Figure 5.2: (a) SPR spectrum of gold-air interface (b) the electric field profile on the two dimensional gold surface (Y-Z plane) obtained from simulation.

ing a resonance angle (RA) value of 44°. The FDTD calculation derived SPR curve and RA value for the gold-air interface align with findings in the literature [154]. The 2D electric field profile due to surface plasmon polaritons at the resonance angle is depicted in Fig:-5.2(b). In the chosen geometry, the YZ plane corresponds to the gold-air interface, with the plane of polarization in XY. The field's surface distribution is identified as anisotropic. In a 1000 nm×1000 nm mesh size, the anisotropic nature of the plasmonic field is evident, suggesting that the excitation of SPP is non-isotropic. Consequently, coupling such anisotropic fields with optically anisotropic materials may exhibit direction-dependent behavior. Thus, measuring SPR in various directions relative to the plane of incidence for anisotropic materials could result in different resonance angles.

Materials with optical anisotropy can occur in bulk or single layers of organic molecules with inherent shape anisotropy. Rod-shaped calamitic liquid crystal molecules, for instance, exhibit a birefringence of ∼0.2 in the bulk nematic phase [155, 156]. The liquid crystal molecules have great technological importance where such optical anisotropy play significant role in display device applications. When such shape-anisotropic molecules are aligned on a solid substrate through self-assembly or controlled Langmuir-Blodgett deposition [3], the deposited single layer induces optical anisotropy through a collective tilt of the molecules concerning the surface normal. Therefore, the projections of these tilted molecules yield a nematic ordering on the two-dimensional surface.

Here, we created an organic layer of specified thickness, with refractive indices made anisotropic by assigning distinct values along the X, Y, and Z axes. SPR spectra were obtained through simulation when the plane of incidence is parallel and perpendicular to the optic axis (OA) of the in-plane nematic ordering in the thin film of organic material. The difference in resonance angle was recorded as $\Delta\theta$ based on the SPR spectra obtained in these two geometries.

Fig:-5.3 shows the SPR curves obtained for an anisotropic thin film of 2 nm thickness having Δn as 0.1. The corresponding RAs were obtained as $44.45°$ and $44.80°$ yielding $\Delta\theta$ to be $0.35°$. In the simulation, the SPR curves are obtained for different values of Δn and thickness of organic film and the corresponding $\Delta\theta$ were obtained. A calibration surface displaying the variation of $\Delta\theta$ as a function of Δn and film thickness (t) is plotted in Fig:-5.4. The simulated data are fitted with a surface polynomial curve

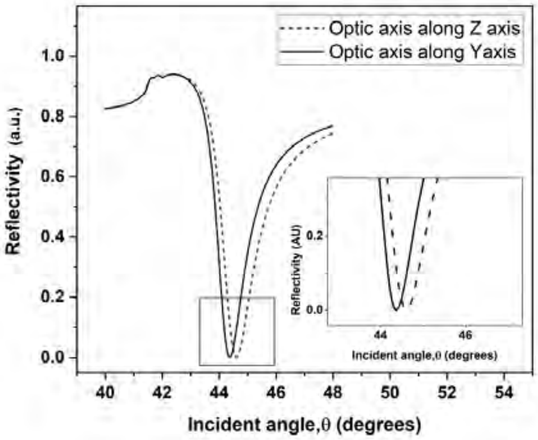

Figure 5.3: Simulated SPR spectra of a 2 nm thick organic film consisting of shape anisotropic organic molecules exhibiting an in-plane birefringence of 0.1.

$$\Delta\theta = P_1 + P_2 t + P_3 \Delta n + P_4 t^2 + P_5 \Delta n^2 + P_6 t \Delta n + P_7 t^2 \Delta n + P_8 t \Delta n^2 + P_9 \Delta n^3 \quad (5.1)$$

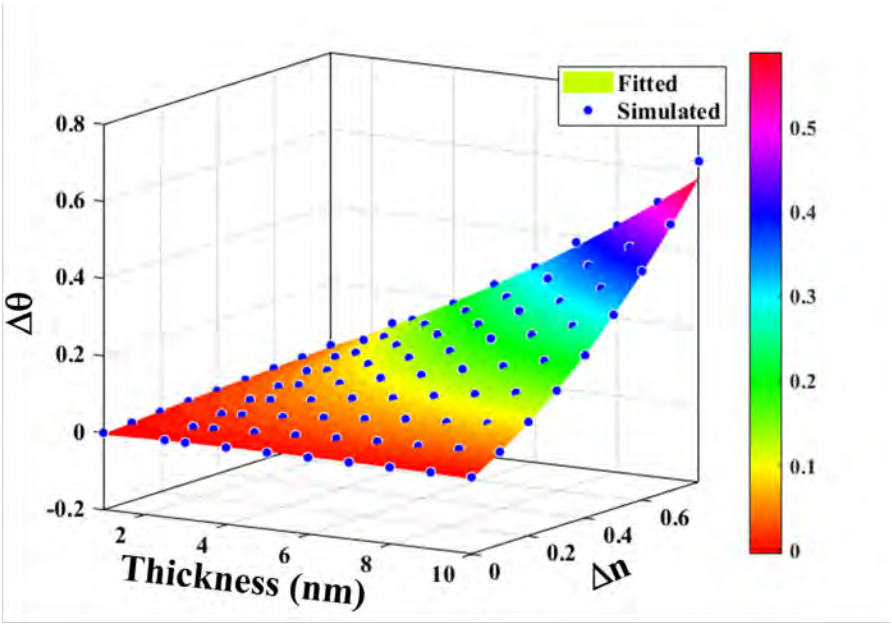

Figure 5.4: Calibration surface plot showing the variation of $\Delta\theta$ as a function of in-plane birefringence (Δn) and thickness of organic film. The simulated points are shown as filled circle. The surface is polynomially fitted.

where $P_i, i = 1, 2, 3...9$ are the fit parameters. The fit indicator R-square was 0.993 which suggests a good fitting. The fitted calibration surface as represented by the Eq:-5.1 can be useful for the determination of Δn of thin films using SPR phenomenon in the very simple prescribed methodology as discussed here.

Further, We have utilized the calibration surface (Eqn:-5.1) for the estimation of in-plane birefringence of ultrathin films fabricated using the standard LB technique. We fabricated a single layer of LB films of cadmium stearate (CdSA) and 8CB molecules on the SPR chips at the target surface pressure of 30 and 4 mN/m, respectively [73, 151]. The molecules in a single layer of LB films of CdSA and 8CB were tilted by $\sim$10 and 60° with respect to the substrate normal [150, 151]. Hence, they can offer anisotropy in the refractive indices and therefore can exhibit non-zero values of Δn. The thickness of the LB films were obtained from X-ray reflectivity measurement (Fig:-5.5). The experimental curve was fitted using Parrat's formulation [75] and the thickness of the film was estimated therefrom. The thickness of gold film deposited over the glass plate, LB films of CdSA and 8CB deposited over such gold substrates were estimated as 49, 2.4 and 2.0 nm, respectively.

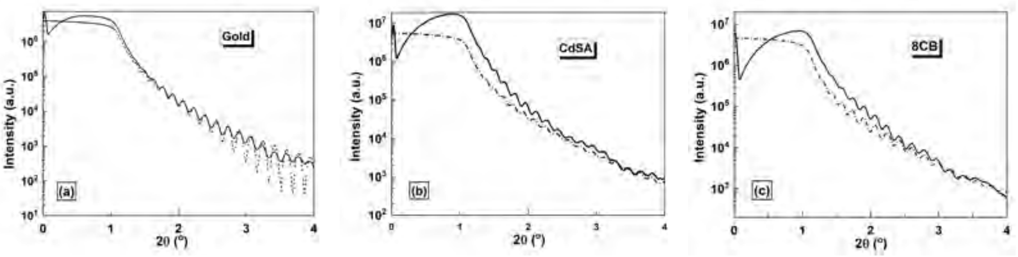

(a) (b) (c)

Figure 5.5: X-ray reflectivity curves obtained from (a) thin films of gold, (b) LB films of cadmium stearate (CdSA) and (c) 4'-octyl-4-biphenylcarbonitrile (8CB). The theoretical fitting yields the thickness of gold, CdSA and 8CB films to be 49, 2.4 and 2.0 nm, respectively.

The anisotropy in the RI can be measured experimentally by rotating the film in orthogonal directions and obtaining the SPR curves. For an isotropic film, the shift in resonance angles obtained by the SPR measurements in orthogonal direction (ΔR) is expected to be zero. However, due to the difference in the value of RI of the single layer of the film in orthogonal direction, (ΔR) will be non-zero. If the optic axis of the tilted molecules in the single layer lie in the plane of incidence, the measured RI from the SPR curve represent n_e and hence that measured by rotating the sample by 90° yields n_o. Since the field due to SPPs are anisotropic in the YZ-plane, the coupling with the anisotropic medium can yield non-zero value of ΔR.

The LB films of CdSA and 8CB were scanned using the SPR instrument. The change in RA along the such orthogonal directions ($\Delta\theta$) were found to be 24 and 71 millidegree, respectively. Such non-zero values suggest the anisotropy in the ultrathin films. The values of thickness and $\Delta\theta$ were substituted in the calibration surface and Δn of the ultrathin films of CdSA and 8CB were estimated as 0.012 and 0.022, respectively.

The analysis give a strong foundation for the measurement of in-plane birefringence of ultrathin films of organic molecules. Such information are essential for the development of optical devices. Thus we present a calibration surface showing the dependency of $\Delta\theta$ on Δn and thickness of the thin organic film. The calibration surface was obtained through simulation, and it was utilized for the estimation of Δn of single layer of LB films of cadmium stearate (CdSA) and 4′-octyl-4-biphenylcarbonitrile (8CB) molecules. The values of thickness and $\Delta\theta$ of the LB films of CdSA and 8CB were obtained from X-ray reflectivity and a home built SPR instrument, respectively, and these values were used in the calibration surface for the estimation of the respective Δn.

5.3 Role of sub-monolayer on SPR based sensing

A sub-monolayer refers to a ultrathin film that covers less than a full monolayer. The surface coverage is incomplete and consists of isolated islands of material rather than a continuous layer. During the deposition of ultrathin films on a solid substrate some defects are introduced. These defects arise due to several factors such as substrate roughness, deposition rate, adsorption kinetics and molecular interaction. Thus, a completer monolayer formation is restricted and small islands of nanoparticles are formed. The surface density of each islands of nanoparticles is different. Thus, this concept is crucial when employing ultrathin films as functional layers over metal layers in SPR applications. In SPR, the sensitivity and effectiveness of the sensor are significantly influenced by the thickness and uniformity of the functional layer. A sub-monolayer can enhance the interaction between the analyte and the sensor surface, providing more active sites for binding and thereby improving the detection capabilities. However, due to the presence of varied surface density on different position on the substrate, SPR response also varies. Thus, understanding the formation of sub-monolayer is vital for optimizing the performance of SPR-based sensors. In this thesis we have studied sub-monolayer using two model systems (a) silver nanoparticles and (b) single walled carbon nanotubes

5.3.1 Methodology

5.3.1.1 Experimental Methodology

The SPR measurements were performed on the same SPR instrument(OPtronix) as discussed in the previous section. The silver nanoparicles to be employed in the study were synthesized in lab. A solution of 0.5mg/mL silver nanoparticles in absolute ethanol (Sigma Aldrich, USA) was made. The gold chips were immersed in nanoparticle solution for varied time duration. The self assembled silver nanoparticles on the gold chips were then scanned using the field emission scanning electron microscopy(FESEM). Further, area coverage of the silver nanoparticles on the chip for different time duration was calculated using ImageJ software[157]. SPR response for each of the samples were recorded and further analysed.

5.3.1.2 Simulation Methodology

A finite difference time domain (FDTD) method was employed for the simulation of SPR phenomenon in the Kretschmann configuration using Ansys Lumerical as discussed in the previous section [149, 158]. Further,the silver nanoparticles (radius(r)= 10 nm) were uniformly seeded on the gold surface and the overlapping was allowed to closely resemble the ultrathin film of silver nanoparticles on the gold surface. The random seeding was performed using the scripting module in Ansys Lumerical package. The area coverage was varied by varying the number of silver nanoparticles distributed on the surface.

5.3.2 Results and discussion

In the FDTD mode, a p-polarized electromagnetic wave was allowed to incident at the glass–gold interface of Kretschmann configured SPR system in angular interrogation mode as shown in Fig:-5.6. The evanescent wave generated in the gold film can excite the surface plasmon polaritons (SPP). The minimum reflected intensity for the gold-air interface at incidence angle of 43.91°, which is in accordance with the literature[154, 158]. The surface coverage of the silver nanoparticles on the gold surface was varied by increasing the number of silver nanoparticles. The spherical silver nanoparticles of radius 10 nm were distribute randomly on the gold surface and the surface coverage(S_o) was estimated as

$$Surface\ Coverage(S_o) = \frac{A_o}{A} \tag{5.2}$$

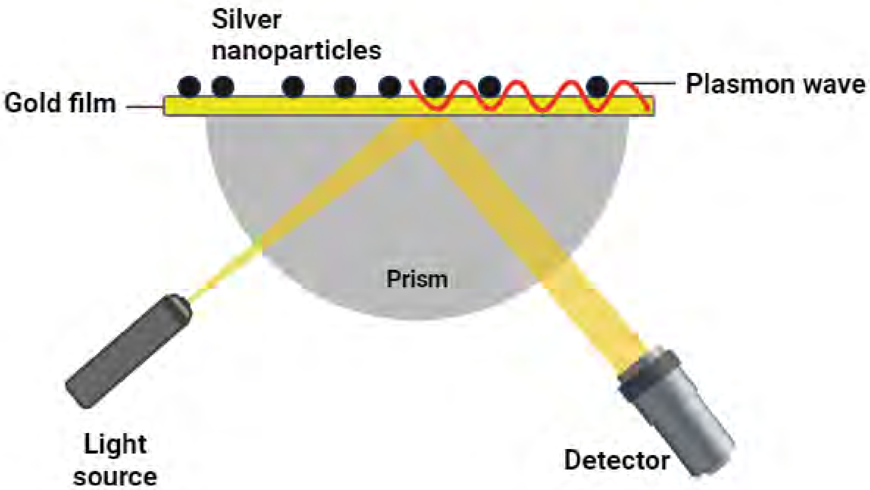

Figure 5.6: Schematic of SPR setup

here, $A_o = N \times 4\pi \times (r)^2$, N is the number of particles and A is area of the substrate. The distribution ultimately gave the surface coverage starting from 2% to 97%. The S_o value = 1, can be considered as a monolayer. However, S_o<1 is considered to be sub-monolayer. For each surface coverage, SPR spectra was observed and plotted as shown in Fig:-5.7. It was observed that an initial increase in surface coverage led to a red shift in the RA, which is in accordance to conventional SPR property. In conventional observations, any material irrespective of its property when deposited over the gold substrate it alters the resonance criterion and dampens the absorbance at the resonance. At low surface coverage the plasmonic field generated at the gold/air interface is altered due to the silver nanoparticles in accordance to the classical effective theory model[159]. At low surface coverage, the silver nanoparticles are far apart from each other, the local electromagnetic field at silver nanoparticles do not interact which each other[159], therefore we observe the conventional red shift in RA and absorbance dampening. This behavior is similar to a dielectric film when measured using SPR. The red shift continues till the surface coverage reaches 40%. Interestingly for S_o > 40%, a blue shift in the RA was observed. For S_o > 40%, the localized electromagnetic plasmonic field of the silver nanoparticles starts to overlap with each other resulting in exchange coupling. With increasing strength in coupling the kinetic energy of the plasmon decreases. This, in turn, starts to overcome the energy required for site charging, leading to a reduction in the Coulomb gap[160]. As separation continues to decrease, the Coulomb gap eventually closes, and the system undergoes a Mott-Hubbard metal-insulator transition[161, 162]. Consequently, with a significant reduction in the separation and a stronger interparticle coupling, the sub-monolayer of silver nanoparticles with $S_o > 40\%$ starts to exhibit properties resembling of a continuous metallic film. This observation suggests that at lower surface coverage of silver nanoparticles, the sub-monolayer manifests dielectric properties, while at surface coverages surpassing approximately 40%, metallic attributes become predominant. The redshift and blueshift observed in the SPR spectrum of silver nanoparticles provide insights into the collective behavior of the nanoparticles and the nature of their interactions.

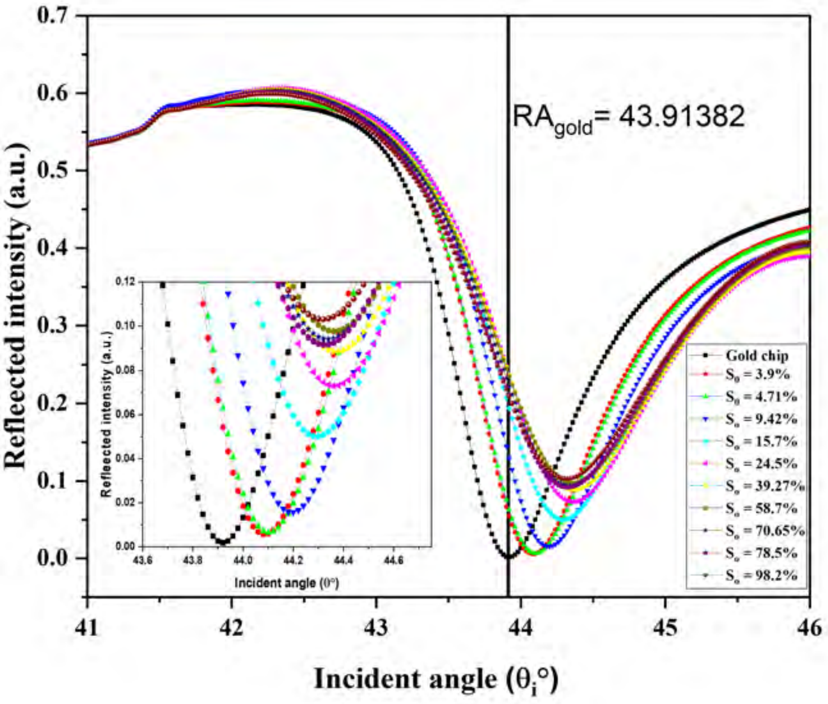

Figure 5.7: SPR response curves for different surface coverage of silver nanoparticles obtained from FDTD simulations.

In order to experimentally investigate the simulated observations, we used a simple thin film deposition technique via self assembly. The morphology and surface coverage of the self assembled layer of silver nanoparticles on gold layer of the SPR chip were analyzed using FESEM. The observed morphology for various surface coverage is shown in Fig:-5.8.

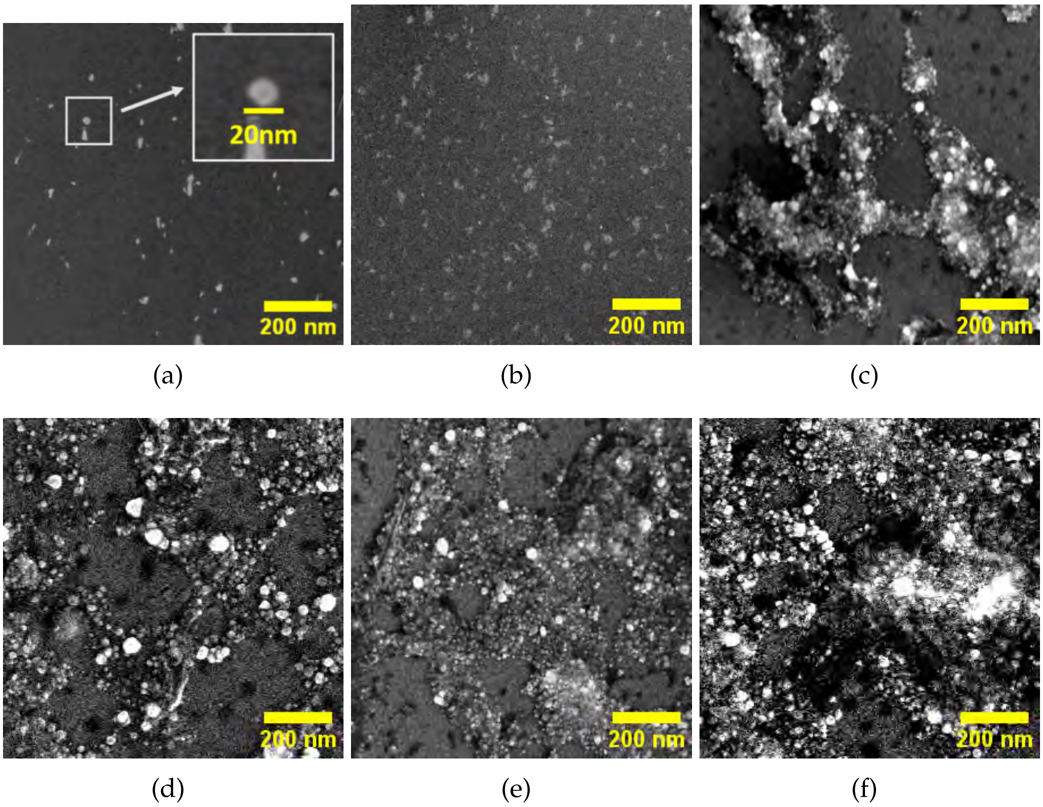

(a) (b) (c)

(d) (e) (f)

Figure 5.8: FESEM observation of silver nanoparticles at different time stamps during self-assembly film formation. (a) S_o = 4.75%, t = 4 hrs, (b) S_o = 14.5%, t = 8 hrs, (c) S_o = 42%, t = 12 hrs, (d) S_o = 55%, t = 16 hrs, (e) S_o = 75%, t = 20 hrs, (f) S_o = 97%, t = 24 hrs. Here time stamp t represents time allowed for self assembly.

During the deposition of sub-monolayer of silver nanoparticles, the surface coverage was controlled by allowing self assembly to happen at a specified time. It is expected to have higher coverage with larger time of self assembly. The time of deposition via self assembly is as shown in the Fig:-5.8. It can be clearly seen from the figure that the surface coverage increase with increase in time of deposition. As the gold chip was dipped into the solution of silver nanoparticles, the seeding happens randomly at different location of the gold chip. Usually when the silver nanoparticle adsorbs to the surface it diffuses on the surface and gets anchored at the defect site forming a seed. Once the seeds are formed, it grows with time on further adsorption of the silver nanoparticles. Such controlled growth of silver domains can lead to formation of sub-monolayer. If sufficient time of growth was allowed, a full monolayer can be obtained.

The SPR spectra of the sub-monolayer of silver nanoparticle were recorded for different S_o and are shown in Fig:-5.9. It is noteworthy that shift in RA follows the same trend as observed through simulation.

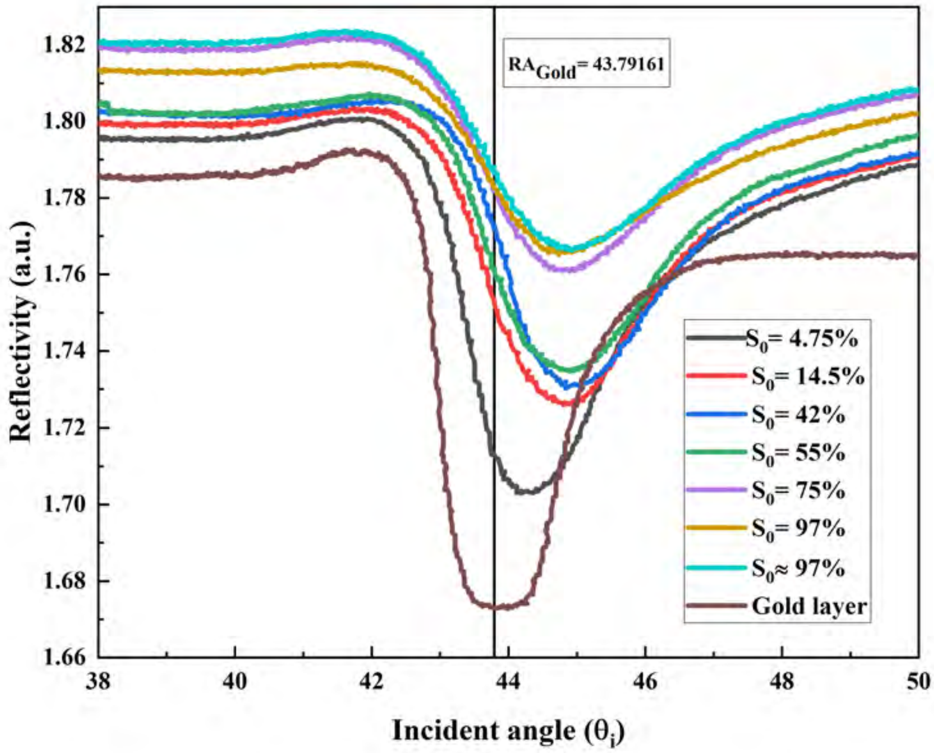

Figure 5.9: Experimental SPR response recorded for different surface coverage of the nanoparticles.

The experimentally observed spectra for different S_o values indicated red shift in RA for $S_o \leq 40\%$ and blue shift for higher S_o values. A comparison of RA obtained from simulation and experiment as function of S_o is shown in Fig:-5.10.

The trend of the variation in both the cases is found to be similar. the magnitude of RA appears to be different. This might be due to some uncontrollable

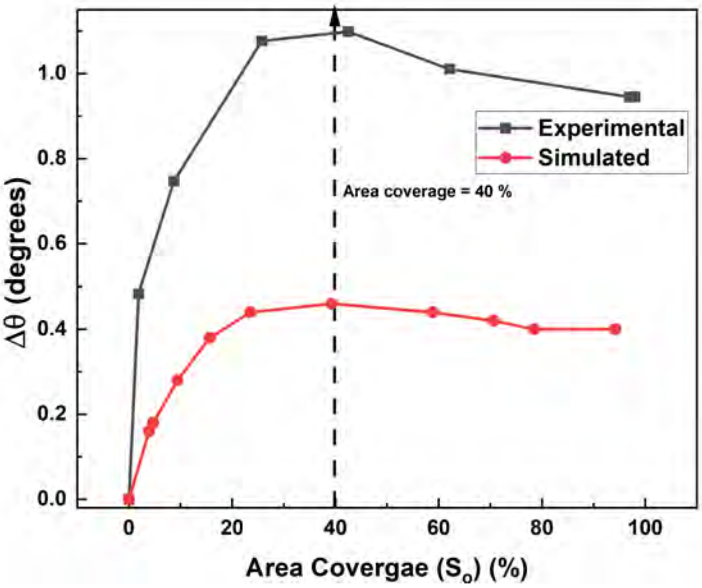

Figure 5.10: Simulated and experimental observation of RA for different surface area coverage of the nanoparticle.

variation in experimental and simulation setup. In simulation, the seeds have been spread uniformly on the gold chip. Such uniform seeds were allowed to grow uniformly in the simulation setup. However, in the experimental setup, it is difficult to control the uniform distribution of seeds as the seeding is primarily dependent on the presence of defect sites on the gold chip. It is also possible that the growth of the seed may not be uniform in the experimental setup. Nevertheless, the trend in variation of RA as function of S_o is essential as it signifies Mott-Hubbard metal-insulator transition.

Here, we observed that even though the bulk nature of silver is highly metallic, in sub-monolayer regime it behaves as an insulator/dilectric which can definitely affect the SPR response when employed for any application. The metallic behaviour is regained as the surface coverage exceeds 40% of the substrate area as it undergoes Mott-Hubbard metal insulator transition. Here, the silver nanoparticles are isotropic in nature therefore it will be interesting to observe the behavior of anisotropic film with varied surface density and alignment. Therefore, we will now discuss how the surface density and the alignment of single walled CNT (highly anisotropic) dictates the SPR response when deposited over the gold chip.

5.4 Role of surface coverage/intertubular distance and alignment of CNT on SPR response.

Over the recent years, aligned CNT have been employed in various applications[163–165]. Notably, CNT have emerged as key functional material in optical-based biosensing, such as SPR device[166, 167]. CNT, due to their excellent biocompatibility, it has been employed extensively for biosensing using SPR platform. CNT possess numerous advantageous properties, including nonlinear optical characteristics and saturable absorption. These attributes make them valuable materials for enhancing sensitivity in advanced target materials, contributing to increased specificity in sensor applications. CNT can be used as functional material to immobilize diverse biological components such as antibodies, DNA, antigens, and enzymes, providing a substantial surface area for such immobilization processes[168]. In an article by Lee et.al[167], they observed enhancement in SPR signal and four fold increase in sensitivity of human erythropoietin (EPO) and human granulocyte macrophage colony-stimulating factor (GM–CSF). Thus, CNT can be employed to enahance SPR signal and sensitivity.

CNT, known for their remarkable sensing characteristics, also exhibit significant inherent anisotropy[169] which is often overlooked while sensing based measurements. SPR is a highly sensitive measurement dependent on even a minute change in the refractive index in local environment. Anisotropic films have variation in the refractive index measured in orthogonal directions with respect to a given direction of the film (Δn). Thus the ultrathin film of CNT fabricated using LB deposition technique can have aligned nanotubes. The functional layers comprising of aligned nanotubes can yield different SPR responses dependent on the direction of the alignment with respect to the plane of polarization of the incident electromagnetic wave. Thus, it is important to study the effect of the anisotropic nature of CNT on the SPR response to have a better fundamental understanding before employing it for sensing based applications. Further, the surface density of CNT fabricated over the gold chip in SPR based sensing can also affect its response as the refractive index of deposited CNT is density dependent[170, 171]. Garcial-Vidal et.al[171] in their article stated that low-density of vertically aligned carbon nanotube arrays can be engineered to have an extremely low index of refraction. Yang et al.[170] observed that as the surface density of the vertically aligned CNT decreases the refractive index also decreases exponentially.

Therefore, in this section we have studied the SPR response on the surface density and anisotropy of the CNT film. Here, we have employed FDTD based simulation to study the SPR repsponse for different intertube separation for surface density based studies. The film anisotropy was controlled by aligning the CNT parallel and perpendicular to the direction of incident polarized light. The SPR measurement were recorded for both perpendicular and parallel alignements with varied intertube separation in order to study the effect on the SPR signal.

5.4.1 Simulation Methodology

The SPR phenomenon in Krescthmann configuration was simulated using FDTD method by employing a commercially available software package ANSYS LUMERICAL. The simulation schematic is shown in Fig:-5.11. The simulatiaon was carried out in a similar manner to the previous section. The generation of the surface plasmons in case of nanorods strongly depend on the aspect ratio, thus it is chosen wisely for minimising the radiation damping and scatterring. In this thesis we have employed CNT with 6nm diamter and 1μm in length for the SPR study. The aligned CNT with varied separation between each of the tubes were added over the gold layer and the change in the SPR condition was observed for both parallel and perpendicular orientation as shown in Fig:-5.11.

5.4.2 Results and discussion

The reference measurements on the gold-air interface was performed and the RA was observed same as 44°. The SPR spectra were obtained for the two orthogonal directions: when the long axis of the tube is (a) parallel and (b) per-

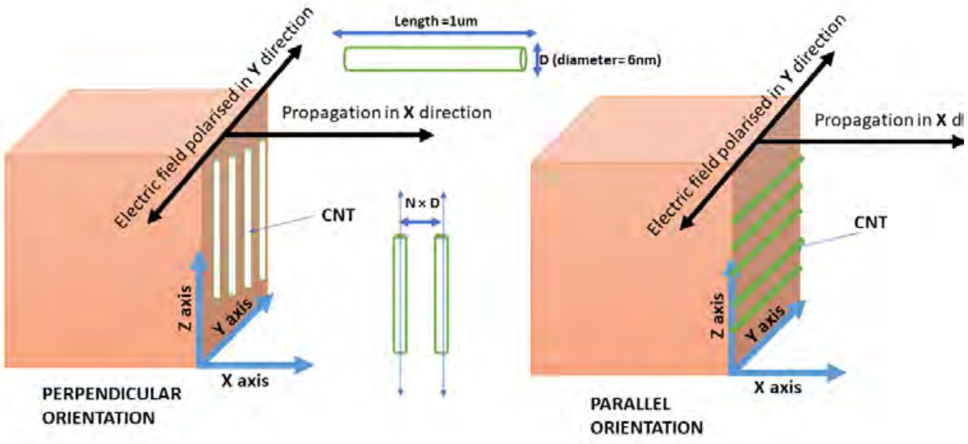

Figure 5.11: The parallel and perpendicular allignment of CNT considered for the proposed SPR measurement. Separation between the tubes is shown as N × diameter (D)

.

pendicular to the plane of polarization of the incident electromagnetic wave (Fig:-5.11). The SPR spectra for perpendicular and parallel alignment of the tubes with intertube separation equal to 4× D is shown in Fig:-5.12. Here, D is the diameter of the nanotube. In Fig:-5.12 the RA obtained from SPR spectra of CNT in parallel orientation was $44.152°$ and perpendicular orientation was at $44.337°$. The deviation in RA with respect to the gold reference for both the alignments with varied intertube separation are shown in Fig:-5.13(a). Such deviation is denoted as $\Delta\theta$. Further, the difference in the RA of parallel and perpendicular alignment for a particular intertube separation is denoted as $\Delta\phi$ which is shown in Fig:-5.13(b). $\Delta\phi$ can also be related to the birefringence which arrives due to the structural anisotropy in the ultrathin film[158]. The variation of $\Delta\phi$ with respect to intertube separation was fitted with a second order exponential decay function

$$\Delta\theta = A_o \exp(-r/t_1) + A_1 \exp(-r/t_2) + y_o \tag{5.3}$$

where A_o, t_1, A_1, t_2, and y_o are constants, and r is the separation between the CNT. The fit had R^2 value of 0.99 which suggests good fitting. In Fig:-5.13 (b),

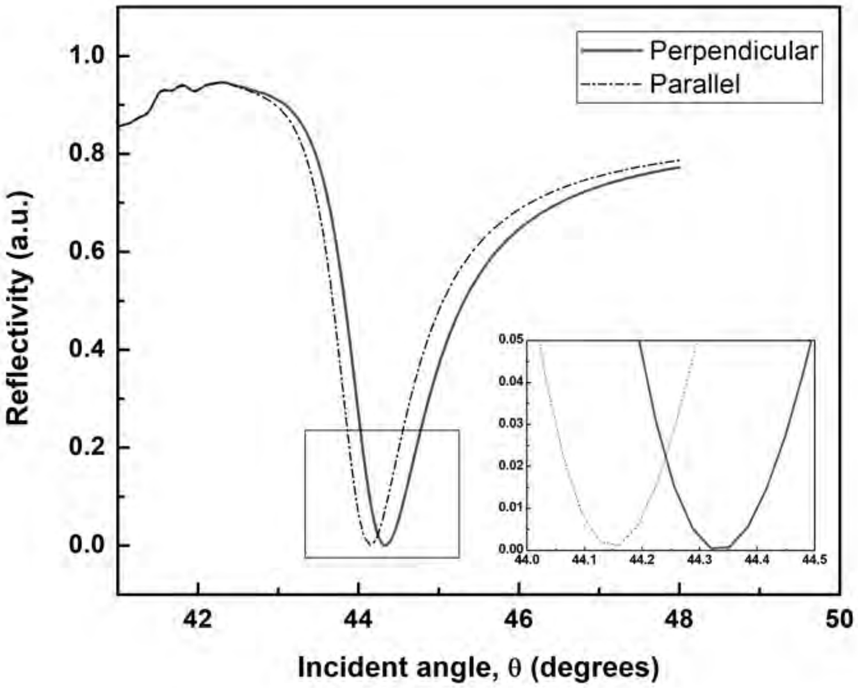

Figure 5.12: SPR spectra for parallel and perpendicular alignment of CNT. Separation between the tubes is shown as N × Diameter (D). Here, the spectra is shown for 4×D =24 nm. D is the diameter of the nanotube.

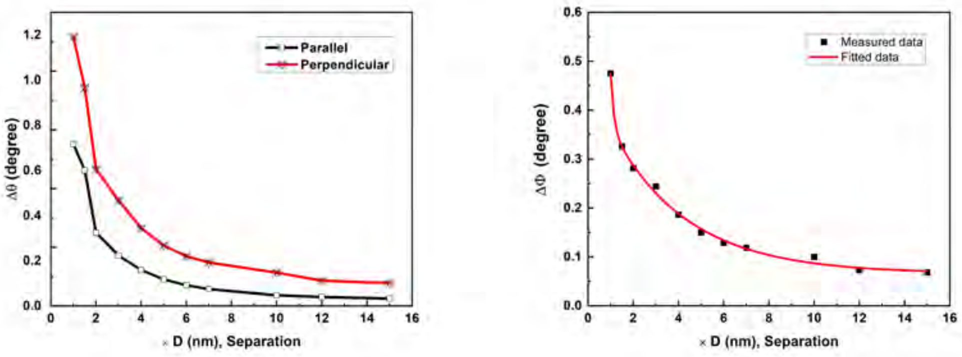

(a)

(b)

Figure 5.13: (a) Change in the RA denoted as $\Delta\theta$ for parallel and perpendicular alignment with respect to RA of gold layer for different intertube separation. (b) Difference in the RA of parallel and perpendicular alignment denoted as $\Delta\phi$ with respect to intertube separation.

the fitting shows that, the birefringence value decreases with increase in the intertube separation. The reduction in birefringence with increased intertube separation is primarily due to the weakening of the collective electromagnetic field interactions. At low intertube separation, the optical properties of the ultrathin film are significantly influenced by the interactions between the individual CNT. As separation increases, the ultrathin film has less pronounced anisotropic effects due to weakening of collective interactions. For separation greater than 8D i.e 96 nm the contribution of collective interaction saturates therefore, we observed saturation in birefringence value.

Fig:-5.14 shows the surface field distribution on the Y-Z plane for both the alignments. Here, Y-Z plane refers to the surface of the gold chip where CNT are aligned.

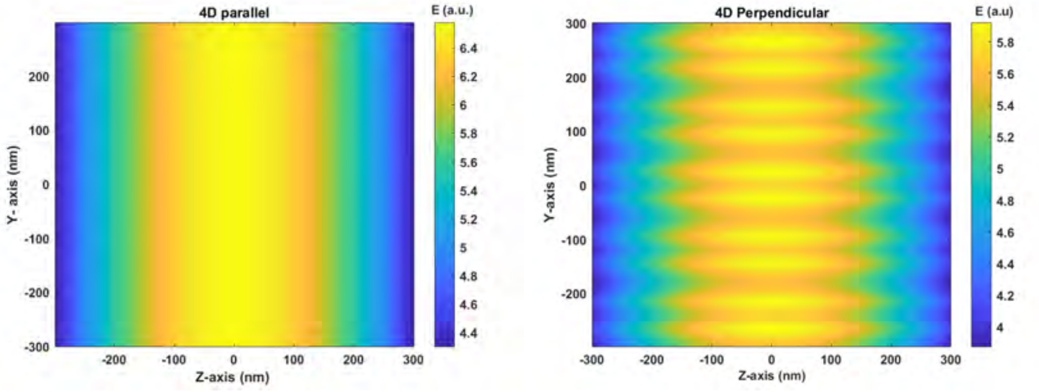

(a) (b)

Figure 5.14: Surface field distribution for (a) parallel and (b)perpendicular orientation of CNT for 4D separtion. Parallel and perpendicular orientation refer to the alignment of tube axis parallel and perpendicular to the plane of polarization of the incident electromagnetic wave.

From Fig:-5.14 (a), it can be observed that in parallel orientation of the CNT ,the plasmonic field distribution shows anisotropic behaviour. The field behavior is similar to plasmonic field distribution for a gold layer. Thus,it can be stated that for CNT layer when aligned parallel to the direction of polarization behaves as a metallic layer. Whereas, when CNT aligned in perpendicular orientation, the field distribution has some stratified structure. Therefore, CNT when aligned in perpendicular orientation it behaves as a dielectric or semiconductor. Similar observation was made by Devanarayanan et al.[147]. The stratified field response in is due to localization of plasmonic field in the perpendicular orientation.

Further, we observed that there was an enhancement in the electric field intensity in both cases at resonance condition. Thus, it will be interesting to observe the localized field response for different intertube separation. Therefore, a 3-dimensional discrete fourier transform monitor was placed in the cavity between the nanotubes. The incident angle of the p-polarized wave was kept at the RA and electric field profile was observed. The 3D monitors gives electric field profile along X, Y and Z direction. The cavity size is fixed in X and Z direction and only varies along Y direction with increase in intertube separation. Thus, the localized electric field magnitude along Y axis is extracted for different cavity size. The field enhancement factor was also calculated as per the relation:

$$Enhancement\ Factor\ =\ [\frac{E_{loc}}{E_{inc}}]^4 \tag{5.4}$$

where, E_{loc} is the average magnitude of electric field observed inside the cavity and E_{inc} is the magnitude of incident electric field. The E_{loc} for Y and Z direction were equal thus only Y-direction was considered and the dependence of enhancement factor on the intertube distance was plotted as shown in Fig:-5.15.

From Fig:-5.15, it was observed that, in parallel orientation the average field enhancement is comparatively 1.2 times higher than perpendicular orientation. As CNT in parallel orientation behaves as an metallic film, the field enhancement is comparatively higher in this orientation when compared to perpendicular orientation. In both alignments it was observed that at smaller cavity size i.e < 5 nm , the field enhancement factor suddenly increased. As in parallel orientation CNT has a predominant metallic behaviour, field enhancement is also more than the perpendicular orientation. The sudden increase in E.F. is due to localization of surface charges as the cavity size enters the quantum regime(<5 nm). When the cavity size enters the quantum regime, the classical Maxwell's equation fails to correctly describe the SPR response. In this sub-nanometre regime, the non-local screening quantum effect takes place and surface charges of the CNT gets redistributed. Therefore, the actual distance between the tubes is now considered to be the separation between

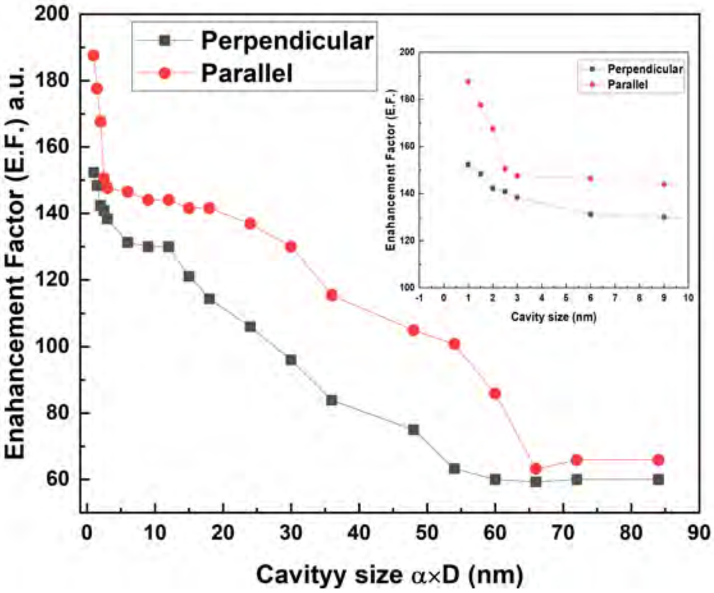

Figure 5.15: Enhancement factor with respect to cavity size. Cavity size is defined as $\alpha\times$D where α can be fraction/integer value. D is the diameter of CNT.

the surface charge rather than the actual geometrical gap. Thus, due to the no local screening we get huge enhancement in the field. Further, as the separation goes down even low (< 1 nm), where the surface of the CNT tend to touch each other, tunneling induced conductance starts to dominate and we observed a further increase in E.F. For the cavity size (10 nm< 65 nm), E.F decays due to decrease in the collective interactions between the nanotubes and later saturates as cavity size is increase >65 nm. The saturation in the E.F. is due to the negligible interaction of plasmonic field of CNT at large separation.

Therefore, in order to employ CNT for SPR applications it is necessary to understand CNT behavior at different surface density and orientation with respect to the incident electromagnetic wave. However, the control over surface density of CNT experimentally is still a area of research, our study provides a framework in understanding its behaviour for a wide range.

5.5 Conclusion

In this chapter we studied SPR resposne of different types of ultrathin films which are generally employed as a functional layer in SPR based applications. The organic ultrathin films such as Liquid crystals posses birefringence when arranged in 2D system and has an huge impact on SPR response when the value of birefringence or the thickness of layer is varied. We propose a calibration curve for change in resonance angle with respect to thickness and birefringence for efficient understanding of SPR behavior of such molecules prior to their application via SPR. Metallic nanoparticle such as silver nanoparticles have the optical property dependence on the surface density in the ultrathin regime. With increase in surface density they undergo mott-hubbard insulator metal transition and we observed that 40% surface coverage is the point of inflection. We examined both simulation and experimental studies, and observed that the surface coverage for the transition was identical in both. Furthermore, the SPR response is influenced by the surface density of CNT, which exhibit either semiconducting or metallic properties depending on their alignment with the incident direction of the electromagnetic wave's polarization. The parallel alignment of CNT has enhanced plasmonic field generation compared to the perpendicular alignment. The SPR response for varied surface density or intertube separation for both alignments were observed. CNT in parallel alignment showed anisotropic behavior whereas the plasmonic field for perpendicular arrangement showed stratified field response at resonance condition. The field distribution inside the cavity formed between the nanotubes were also studied. For different cavity lengths, field enhancement was calculated. The parallel alignment overall showed higher enhancement and we observed that as the cavity length was increased field enhancement dipped and lately saturates. The functionization of gold layer with such type of active layer enhance the performance but their inherent properties alter the SPR response. In the next chapter we have proposed a new configuration fro SPR chip where graphene is used as plasmonic as well as bio-recognition element that can eliminate such type of discrepancy due to functionlization.

CHAPTER 6

Monolayer, bilayer and twisted-bilayer graphene layers for label-free sensing using surface plasmon resonance.

In the preceding chapter, we studied the role of sub-monolayer and anisotropy in ultrathin film on the SPR response.Such practical limitations affect the reliable measurements using the SPR phenomenon. At resonance, the plasmonic field decays exponentially in the sensing medium. Thus, the functionalization of gold chip by immobilizing bio-ligands can reduce the efficiency of the sensor tremendously. Binding of the analytes with thicker bio-ligands may fail to alter the SPR conditions which may affect the sensitivity of the sensor. It is therefore recommended to have ultrathin layer as functional layer for any sensing application using SPR. In this chapter we have proposed a novel SPR design. In the proposed design we have employed graphene as dual nature active layer. Graphene being established as a good bio affinitive layer can also generate plasmon in terahertz regime. Thus, in our design we propose graphene to be employed as plasmon generative as well as the biorecognitive layer. The design offered a sensitivity of 20,000nm/RIU. Further, different graphene systems were also tested for the proposed design.

6.1 Surface plasmon resonance

SPR is a widely recognized optical phenomenon with significant applications in the fields of bio-sensing and bioanalysis. Its main advantage lies in its ability such as label free detection, high sensitivity and resolution[172, 173]. SPR is primarily employed as a method for measuring change in the refractive index (RI), which allows the detection of even minute quantities of analytes binding to the active area of the sensor [174]. The SPR based sensors can be improvised from several enhancement factors such as, optimization of optical components and appropriate functionalization of the active region. The most widely used SPR configuration in the sensing application is the Kretschmann configuration, which involves prism/metal/dielectric interfaces to create SPR conditions as shown in Fig:-6.1. This configuration is both highly sensitive and practically feasible. In this configuration, surface plasmon polaritons (SPP) are generated by the evanescent wave of the incident electromagnetic (EM) wave at the metal/dielectric interface. The resonance condition, characterized by the minimum intensity of the reflected wave, results in the maximum transfer of energy from the incident EM wave to the SPP wave. At this resonance, the plasmonic field becomes highly intense. This intense plasmonic field interacts with the dielectric medium above the metal surface. Any alteration in the dielectric properties due to the adsorption of analytes, perturbs the plasmonic field, leading to a shift in the resonance condition. This shift can be quantified using SPR instrumentation. This fundamental principle is used in all biosensing applications utilizing the SPR phenomenon.

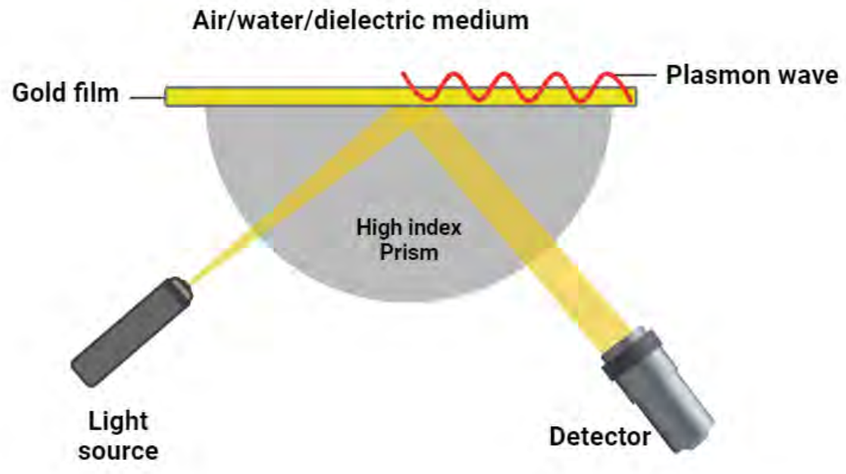

Figure 6.1: Schematic of conventional Kreschtmann configuration SPR setup.

In conventional SPR-based sensor, gold is predominately used as a plasmonic material for the generation of the SPP wave. It possesses several practical advantages like chemically inert, easy functionalization,and good stability in aqueous medium. However, the pure gold surface has a lower affinity for many bio-analytes. Therefore, to enhance the performance, several developments in conventional SPR have been reported. The use of a bimetallic (Ag-Au) layer, nanohybrid metal/dielectric structure Au with thin oxide film coating and amorphous carbon on surface plasmon active silver substrate have proved to enhance the sensitivity and sensitivity of the system. However, these hybrid and bimetallic layer do not have high bio-affinity towards small biomolecules and also sometimes, the thickness of such layers may not be able to induce any perturbation in the plasmonic field due to the adsorption of analytes. This reduces the sensing performance of the SPR-based biosensors. Therefore, the choice of functional layer should be appropriate such that SPP waves are able to interact with the introduced analyte and also acts as a good bioaffinitive layer. Thus, to increase the analyte affinity, the gold surface is to be functionalized with a suitable layer. Recently, it has been studied that graphene may be employed as a biomolecular recognition element (BRE) to functionalize the metal film for higher sensitivity. Graphene has a high surface-to-volume ratio and a rich π electron conjugation. It enhances the binding affinity of bio-analytes through $\pi - \pi$ interaction. The carbon-based ring structures in organic and biomolecules might enable efficient π stacking interaction with hexagonal graphene. Thus, the employment of graphene as the functionalized layers have proved to be appropriate for SPR sensing applications. biosensors[175–177].

Although, graphene can enhance the adsorption capability of the analytes, the FOM for graphene functionalized gold SPR chip in aqueous medium reduces[178]. Furthermore, the weak physical force of binding between metal and graphene can decrease sensitivity and stability[66, 179].

To address these challenges, the possibility of generating plasmonic fields within the graphene layer itself and effectively using graphene as a plasmonic material and a BRE to induce SPP waves and enhanced biomolecular interaction.

However, to observe plasmon generation in graphene, the investigation of optical properties of ultrathin graphene films is integral. But conducting experimental observations presents huge challenges. Graphene's exceptional transparency in the visible and near-infrared spectrum, complicates precise measurement of its optical characteristics due to minimal light absorption.

Graphene films employed for SPR are often single or few layered and present difficulties in interacting with sufficient photons for reliable detection. Substrate interactions introduce complexities as graphene, typically grown or transferred onto a substrate, can alter its intrinsic optical properties. In order to have a uniform layer sample preparation demands control to mitigate variations or impurities that could impact observed optical properties. Furthermore, some optical techniques have constrained wavelength ranges, limiting their effectiveness in probing the full spectrum of graphene's remarkable optical properties. Therefore, in this work we have employed DFT to calculate the optical properties of graphene. DFT offers huge advantage over other methods as it is computationally efficient. Calculations can be performed with reasonable accuracy, making it feasible to study the optical properties of ultrathin graphene layers within reasonable timeframes.

Graphene is single atom thick two dimensional system with remarkable optical properties[180–182]. It's extraordinary optical property lies in its unique band structure. It has linear energy dispersion and zero band gap [183]. Although, graphene has a very stable structure due to sp^2 hybridization between the carbon atoms. The number of layers, stacking sequence, stacking orientation and energy dispersion affect the band structure of such low dimensional systems [184]. Multilayer and stacked graphene has also attracted tremendous interest in the optical field of sensor research and development [185–189]. The simplest form of multilayer and stacked graphene structure consists of two layers termed as bilayer graphene(BLG) [190]. Subsequently, due to the interlayer interactions, the linear bands of the monolayer transforms into pair of parabolic bands and band asymmetry is introduced between the valence and conduction band for BLG structures. The most investigated forms of stacking present in BLG structures are AA, AB and twisted stacking. In AA stacking, the lateral coordinates of the carbon atoms in each layer are identical whereas in AB stacking one of the layer is relatively shifted by the vector equal to the edge of the hexagon. This suggests that all the carbon atoms in each layer of AA BLG are stacked one above another whereas only half of the carbon atoms in each layer of AB BLG are stacked one above another. This indicates that the interlayer coupling of the graphene layers in the AA and AB BLGs is different which leads to different band structure and hence different electrical and optical properties. The level of interlayer coupling can be altered by giving a relative in-plane twist to one of the layer in BLG system which are known as twisted BLG. The band structure of these BLG systems are different. The band structure of AA appears like two copies of monolayer, AB as asymmetric and parabolic and a complex band structure for twisted BLG. The generation of Moire patterns in twisted BLG as a function of twist angle indicates different degree of coupling between the layers and hence suggests an immense possibility to alter the physical properties as a function twist angle in the twisted BLG system. This made the twisted BLG extremely interesting and instigated many research groups to thoroughly investigate the BLG systems.

In this chapter we explored the optical properties of monolayer graphene(MLG), bilayer graphene(BLG) in both AA and AB stacking and twisted bilayer graphene(T-BLG) with different relative in plane twists in AA and AB stacked BLG. The refractive index calculated from the DFT. Further using the DFT calculated refractive index of the graphene systems, we simulated the SPR for a given design using finite difference time domain (FDTD) method.

6.2 Simulation Methodology

6.2.1 Density Functional theory calculation

The RI of monolayer and BLG structures was calculated for a unit cell which belongs to P3/MMC/93 hexagonal crystal family [191]. For monolayer calulation, a 2-atom unit cell [192] and for a bilayer system, 4-atom unit cell was assumed. The interlayer distance between the two layers was kept as $0.342\ nm$. The study was carried out for both AA stacking and AB stacking. For the AA stacking of the second layer, the two atom system was put just above the first layer such that the lateral coordinates of the carbon atoms in each layer were identical. For AB stacking, the second layer was shifted towards y direction by one bond length of C atom in graphene i.e $0.142\ nm$ as shown in the Fig:-6.2.

An angular twist was applied to one of the graphene layer of the bilayer system. The RI for both small and large angular twists were calculated. The RI calculation was performed via DFT [77, 193, 194] with Generlized Gradi-

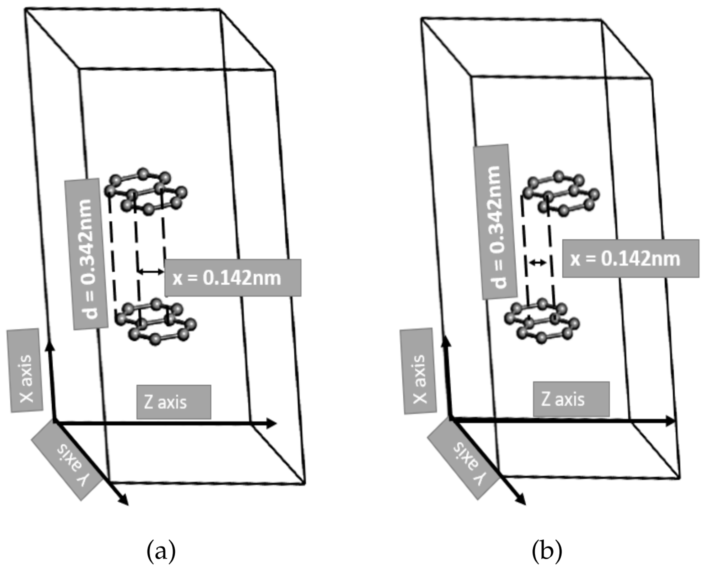

(a) (b)

Figure 6.2: Schematic diagram of the bilayer stacking adapted for simulation.(a) AA stacking (b) AB stacking. In the chosen geometry, the graphene plane is lying along Y-Z axis whereas the layer stacking is along X-axis.

ent Approximation (GGA) and applying Perdew Burke Ernzerhof (PBE) function [195] as exchange correlation function which further was implemented in Cambridge Serial Total Energy Package (CASTEP) [196]. Ultrasoft psuedopotential was employed to represent the ionic cores. The total energy minimization was done through convergence tests which includes lattice relaxation, energy change, maximum force and stress in the unit cell to obtain ground state energy. The optimization was performed for 101 iterations. The total energy per atom was allowed to converge upto $2 \times 10^{-7}\ eV$, the force per atom to $1 \times 10^{-6}\ eV$ and maximum displacement and stress were allowed to converge upto $10^{-4}\ nm$ and $0.05\ GPa$ respectively. The calculations were carried out in Brillouin zone with $4{\times}4{\times}1$ k point mesh of Monkhorstpack(MK) scheme [197]. The kinetic energy plane wave cut off was set to $700\ eV$ for single layer system and $1000\ eV$ for bilayer system. The calculation for RI was performed for energy range $0.03\ eV - 15\ eV$.

6.2.2 FDTD simulation for SPR in Kretschmann configuration using graphene systems

A finite difference time domain (FDTD) method was employed for the simulation of the SPR phenomenon using a commercial package of Lumerical. The FDTD simulation setup; the schematics of graphene system such as MLG, BLG, and T-BLG systems; and the graphene-SPR sensor setup are shown in Fig:-6.3, 6.4 and 6.5 respectively.

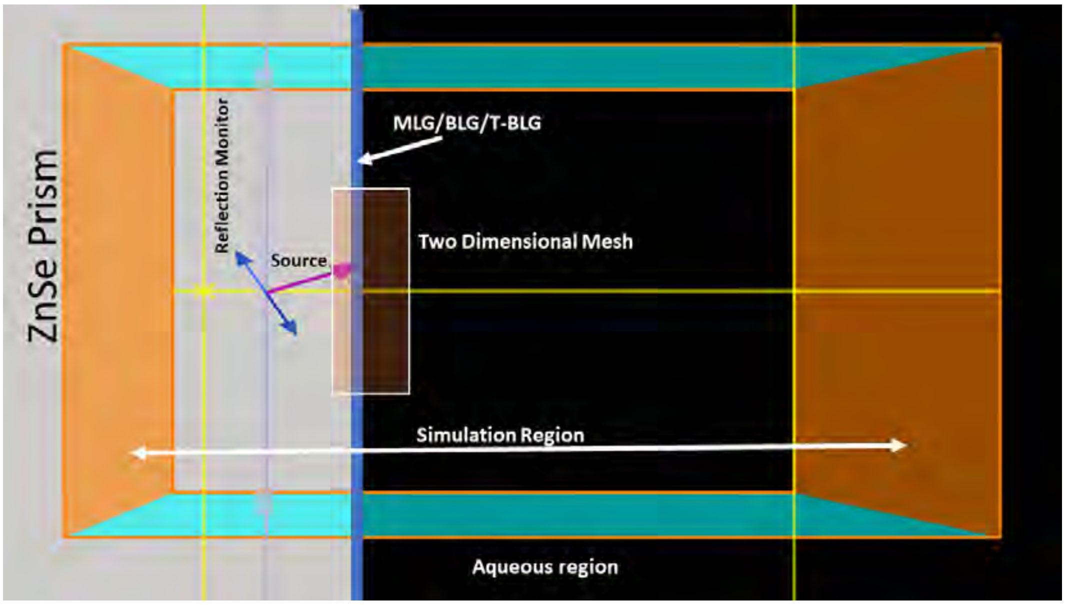

Figure 6.3: Schematic of conventional Kreschtmann configuration SPR setup used in FDTD simulation.

The simulation was carried out in an aqueous medium with a refractive index of 1.33 RIU and pH = 6. This is one of the physiological conditions where pH = 6 is suitable for biosensing. However, a change in pH does not have a direct impact on SPR measurement until it changes the RI of the aqueous medium. A plane wave source was allowed to an incident at the zinc selenide (ZnSe)–graphene system interface at an angle of 25° which is slightly more than the critical angle of incidence for total internal reflection in ZnSe. A few of the simulation parameters for the material used are mentioned in Table:-6.1

The thickness of ZnSe and aqueous medium is taken very large to represent a continuous medium. Although a smaller simulation region is considered to solve Maxwell's equation at the ZnSe/graphene interface, the per-

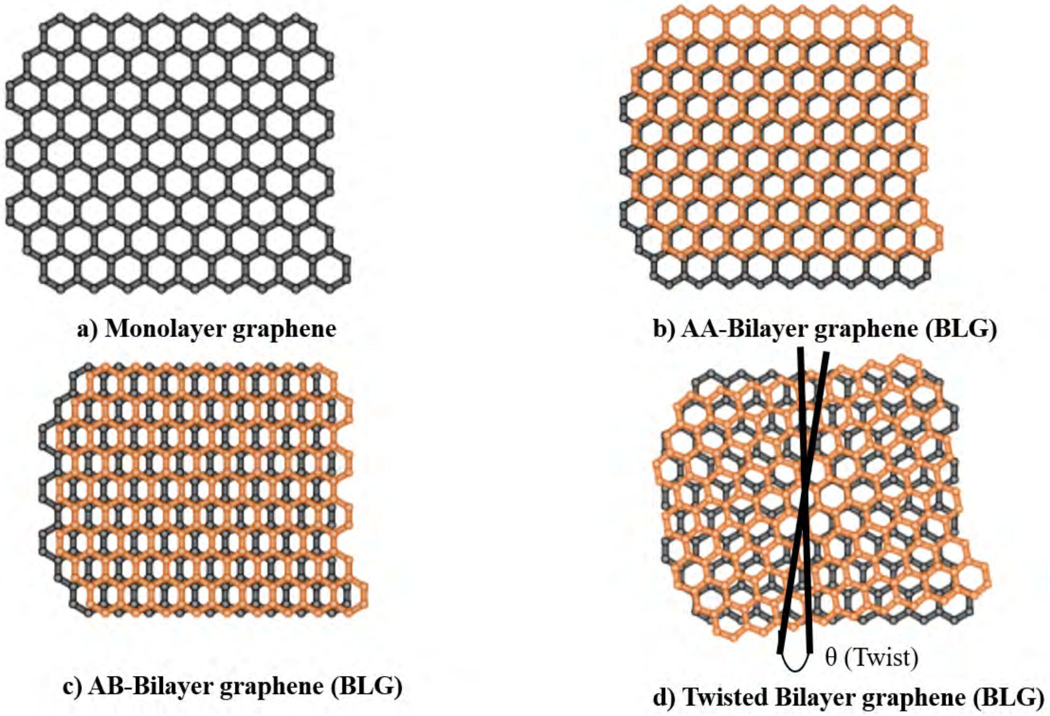

Figure 6.4: Graphene systems employed as plasmonic and bio recognition element. The schematic of (a) Monolayer graphene, (b)AA stacked (c) AB stacked and (d) twisted bilayer graphene is shown.

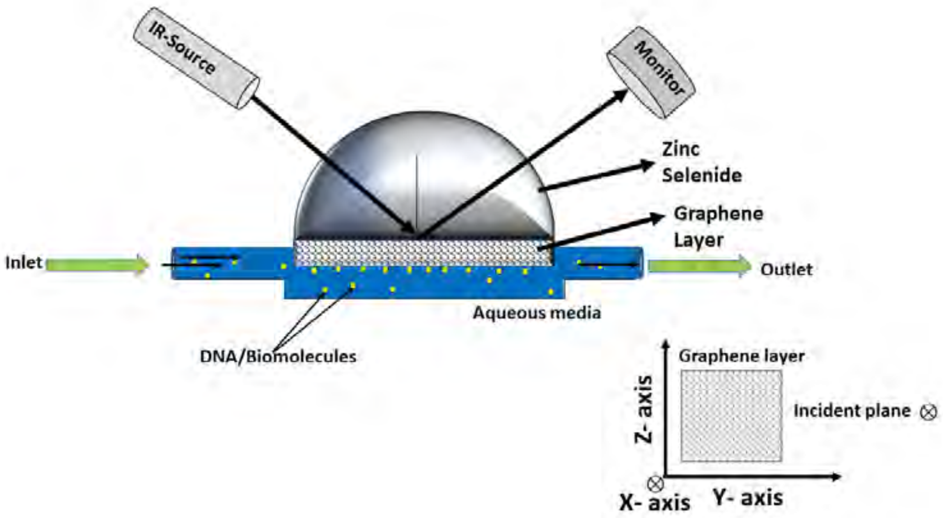

Figure 6.5: Schematic of graphene-SPR sensor setup.

Material	Thickness	Refractive Index
ZnSe	100 mm	2.46
MLG	0.34 nm	As per DFT calculation
BLG (AA/AB stacking)	0.68 nm	
T-BLG (for different twists)	0.68 nm	
Aqueous medium	100 mm	1.33

Table 6.1: The thickness and RI of the layers used in the simulation.

fectly matched layer (PML) boundary condition with a steep angle profile of 12 layers was used to minimize reflection from the boundary as the wave enters the layer. Linear discrete Fourier transform monitors were used to capture reflected and transmitted electric field at 350 nm away from the interface. These monitors return the Fourier transform of time domain electromagnetic fields. To obtain the resonance condition, a wavelength interrogation sweep was generated from 1–15 μm with 1000 iterations. Later after the observation of SPR wavelength at 13.7 μm in the MLG system, the sweep was reduced to 12–15 μm with 5000 iterations for better numerical accuracy. A mesh override was selected in the propagation direction of the plane wave to get a more precise result. To observe the two-dimensional plasmonic field generated at the graphene surface, a 2D monitor was placed, and the plasmonic field was captured at the resonance condition. For biomolecules/analytes sensing, the refractive index of the aqueous medium was varied from 1.33 to 1.331 in steps of 10^{-4} RIU. The RI range was chosen to represent biosensing applications in the aqueous medium. Most of the biosensors need an aqueous medium where the change in RI may lie in this range. The calibration curves showing the variation of the shift in resonance wavelength $\Delta\lambda$ as a function of change in RI of aqueous medium possessing the analytes (Δn) were obtained for MLG, BLG, and T-BLG (with different twist angles) systems. Mathematically, sensitivity (S_λ) can be calculated from the slope of the calibration curve using the formula

$$S_\lambda = \frac{\Delta\lambda_{RW}}{\Delta\, n} \tag{6.1}$$

Figure-of-merit (FOM can be calculated as follows:

$$FOM = \frac{S_\lambda}{FWHM} \times [\Delta T] \tag{6.2}$$

FWHM is the Full Width at Half Maximum, and $\Delta T = 1 - T_{\text{min}}$, where T_{min} is the dip in the reflectivity at the resonance wavelength (RW).

6.3 Results and Discussion

6.3.1 DFT calculation of optical properties

6.3.1.1 Monolayer graphene (MLG)

The DFT calculation were performed to obtain refractive index (RI) of the graphene system as a function of energy of the photon. Firstly for MLG, the spectra for both the real (n) and imaginary part (γ) of the complex RI ($r = n + i\gamma$) is shown in Fig:-6.6 over a wide incident energy range. The observed RI in our calculation was compared to available literature to check the validity of the simulated result. The obtained value of r at $1.96\ eV (i.e. 634\ nm)$ through our calculation was $2.24 + i0.48$. The values of r of the graphene monolayer varies marginally as reported by several other groups [198–201]. This variation may arise due to difference in simulation parameters viz. variations in the energy cutoff value, atomic potential modeling, different exchange correlation functions and MK pack scheme and k-mesh grid points. The absorption (γ) spectra for the monolayer graphene shows three major peaks at 2.62, 4.45 and 14 eV. These peaks might be attributed to the transition between the $\pi - \pi^*$ states for low energy and $\sigma - \sigma^*$ interband transitions for high energy peaks [202]. The corresponding variation in n is consistent with Lorentz's electron model of the origin of RI [203]. Consequently, the entire spectrum is divided into three regions as shown in the Fig:-6.6. The magnitude of γ peaks in these three energy ranges are quite high as compared to the normal dielectric materials. This suggests that the single layer of graphene behaves more like metals in these range of energy of the incident photons. The band structure of graphene monolayer suggests the Fermi level to lie near the Dirac point

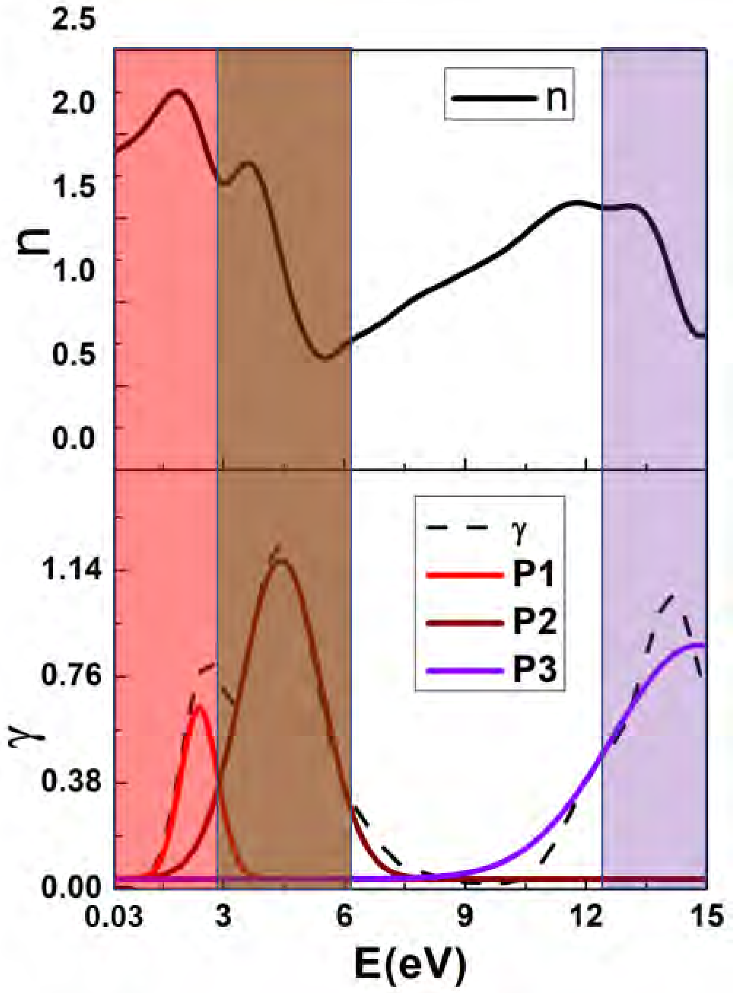

(a)

Figure 6.6: Spectra showing real (n) and imaginary (γ) part of the complex refractive index ($r = n + i\gamma$) of graphene monolayer. The component peaks P1, P2 and P3 were obtained by deconvolution method.

due to which conduction band is empty and valence band is filled completely. Thus, the free electron-hole pairs are mostly available and awaiting to be excited through an incident phonon of the corresponding energy which results in broad absorption spectra [204]. A similar broadening of n and γ can be seen in Fig:-6.6.

6.3.1.2 Bilayer graphene (BLG)

Bilayer graphene (BLG) can be considered as another class of materials which can be potentially employed for several novel applications. It shares many properties with its single layer counterpart, such as high electrical mobility, flexibility and chemical stability. But due to the structural difference between them, bilayer system has number of different electronic and optical properties. Among these, the most notable ones are comparatively larger band gap [205] and optical response in infrared region [206]. Bilayer graphene structure naturally tend to have AB type stacking (e.g. highly oriented pyrolytic graphite) although, using certain controlled deposition techniques such as CVD [207] and Langmuir-Blodgett (LB) technique [53], we can achieve different types of stacking. The two major bilayer graphene stacking are - AA and AB. The physical properties of BLG with different stacking are known to be different. Additionally, a relative planar twisting plays a crucial role in altering the optical and electrical properties of the BLG.

We calculated the RI of the BLG for both AA and AB stacking. The RI as a function of the photon energy for AA and AB stacking is shown in Fig:-6.7(a) and (b), respectively. The γ spectrum of AA stacking shows five prominent peaks at 3.43, 5.16, 9.52, 11.13 and 12.92 eV. The corresponding variation in n resembles the Lorentz's electron model of RI. As a result, it is possible to divide the spectrum in five ranges as shown in the Fig:-6.7. The γ spectrum of AB stacking (Fig:-6.7 (b)) shows interesting result. The two prominent peaks at 2.49 and 4.42 eV with almost three-fold increase in strength as compared to the highest peak in AA stacking have appeared. The three peaks in the range of 6 - 15 eV are relatively lower strength but have similar magnitude as compared to that in AA stacking. The five major peaks in AB stacking appear red-shifted as compared to that of AA stacked layers. The three-fold rise in magnitude of the absorption γ peak indicates increase in metallicity in AB stacking. In AA

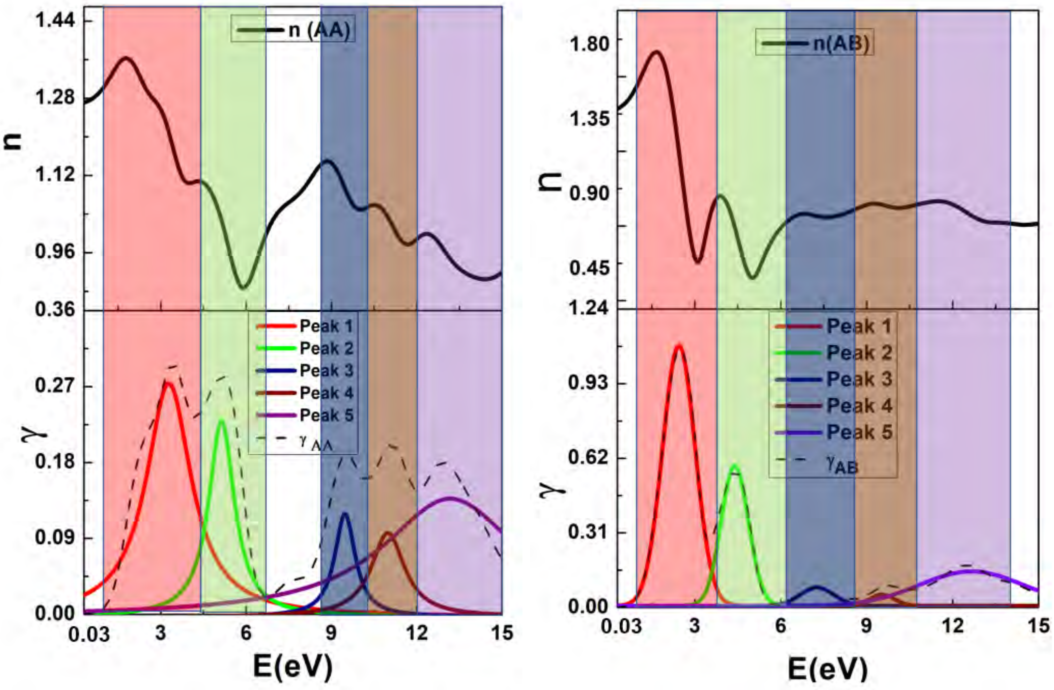

(a) (b)

Figure 6.7: The spectra showing (a) real and imaginary part for (a) AA stacked and (b) AB stacked BLG.The component peaks P1-P5 were obtained by deconvolution method.

stacking, the band structure looks like two copies of monolayer bands with a vertical offset of Dirac cones at the Brillouin zone boundary whereas in AB-stacked configuration, it has a pair of intersecting parabolic bands with additional parabolic bands away from these bands [208]. In AB stacking, it has only one conduction channel around Fermi energy whereas in AA stacking, it has two accessible conduction channels which can lead to a significant decay in reflectance. Therefore, some similarities in the spectra of monolayer graphene and AA stacked BLG can be observed in terms of position of low energy peaks and broadening of the spectra. A significant change in the spectra of AB stacking can be observed with respect to either AA stacking or monolayer graphene. The spectra of AB stacking shows intense peaks which are red-shifted as compared to that of AA stacking which indicate enhancement of metalicity of the AB stacked BLG in the low energy regime.

6.3.1.3 Twisted Bilayer graphene (T-BLG)

Recently, twisted bilayer graphene (T-BLG) is a major research focus due to it's extraordinary electrical and optical behaviour . Many research groups [72, 208–210] have studied these physical properties which arise from twisting a layer relative to other in bilayer system [71]. In a typical bilayer graphene system when two aligned graphene sheets are stacked, the energy band structure shifts from linear to parabolic due to the interlayer hopping of the electrons. Now, due to additional in-plane twist between layers, a hexagonal Moiré pattern consisting of alternating AA and AB-stacked regions emerge and acts as a superlattice modulation [211]. Due to the superlattice formation, the band structure folds itself into mini Brillouin zones. In these mini Brillouin zones, the Fermi velocity of electrons decrease as the adjacent Dirac cones undergo hybridization. Thus, forcing the band structures of T-BLG to become more complicated as compared to normal AA or AB stacking. The superlattice of T-BLG also reduces the linear dispersion range as well as the energy span between the conduction band and valence band. Therefore, the Dirac points shift in the visible or infrared regime depending on the angular twist. The shifts in the Dirac points influence the optical absorption peaks. In presence of such relative twist between the layers, the T-BLG will also be accompanied with various interlayer coupling strength, and thus going to exhibit different physical properties. Fig:-6.8 shows the contour plot for the real and imaginary part of RI for small $(0 - 10^{\circ})$ and large in-plane relative angular twists $(10 - 90^{\circ})$ for AA and Fig:-6.9 for AB stacking.

From the contour plots it is evident that the RI is dependent on not only the photon energy but also the in-plane relative angular twists in the BLG system. In BLG system, the optical conductivity is energy dependent. As the twist is applied, the energy span between the bands changes. The different orientation angle affects the electronic structures of T-BLG by reducing the band gap at a point and may introduce more bands or absorption peaks. Also, the van der Waals interaction between the layers plays an important role at a particular twist angle which gives rise to a sudden change in the RI for a given energy. Further analysis of the real and imaginary part for both the stacking at different twist angles, it implies that the same bilayer graphene material can exhibits

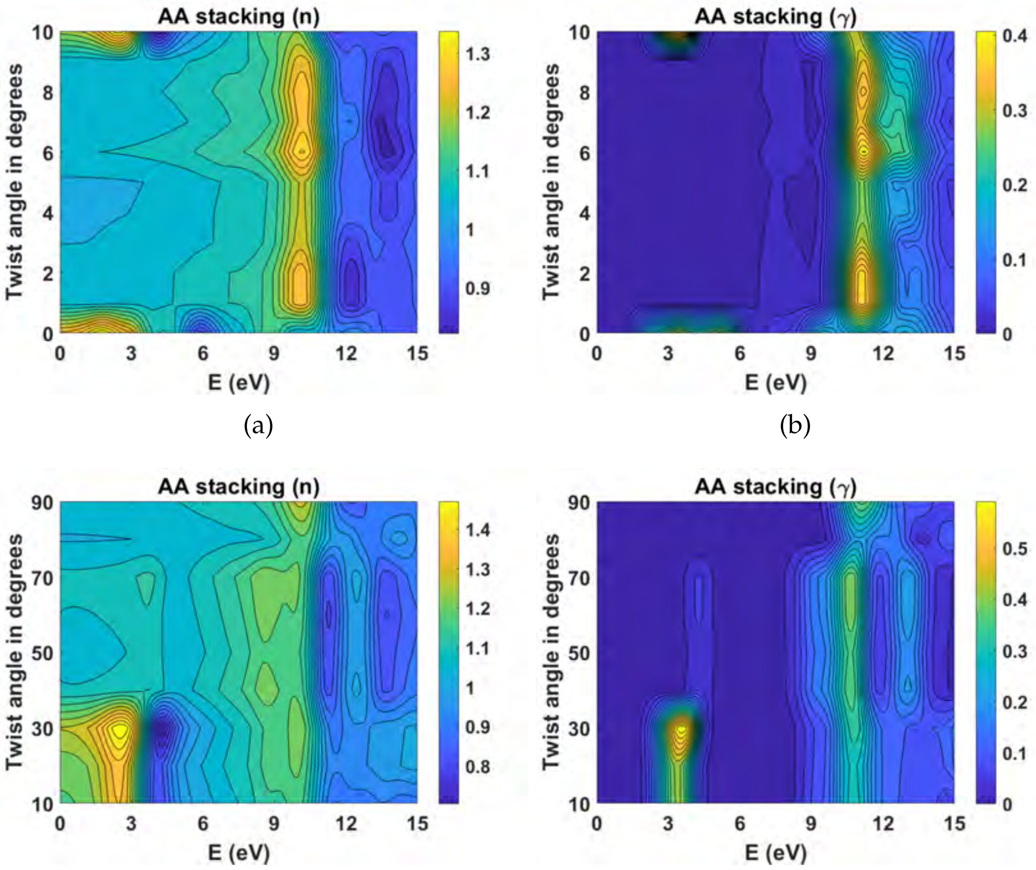

(a) (b)

(c) (d)

Figure 6.8: (a) Real part (b) imaginary part for small in-plane relative angular twists in AA stacking. (c)Real and (d) imgainary part for larger in-plane relative angular twist in AA stacked bilayer graphene

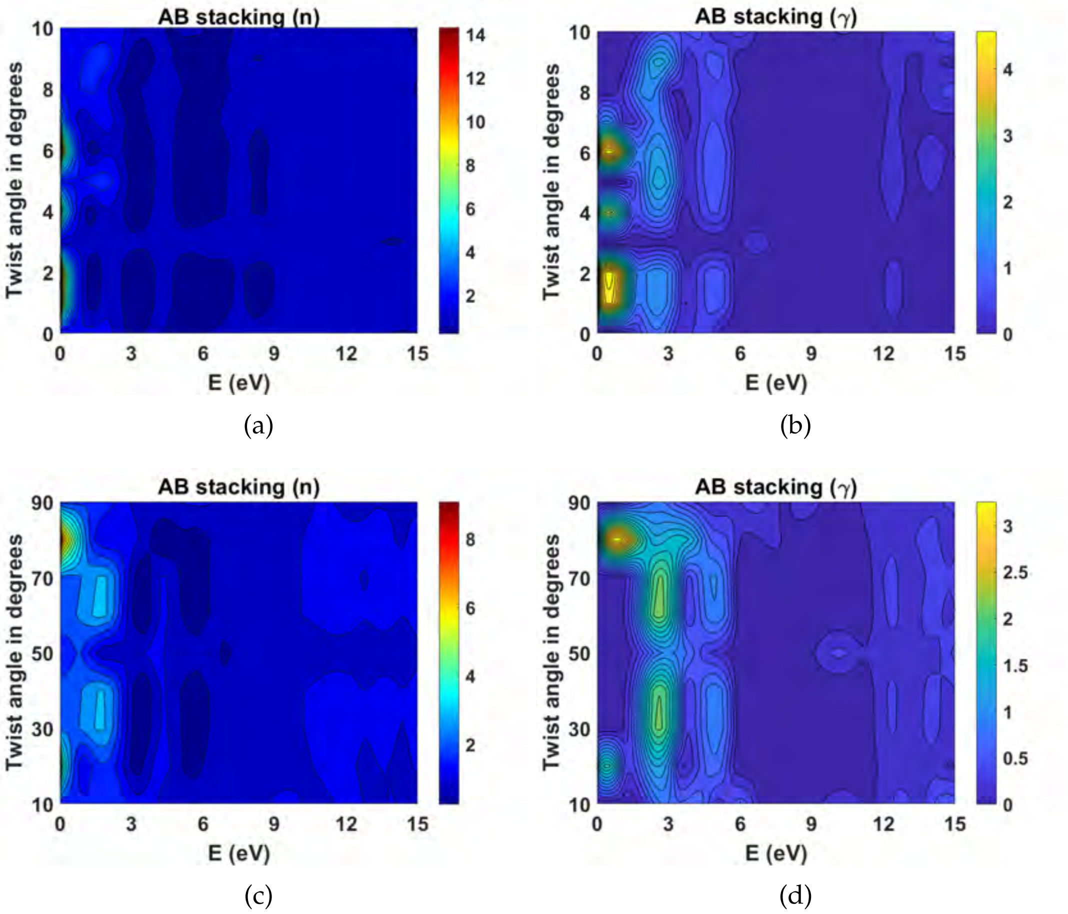

(a) (b)

(c) (d)

Figure 6.9: (a) Real part and (b) imaginary part for small angular in-plane relative twist in AB stacking (c)Real and (d) imgainary part for larger in-plane relative angular twist in AB stacked bilayer graphene)

metallic (M), semimetallic (SM), dielectric (D) and semiconducting (SC) behavior when operated in a particular energy range. In the Table:-6.2[212], there are few example of the materials which belong to specific type are listed with their RI range for different energy ranges.

Material	Infrared ($1.24\ eV - 1.7\ eV$)		Visible($1.7\ eV - 3.3\ eV$)		Ultraviolet($3.3\ eV - 124\ eV$)	
	Real	Imaginary	Real	Imaginary	Real	Imaginary
Ag(M)	$1 < n < 10$	$4.4 < \gamma < 40$	$0.15 < n < 0.19$	$1.5 < \gamma < 4.4$	$0.75 < n < 1.6$	$0.75 < \gamma < 1.6$
Au(M)	$0.25 < n < 5$	$3.8 < \gamma < 40$	$0.25 < n < 1.4$	$1.76 < \gamma < 3.8$	$n \approx 1.4$	$\gamma \approx 1.7$
Si (SC)	$3.48 < n < 3.7$	$10^{-13} < \gamma < 10^{-3}$	$3.48 < n < 6.6$	$10^{-3} < \gamma < 10^{-1}$	$1.6 < n < 6.6$	$10^{-1} < \gamma < 4.65$
Sn (SM)	$3.13 < n < 10$	$0.483 < \gamma < 4.6$	$0.85 < n < 3.13$	$2.73 < \gamma < 4.6$	$0.85 < n < 1$	$0.734< \gamma <2.73$
Quartz(D)	$1.15 < n < 1.45$	-	$1.45 < n < 1.47$	-	$1.47 < n < 1.55$	

Table 6.2: Table showing the refractive index (RI) for different materials which belong to different categories.

The calculated values of RI for T-BLG of AA and AB stacking of BLG systems was compared with some of the common materials exhibiting M, SM, D and SC properties. A phase diagram schematic was constructed as shown in Fig:-6.10. The phase diagram shows the dependencies of photon energy and the relative in-plane twist angle between the layers of BLG having AA and AB stacking to exhibit different material properties viz. M, SM, D and SC. It is quite clear from the schematic that smaller twist has greater impact on the optical properties of both the stacking. The AA stacking yields dielectric behavior in more than half the region of the phase diagram whereas the AB stacking exhibits large SC and SM behavior in small and large twist phase diagram, respectively. The optical properties of bilayer graphene are known to be dependent on the type of stacking viz. AA or AB due to difference in their band structure. However, the formation of Moiré pattern due to application of relative in-plane twist in the BLG indicated that the optical properties can be altered. The calculation of RI using DFT on such BLG systems shows very interesting result. The absorption spectrum of AA stacked layer resembles some similarity with that of monolayer graphene whereas the spectrum of AB stacked layer was found to be red-shifted. It reveals two sharp peaks in the low energy regime with almost three-fold increase in strength as compared to AA stacking. This indicates enhancement of metalicity in AB stacking as compared to that of AA stacking. The RI of BLG of AA and AB stacking were calculated as a function of in-plane relative twist between the layers. The AA stacking reveals largely dielectric behavior whereas the AB stacking shows predomi-

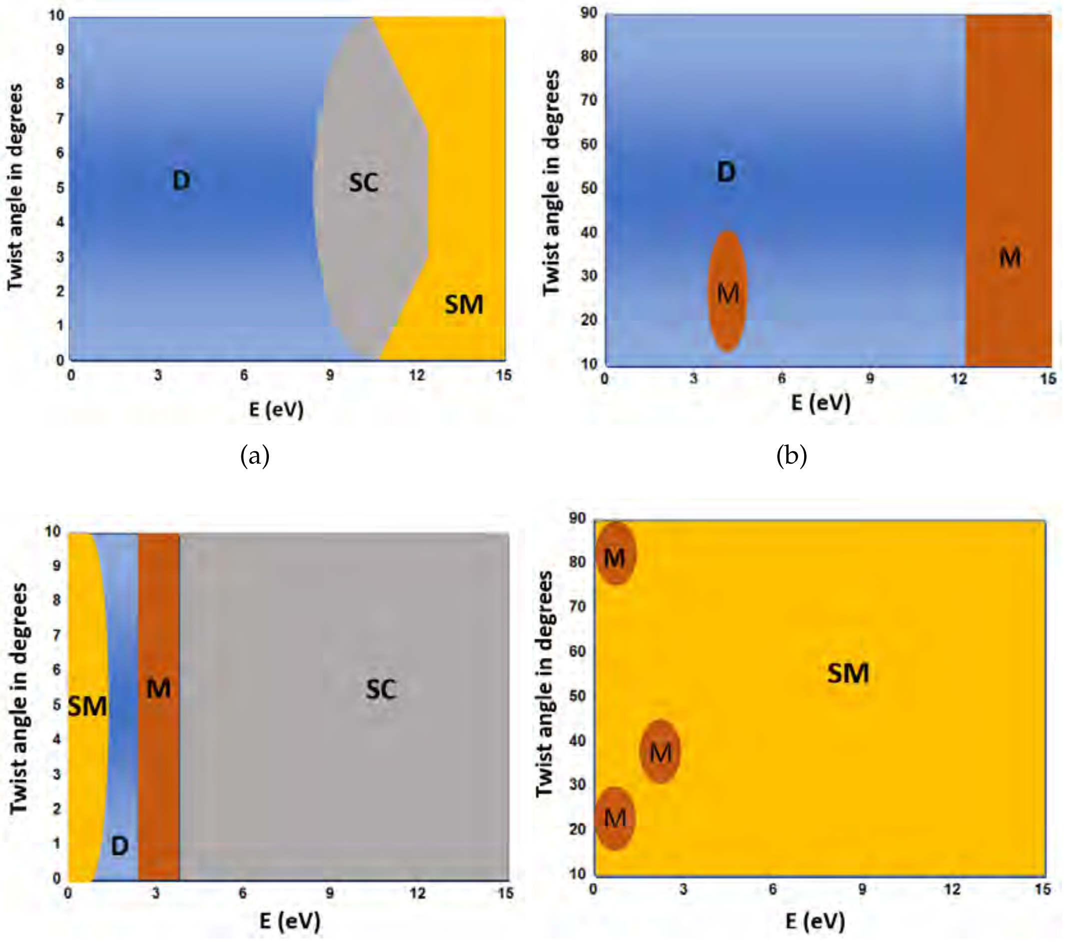

(a) (b)

(c) (d)

Figure 6.10: Schematic phase diagram showing different category of materials for (a) small angle and (b) large angle twists in AA stacking and similarly for AB stacking in (c) and (d), respectively.

nately SM and SC behavior as a function of the twist angle. The studies will be very useful for the development of optical devices e.g. sensors, optoelectronics and lasers. Further, using the observations from the DFT calculations an efficient SPR based sensors by optimization of twist angle of the BLG system is proposed.

6.3.2 Sensing measurements using the graphene system: FDTD calculation

6.3.2.1 Monolayer graphene

The FDTD method is highly reliable and advantageous over other techniques in solving Maxwell's equations for complex geometries of materials. It also has the benefit of calculating reflectance for multiple wavelengths of light per simulation. The main advantage of FDTD compared to the other methods such as Transfer Matrix Method (TMM) and other methods is that it can give the transmission properties over a wide spectral range with just a single calculation. It can also calculate time domain field profile and the currents over the entire computational domain. Moreover, it can treat defects with no additional computational complications. Here we have employed Kretschmann configuration with wavelength interrogation to investigate SPR phenomena in graphene. A p-polarized electromagnetic (EM) waves were allowed to incident at the ZnSe-MLG (Z/M) interface as shown in Fig:-6.5. For bio-sensing measurements, the dielectric medium is generally aqueous (RI = 1.33 RIU and pH = 6). Thus, SPR sensing module consisted of ZnSe/MLG/aqueous (Z/M/A) system. The SPR spectrum and the 2D plasmonic field distribution from the Z/M/A system in pure water medium is shown in Fig:-6.11 The spectrum Fig:-6.11 (a) shows a good trend with a resonance wavelength (RW) of about 13.7μm. The spectrum is similar to that of a glass/gold/aqueous system. The field distribution of 2D plasmonic field Fig:-6.11 (b) is also found to be similar to that of a glass/gold/dielectric (Fig:-5.2 (b)).

The concentration of the bio-analytes in the aqueous medium is changed by changing the RI of the aqueous medium from 1.33 to 1.331 in the step of 1×10-4 RIU. The corresponding SPR spectra were simulated and are shown in

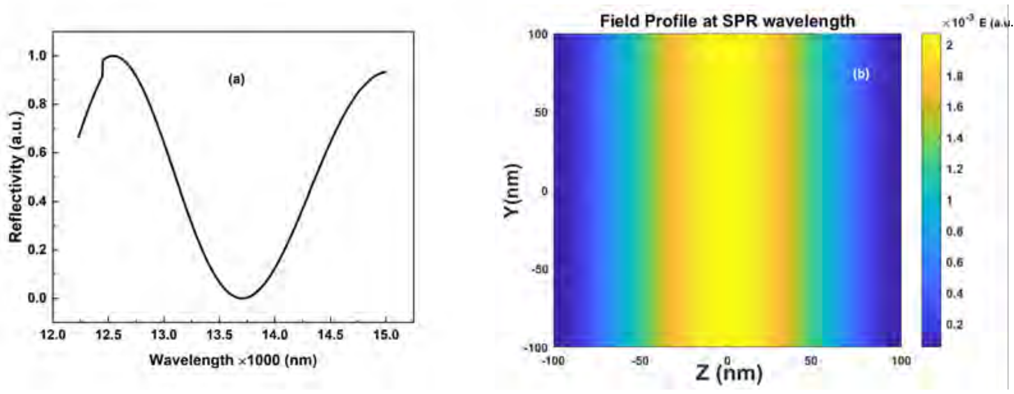

(a) (b)

Figure 6.11: (a) SPR spectrum from Z/M/A system. (b) The plasmonic field profile for the Z/M/A system obtained at resonance wavelength (on Y-Z plane).

Fig:-6.12-a. The resonance wavelength (RW) shifts towards higher wavelength as a function of concentration of the bio-analytes in the aqueous medium. A calibration curve is obtained by plotting the shift in RW ($\Delta\lambda$) due to change in RI (Δn) of the aqueous medium. A linear trend in the calibration curve was obtained which is one of the indicators of good sensor. The sensitivity of the device was calculated from the calibration curve, Fig-6.12-b and using the Eq:-6.1, and it was found to be approximately 20,000 nm/RIU. This is about four times the average sensitivity reported yet for graphene based SPR sensors in infrared regime. This enhancement is due to the choice of suitable coupling medium i.e. ZnSe in the present case. The ZnSe medium provides least attenuation of the incident EM wave in IR regime which otherwise gets absorbed largely in a glass coupling medium. Thus, the MLG system over the ZnSe coupling medium can be a good candidate for sensing application using the SPR phenomenon.

6.3.2.2 Bilayer graphene

The bilayer graphene (BLG) is considered as another category of materials which are being employed for various novel applications. Due to the structural difference between MLG and BLG, bilayer system has larger band gap and altered optical response in infrared region. The BLG structure naturally tends

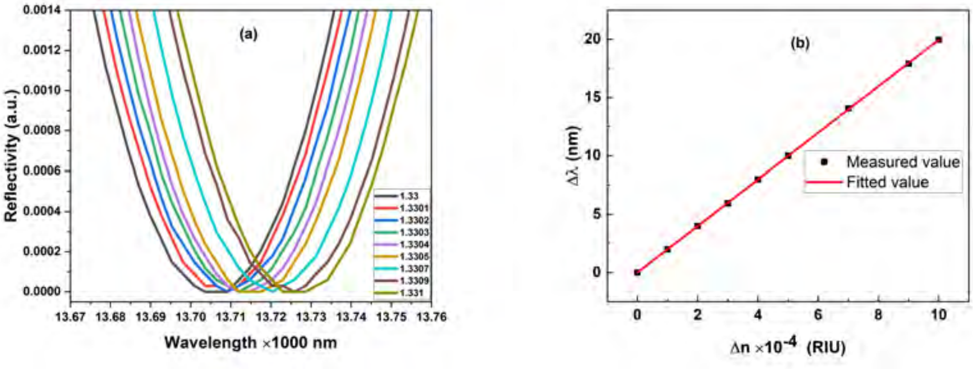

(a) (b)

Figure 6.12: (a)SPR spectra for different refractive indices of aqueous medium due to adding of biomolecules from Z/M/A system (b) Calibration curve showing change in resonance wavelength (Δλ) Vs change in RI (Δn).

to have Bernal (AB) type stacking (e.g. highly oriented pyrolytic graphite). Although, using certain controlled deposition techniques such as CVD , non-Bernal stacking (AA or twisted) can be achieved . The optical properties of BLG with different types of stacking are known to be different. It is noteworthy that the coupling between the two layers of a BLG system can be altered by applying a relative in-plane twisting. It is, therefore, interesting to study the effect of twisting on sensing performance of a BLG-based SPR sensor. On investigating, we found that the BLG system with AA and AB (non-twisted) stacking does not show any significant change in the RW, and sensitivity as compared to MLG system. The sensitivity of AA and AB stacked BLG are found to be 20,016 and 19300 nm/RIU which are closer to MLG system (20000 nm/RIU). Additionally, we found that twisting of AA stacked BLG does not show any further improvement in sensitivity and FOM. This was expected from our previous studies wherein the optical properties of AA stacked BLG does not reveal significant change as compared to the untwisted state. However, it was also observed that the optical properties of AB stacked BLG system was highly dependent on the in-plane twist angle as shown in the schematic phase diagram dependent for different relative in plane twist.(Fig:-6.10). Therefore, it is interesting to study the SPR based sensing of the AB stacked BLG system as a function of in-plane twisting.

6.3.2.3 Twisted Bilayer graphene

The T-BLG system is rather an unconventional and complex system. It possesses a complex band structure which varies for different in-plane twisting. Due to the twists, hexagonal Moire patterns are generated with irregular defects along the bilayer system which affects its band structure leading to a twist angle dependent behaviour. The AB type stacked BLG behaves like a semi-metallic in the mid infra-red region due to small angular twists (1°-10°) and as metal for larger twists like 20° and 80°. It was found that coupling between the layers for lower twist angles is high and it diminishes for the large twist angles. Therefore, we performed the simulation to observe the SPR curve from AB stacked BLG system in the aqueous medium for the twist angles (Z/T/A) in two different regions viz. low angular twist (1°, 2°, 3° and 7°, semi-metallic behaviour) and high angular twist (20° and 80°, metallic behaviour). Fig:-6.13 (a) shows the SPR curves for the T-BLG systems with different twist angles. It can be observed from the figure that the spectrum shifts towards left (blue shift) of the AB stacked BLG with 0° twist. The blue-shift of RW (-Δ λ) SPR spectra towards for the given aqueous medium suggests increase in metallicity of the T-BLG system due to twisting. The amount of blue shift in RW is calculated and shown in Fig:-6.13 (b).

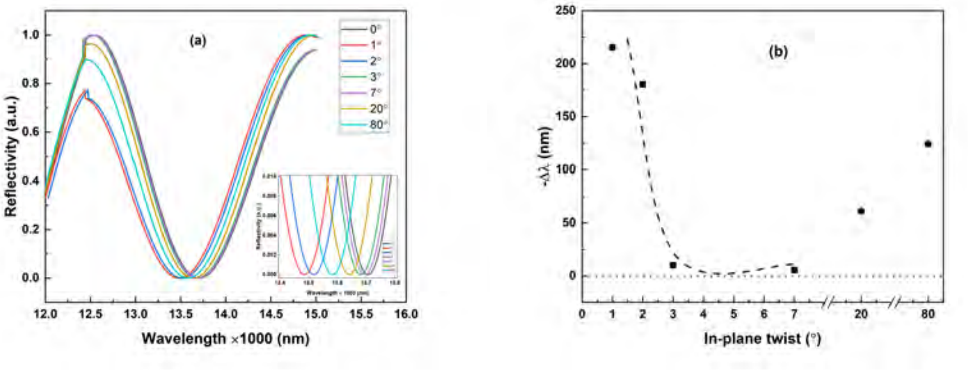

(a) (b)

Figure 6.13: SPR spectra and (b) corresponding RW (λ) for different in-plane twist angles in AB stacking of T-BLG (Z/T/A) system. (-) sign represents blue-shift in RW of the SPR spectra as observed in (a). The dash line is drawn to show the reference. Z/T/A corresponds to ZnSe/ Twisted-BLG/ Aqueous.

The amount of blue shift in RW is calculated and shown in Fig:-6.13-b. It can be observed that the, maximum blue-shift in RW (220nm) was obtained for a twist angle 1°. In the low angle regime, it decreases sharply till 3°and then saturates at 7°. The -$\Delta\lambda$ value increases moderately for large twist angle e.g., 20° and 80°. This variation thus suggested that the T-BLG system exhibited the largest metallic characteristics for the twist angle of 1°. The sensitivity towards bio-analytes in aqueous medium was calculated from the calibration curves obtained for the BLG and T-BLG as a function of twist angle. The results are summarized as a bar diagram in Fig:-6.14-a.

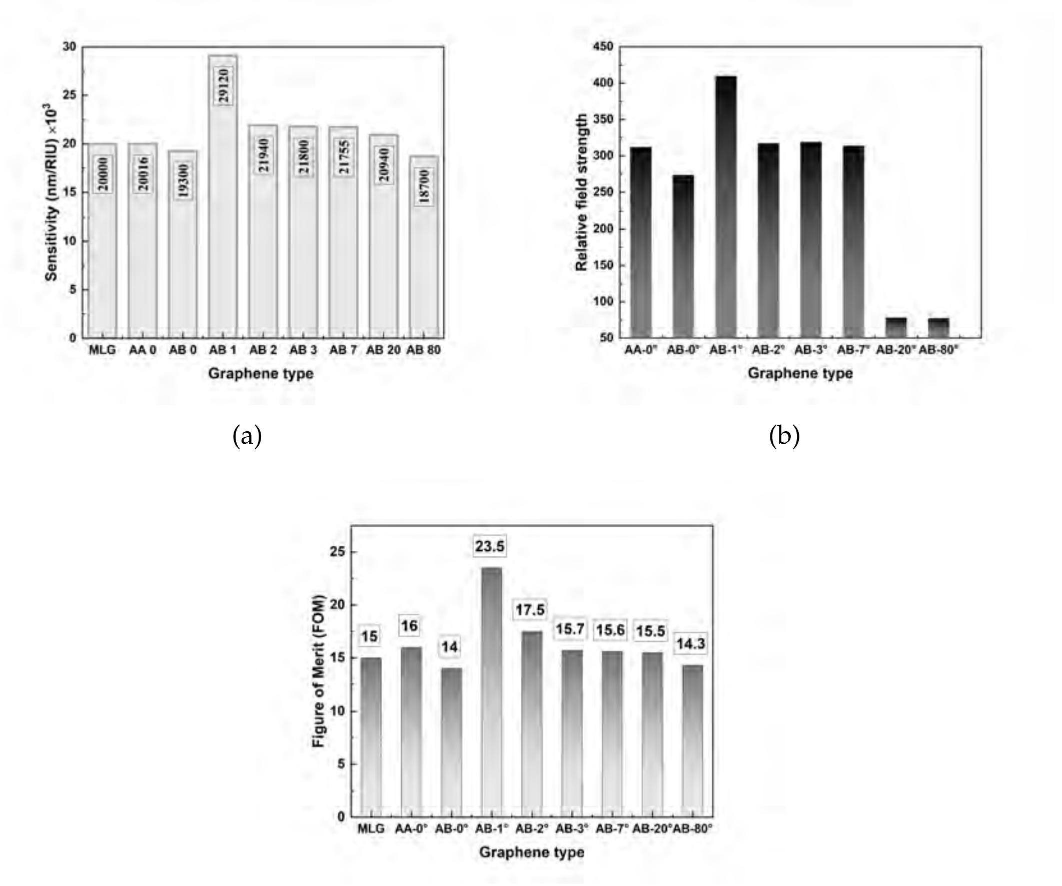

(a) (b)

(c)

Figure 6.14: (a) Sensitivity for different graphene systems. Corresponding values of sensitivity are as mentioned, (b) Relative plasmonic field strength (RFS) of BLG and T-BLG system in comparison to MLG system and (c) Figure-of-merit (FOM) for different graphene systems.

The sensitivity for MLG, and AA, AB stacked BLG system with 0° twist are comparably similar. Interestingly, on twisting the layers in Z/T/A system by 1°, the sensitivity of the sensor enhanced remarkably to 29120 nm/RIU which is more than 140% compared to MLG or BLG (with 0° twist). The sensitivity is lowest for 80° twist of the T-BLG system. The 2D plasmonic field over the surface (Y-Z plane) of BLG and T-BLG systems was estimated from the simulation. Interestingly, the magnitude is enhanced due to the addition of extra layer BLG as compared to MLG (Fig:-6.11-b. The relative field strength (RFS) was calculated from the ratio of fields of a BLG system to MLG system. As observed, the RFS increases to nearly 300 times on simply going from MLG to BLG system (Fig-6.14(b). Under the influence of twist in T-BLG, the RFS is found to be maximum (425) for a twist angle of 1°. It reduces to nearly to 315 on further increase of twist angle till 7°. There is a drastic decrease in RFS on higher twist angle (i.e., at 20° and 80°). This observation is in consistence with the sensitivity data as shown in Fig-6.14-a. The FOM was calculated for the BLG and T-BLG systems with different values of relative in-plane twist angles using Eq:-6.2. Fig-6.14-c shows the FOM for different graphene systems. The largest and the smallest values of FOM was obtained for 1^{circ} and 80^{circ} twist angle in the T-BLG system respectively. This is in consistent with the other parameters.

The T-BLG system possessing twist angle closer to 1° has been studied widely for its extraordinary behavior. This angle of twist is also called as magic angle. At this magic angle the T-BLG system shows superconducting behaviour as it exhibits ultra-flat bands near charge neutrality. For the twist angles close to the magic angle such as 1°, the energy separation between the nearly flat bands and the nearest conduction and valence bands is 100 meV which is comparable to energy of mid infrared regime (80 meV-200 meV). These energies are comparatively larger than the energy separation between the pair of nearly flat bands at the magic angle. When light impacts on T-BLG, its time-periodic electric field vibrates electrons around their equilibrium positions and induces an interband transition. When a plane polarized EM wave is incident, the electrons will build up an oscillating charge density with the same wavevector. This oscillating charge density in turn, creates an oscillating electric field that develops an external field, and at resonance this induced field is strong enough to maintain the oscillation for a longer duration. This resonance behaviour gives rise to collective modes that are called interband plasmons. Thus, due to this strong collective mode oscillation, the interaction with the nearby dielectric is enhanced. Therefore, the $\pi - \pi$ interaction with the analytes present in the sensing medium will also be high for the T-BLG near magic angle. Now as the twist angle moves further away the magic angle, the oscillation of this collective mode might decrease resulting in weaker interaction. Also, a strong coupling between the two layers of a BLG system is reported at the magic angle which reduces on increasing twist angle. In the present case, the decoupling is found near to 7° twist angle (Fig.-6.13(b)). For the very high twist angle (20° and 80°), the coupling increases to about 30-50 percent of the maximum. This is due to the traditional metallic behaviour of T-BLG system as calculated earlier using DFT.

6.4 Conclusion

In this chapter, we studied the optical properties of ultrathin film of graphene and its application in SPR based biosensing. We found that the optical properties of the graphene are stacking dependent. A comprehensive understanding of the optical and electrical properties of bilayer graphene (BLG) emerges, particularly in the context of different stacking configurations (AA and AB) and the application of relative in-plane twist. The impact of Moire patterns on the physical behavior of T-BLG is evident, suggesting the potential for tailored alterations in its optical and electrical properties.

The DFT calculations provides the differences in the refractive index (RI) between AA and AB stacked BLG. The absorption spectrum of AA stacking exhibits similarities to monolayer graphene, while AB stacking displays a red-shifted spectrum with enhanced metallicity. This variation in RI signifies the potential for diverse applications, especially in optical devices like sensors, optoelectronics, and lasers. The dielectric behavior of AA stacking and the predominance of semimetallic (SM) and semiconducting (SC) behaviors in AB stacking, as influenced by the in-plane relative twist, further underscore the versatility of BLG.

Further we extended our study into the application of BLG in SPR sensors. The dual functionality of BLG as a plasmonic material for surface plasmon polariton (SPP) wave generation and as a functional layer for analyte adsorption through $\pi - \pi$ interactions presents a novel approach. The simulation of SPR phenomena in monolayer graphene (MLG), bilayer graphene (BLG), and twisted bilayer graphene (T-BLG) provides insights into their sensing capabilities. The exceptional performance of T-BLG (AB stack) with a 1° twist angle, often referred to as the magic angle, surpasses the sensing merits of both MLG and BLG. The strong interlayer coupling in T-BLG near the magic angle results in exceptionally flat bands, enhancing the sensor's sensitivity, resonance frequency shift (RFS), and FOM. The optimization of the twist angle in BLG systems, especially T-BLG, emerges as a potential future direction of research and development. This work not only contributes to the fundamental understanding of BLG properties but also provides a practical framework for designing advanced optical devices with enhanced sensing capabilities, positioning BLG as a key material for the next generation of SPR sensors.

CHAPTER 7

Conclusion and Future Scope

The primary objective of this thesis is to investigate the fundamentals of scientific phenomena exhibited by materials at interfaces and explore the sensing applications of ultrathin films of such materials at fluid-solid interfaces. In material science engineering, different types of interfaces such as gas-gas, solid-solid , liquid-liquid, solid-liquid, gas-liquid and gas-solid exists. In this thesis we have focused our work in the realm of gas-liquid (air-water) and fluid-solid(air-solid and liquid-solid) interfaces. The air-water interface offers excess of surface free energy at the water surface which is ideal for studying the thermodynamics of ultrathin layer of molecules. Typically, the amphiphilic molecules tends to form a stable single layer of molecules when dispersed with a polar solvent on the A/W interface. However, there are materials which are not completely amphiphilic but they are of high technological importance such as nanomaterials, polymers and nanocomposites. There are several nanomaterials which can form a stable monolayer at the A/W interface.

Further the ultrathin 2D films can be transferred from the A/W interface onto the solid supports by employing a vertical deposition mechanism known as LB technique. The transferred layers can exhibit physicochemical properties remarkably different from their bulk counterparts. The transferred LB films can be judiciously used for various applications. The carbon nanomaterials showed superior interaction with a variety of materials particularly biological analytes. In this thesis, we have focused on the sensing application of the ultrathin films of carbon nanomaterials. For sensing applications, the ultrathin films can be deposited as a functional layer on the active surface of a transducer and further used for sensing a variety of analytes.

In this thesis, we have first discussed the brief introduction to the interfacial phenomena at the air-water and air-solid interface in chapter-1. In chapter-2 we have discussed the various experimental and simulation techniques employed for studying some of the systems.

In chapter-3, we have focused on the effect of functionalization of the CNT on the Langmuir monolayer at the air-water interface and the sensing ability of the LB films for acetone vapours at room temperature. We observed that spreading capability of ODA-CNT is better than the pristine-CNT at the air-water interface. Further, the morphology of the transferred LB films of pristine and ODA-CNT revealed the homogeneous and aligned morphology of the ODA-CNT as compared to that of pristine-CNT. The ultrathin film of ODA-CNT was used as the functional layer for sensing acetone vapor. The acetone sensing performance of films were measured using impedance spectroscopy. Impedance spectroscopy is a multiparameter technique which measures capacitance, resistance, real and imaginary impedance, phase difference, current as a function of input frequency. Most of the sensing platforms proposed for acetone sensing in literature have employed resistance as measuring parameter which is highly susceptible to change in temperature and humidity. Most of the reported work stated that the sensing of acetone can be done at elevated temperature. Therefore, the sensing of acetone at room temperature should be addressed with superior sensing parameters such as limit of detection and detectable concentration range. Principal component analysis (PCA) was employed to reduce the parameter space and select the most suitable measuring parameter during sensing of acetone using IS. We applied PCA on to the measured impedance data and observed capacitance to have larger variance with respect to acetone concentration. The study on acetone sensing using the ultrathin film of ODA-CNT indicated very low LOD and wider detectable concentration range even at room temperature. The sensing performance of LB film of ODA-CNT was compared with that of LB film of ODA-CNT and drop cast film of ODA-CNT.

Apart from health monitoring such as diabetes diagnosis, ultrathin films of carbon nanomaterials have also been used in environmental monitoring. The quality monitoring of potable water is essential to provide a safe life to the society. Often water sources get polluted due to several reasons. Among the several contaminants the biological contaminants such as E. coli poses serious hazards. E. coli bacteria is one of major concern in polluted water bodies. E. coli contaminate the sources of drinking water due to seavage leaks, animal contaminants, septic malfunctioning and improper disposal of human wastes. The detection of E. coli in potable water, food and beverages is essential. It is known that graphene being a bio compatible carbon nanomaterial has been employed for E. coli sensing in water. However, most of the proposed sensing platforms employing graphene as functional layer for pathogen sensing is further modified either with fluorescent labels or antigen-antibody label for selective detection of E. coli bacteria. In the chapter 4, we observed that LB film of ODA-functionalized graphene can be used as a suitable functional layer for selective determination of E. coli for a wide range of concentration. The lowest detectable concentration was 2.5 cfu/mL. The sensing measurements were performed using electrochemical impedance spectroscopy (EIS). We cultured six different bacteria: three from gram positive family and three form gran negative family. Later, the sensing response for the individual bacteria species were recorded and the data were analysed. Based on the analysis, it was observed that E. coli had a unique response compared to all other bacteria. The unique response of E. coli was due to the unique interaction of outer membrane of E. coli with graphene surface. The selective response were further checked by applying machine learning algorithm on the raw impedance data. The machine learning algorithms also showed unique response for E. coli.

The physical transducers plays crucial role during selective and efficient sensing. Some of the most commonly used transducers are piezoelectric, conductometric, magnetic, impedance, and optical. In the optical based biosensors, the system is generally labeled with some tag. Such labeling can effect the system due to the presence of the foreign molecules. Therefore, label-free optical sensing is more favorable than other techniques. The sensing using SPR ensures label-free measurement with a very high degree of sensitivity and resolution. There are some fundamental issues related to the SPR phenomenon used during sensing measurements. Some of the commonly issues which are not addressed sufficiently in the literature are: field distribution, role of anisotropic nature of the functional layer, surface density of the molecules/particles in the ultrathin film etc. In this thesis we highlighted such issues and performed systematic studies to understand the system in greater details.

In chapter-5, we addressed the role of optical anisotropy in the ultrathin film during SPR measurements. The plasmonic field distribution on the gold surface is found to be anisotropic. It is most likely that such anisotropy in field distribution can have huge impact on the SPR measurement for anisotropic film. We found that the SPR measurement are dependent on the relative angle between the plane of incidence and plane of anisotropy of the functional layer. Therefore, reference measurements are difficult. In order to understand the effect of optical anisotropy of the functional layer, we studied the plasmonic field distribution as a function of the degree of anisotropy and thickness of functional layer. We employed FDTD based electromagnetic simulation to perform the measurement and proposed a calibration curve of change in SPR angle with respect to film thickness and degree of anisotropy. Experimentally, we deposited LB films of 8CB liquid crystal and cadmium stearate and measured their SPR response for perpendicular and parallel direction. We also measured the thickness of both samples from XRR and based on the calibration curve we predicted the degree of anisotropy of both the systems. Therefore, analysis gives a strong foundation for the measurement of in-plane birefringence of ultrathin films of organic molecules which is essential for the development of optical devices.

It is observed during the deposition of ultrathin films as a functional layer, sometime the homogeneity of the film appears poor. Such non-homogeneous film can be considered as sub-monolayer rather than a monolayer. Therefore, the SPR measurement by assuming a uniform monolayer seems to be erroneous. Thus it is essential to study the SPR phenomenon by considering the sub-monolayer state of the ultrathin functional layer. In the chapter we have discussed the effect of surface density of metallic nanoparticles in the sub-monolayer regime on the SPR response. The surface density of the metallic nanoparticle are known to play a huge role in optical/electrical property of the film. We have used FDTD to calculate the SPR response for different surface density of silver nanoparticles as the functional layer over the conventional gold film. The SPR response for surface density less than 40% showed dielectric behavior and the corresponding SPR spectra undergoes red shift. As the surface density increased beyond 40%, a metallic behavior is observed and thus the SPR spectra show a blue shift. This phenomena is termed as Mott-Hubbard insulator metal transition (MI). For less surface density, the plasmonic waves of the silver nanoparticles has classical interaction. With decrease in the density, the quantum mechanical interaction starts to dominate leading to a metallic behavior of the film. Further, the simulation result was validated with SPR experiments in our lab. The silver nanoparticles were deposited on the gold chip by self assembly. The surface coverage was controlled by controlling the self-assembly with time. The morphology at different time stamps were obtained using FESEM and surface coverage was analyzed using ImageJ software. We found a good agreement of the experimental data with that of simulated data. Similarly the surface density of single walled carbon nanotubes was varied and SPR phenomenon was studied systematically. The effect of intertube separation and the alignment of CNT on the SPR response was studied. CNT have shape anisotropy, due to which the refractive index differs in both parallel and perpendicular alignment. In parallel alignment, the direction of polarization of incident wave is parallel to director axis of CNT whereas in perpendicular alignment, it is perpendicular. CNT tend to behave as a metallic layer when aligned in parallel and semiconducting in perpendicular orientation. We present our study on SPR by varying the surface density and alignment of the CNT. We observed anisotropic field behavior for parallel orientation and stratified for perpendicular. Further, when the tube density of the CNT were varied on the gold surface we observed huge change in SPR response. Although in both the alignments we observed significant change in resonance angle due to density variation but in case of parallel orientation the variation was comparatively larger. We also perturbed into the localized plasmon field distribution and field enhancement due to density variation. Thus, we calculated the enhancement factor for different separation od tubes i.e cavity size and observed it for both alignments. In parallel alignment the enhancement factor was around 190 for 0.5 nm cavity size and 150 for perpendicular alignment. As the parallel alignment showed metallic characteristics we observed higher enhancement in the plasmonic field.

Thus, it can be said that there are lot of fundamental issues needed to be addressed before deposition of such functional layer over the metallic film of SPR chip to improve its performance. Also the interaction between the gold chip and functional layer are weak and hinders the FOM of the device. The functionalization also increases the film thickness which reduces the quality factor of SPR measurement. Thus, there is a need to have dual nature film, which can generate plasmon and can offer high affinity to molecules for sensing applications.

Thus, In chapter-6 we propose graphene to be employed as the dual nature films for potential application is SPR based biosensing. Graphene is an established material, which has proved to be a good bio recognition nanomaterial. Further, due to its unique electronic and non linear optical properties,it has the ability to generate surface plasmons. However, in order to utilize graphene effectively as a layer for generating plasmons, thorough examination of its optical properties is essential. Therefore, in this chapter, we studied the optical properties of ultrathin film of graphene. We found that the optical properties of the graphene are stacking dependent. A comprehensive understanding of the optical and electrical properties of bilayer graphene (BLG) emerges, particularly in the context of different stacking configurations (AA and AB) and the application of relative in-plane twist. The impact of Moir´e patterns on the physical behavior of T-BLG is evident, suggesting the potential for tailored alterations in its optical and electrical properties.

The DFT calculations provides the differences in the refractive index (RI) between AA and AB stacked BLG. The absorption spectrum of AA stacking exhibits similarities to monolayer graphene, while AB stacking displays a red-shifted spectrum with enhanced metallicity. This variation in RI signifies the potential for diverse applications, especially in optical devices like sensors, optoelectronics, and lasers. The dielectric behavior of AA stacking and the predominance of semimetallic (SM) and semiconducting (SC) behaviors in AB stacking, as influenced by the in-plane relative twist, further underscore the versatility of BLG.

Further we extended our study into the application of BLG in surface plasmon resonance (SPR) sensors. The dual functionality of BLG as a plasmonic material for surface plasmon polariton (SPP) wave generation and as a functional layer for analyte adsorption through $\pi - \pi$ interactions presents a novel approach. The simulation of SPR phenomena in monolayer graphene (MLG), bilayer graphene (BLG), and twisted bilayer graphene (T-BLG) provides insights into their sensing capabilities. The exceptional performance of T-BLG (AB stack) with a 1° twist angle, often referred to as the magic angle, surpasses the sensing merits of both MLG and BLG. The strong interlayer coupling in T-BLG near the magic angle results in exceptionally flat bands, enhancing the sensor's sensitivity, resonance frequency shift (RFS), and FOM.

The synergistic integration of findings from this chapter points towards a promising field for the development of efficient SPR-based sensors. The optimization of the twist angle in BLG systems, especially T-BLG, emerges as a potential future direction. This work not only contributes to the fundamental understanding of BLG properties but also provides a practical framework for designing advanced optical devices with enhanced sensing capabilities, positioning BLG as a key material for the next generation of SPR sensors in various applications, including bio-sensing.

Future Scope

In this thesis we studied the behavior of different nanomaterials at interface and their applications. There is a large futue scope in the field.

- The twisted bilayer graphene system is a very exotic and interesting system. The experimental investigation of the twisted graphene system is very challenging and important. There are several techniques for depositing such a high precision system, but some modifications still need to be addressed. We have observed that the LB technique supports the transfer of a single layer of molecules at high precision. Therefore, it can be employed to deposit twisted bilayer graphene systems and study the different applications. However, transferring such an intricate system requires high precision and a highly stable layer at the interface.

- The Langmuir monolayer of ODA-gr seems very interesting after the collapse. This mechanism can provide a protocol to obtain 3D graphene with exceptionally high adsorption capabilities. Such thin films of 3D graphene can be explored for their application as supercapacitor, advanced sensing layer, photocatalysis, water purification, tissue engineering and heat sinks. These applications leverage the unique combination of properties offered by 3D graphene, including high surface area, excellent electrical and thermal conductivity, mechanical strength, and chemical stability.

- In chapter 5 we investigate the variation in SPR response due to density variation of spherical silver nanoparticles. However, it is interesting to investigate the role of shape and size of such nanoparticles. The study can be extended to different semiconducting systems as well.

Bibliography

[1] O. N. Oliveira Jr, L. Caseli, and K. Ariga, "*The past and the future of Langmuir and Langmuir–Blodgett films*," Chemical reviews **122**, 6459 (2022).

[2] B. Bai, D. Wang, and L.-J. Wan, "*Synthesis of covalent organic framework films at interfaces*," Bulletin of the Chemical Society of Japan **94**, 1090 (2021).

[3] G. Roberts, *Langmuir-blodgett films* (Springer Science & Business Media, 2013).

[4] V. M. Kaganer, H. Mohwald, and P. Dutta, "*Structure and phase transitions in Langmuir monolayers*," Reviews of Modern Physics **71**, 779 (1999).

[5] J. Zasadzinski, R. Viswanathan, L. Madsen, J. Garnaes, and D. Schwartz, "*Langmuir-blodgett films*," Science **263**, 1726 (1994).

[6] M. C. Petty, *Langmuir-Blodgett Films* (1996).

[7] A. Ulman, *An Introduction to Ultrathin Organic Films: From Langmuir–Blodgett to Self–Assembly* (Academic press, 2013).

[8] K. B. Blodgett, "*Monomolecular films of fatty acids on glass*," Journal of the American Chemical Society **56**, 495 (1934).

[9] K. B. Blodgett, "*Films built by depositing successive monomolecular layers on a solid surface*," Journal of the American Chemical Society **57**, 1007 (1935).

[10] M. Bodik, M. Jergel, E. Majkova, and P. Siffalovic, "*Langmuir films of low-dimensional nanomaterials*," Advances in Colloid and Interface Science **283**, 102239 (2020).

[11] H. Kim, Y. J. Lee, G. Byun, C. Choi, and W.-H. Yeo, "*Advances in ultrathin soft sensors, integrated materials, and manufacturing technologies for enhanced*

monitoring of human physiological signals," Advanced Electronic Materials **9**, 2201294 (2023).

[12] C. Tan, X. Cao, X.-J. Wu, Q. He, J. Yang, X. Zhang, J. Chen, W. Zhao, S. Han, G.-H. Nam, *et al.*, "*Recent advances in ultrathin two-dimensional nanomaterials*," Chemical reviews **117**, 6225 (2017).

[13] H. Zhang, "*Ultrathin two-dimensional nanomaterials*," ACS nano **9**, 9451 (2015).

[14] M. S. Mauter and M. Elimelech, "*Environmental applications of carbon-based nanomaterials*," Environmental science & technology **42**, 5843 (2008).

[15] D. Jariwala, V. K. Sangwan, L. J. Lauhon, T. J. Marks, and M. C. Hersam, "*Carbon nanomaterials for electronics, optoelectronics, photovoltaics, and sensing*," Chemical Society Reviews **42**, 2824 (2013).

[16] P. Xie, W. Yuan, X. Liu, Y. Peng, Y. Yin, Y. Li, and Z. Wu, "*Advanced carbon nanomaterials for state-of-the-art flexible supercapacitors*," Energy Storage Materials **36**, 56 (2021).

[17] Z. Wang, D. Shen, C. Wu, and S. Gu, "*State-of-the-art on the production and application of carbon nanomaterials from biomass*," Green Chemistry **20**, 5031 (2018).

[18] K. P. Loh, D. Ho, G. N. C. Chiu, D. T. Leong, G. Pastorin, and E. K.-H. Chow, "*Clinical applications of carbon nanomaterials in diagnostics and therapy*," Advanced Materials **30**, 1802368 (2018).

[19] A. C. Power, B. Gorey, S. Chandra, and J. Chapman, "*Carbon nanomaterials and their application to electrochemical sensors: a review*," Nanotechnology Reviews **7**, 19 (2018).

[20] Q. Cao and J. A. Rogers, "*Ultrathin films of single-walled carbon nanotubes for electronics and sensors: a review of fundamental and applied aspects*," Advanced Materials **21**, 29 (2009).

[21] D. S. Hecht, L. Hu, and G. Irvin, "*Emerging transparent electrodes based on thin films of carbon nanotubes, graphene, and metallic nanostructures*," Advanced materials **23**, 1482 (2011).

[22] M. Poonia, V. Manjuladevi, R. Gupta, S. K. Gupta, J. Singh, P. B. Agarwal, and J. Akhtar, "*Ultrathin films of single-walled carbon nanotubes: A potential methane gas sensor*," Science of Advanced Materials **7**, 455 (2015).

[23] X. Li, T. Yang, Y. Yang, J. Zhu, L. Li, F. E. Alam, X. Li, K. Wang, H. Cheng, C.-T. Lin, *et al.*, "*Large-area ultrathin graphene films by single-step marangoni self-assembly for highly sensitive strain sensing application*," Advanced Functional Materials **26**, 1322 (2016).

[24] G. Speranza, "*Carbon nanomaterials: Synthesis, functionalization and sensing applications*," Nanomaterials **11**, 967 (2021).

[25] F. R. Baptista, S. A. Belhout, S. Giordani, and S. J. Quinn, "*Recent developments in carbon nanomaterial sensors*," Chemical Society Reviews **44**, 4433 (2015).

[26] H. M. Fahmy, E. S. Abu Serea, R. E. Salah-Eldin, S. A. Al-Hafiry, M. K. Ali, A. E. Shalan, and S. Lanceros-Mendez, "*Recent progress in graphene- and related carbon-nanomaterial-based electrochemical biosensors for early disease detection*," ACS Biomaterials Science and Engineering **8**, 964 (2022).

[27] T. Pasinszki, M. Krebsz, T. T. Tung, and D. Losic, "*Carbon nanomaterial based biosensors for non-invasive detection of cancer and disease biomarkers for clinical diagnosis*," Sensors **17**, 1919 (2017).

[28] A. Thakur and A. Kumar, "*Recent advances on rapid detection and remediation of environmental pollutants utilizing nanomaterials-based (bio) sensors*," Science of The Total Environment **834**, 155219 (2022).

[29] L. Zhang and M. Fang, "*Nanomaterials in pollution trace detection and environmental improvement*," Nano Today **5**, 128 (2010).

[30] A. Tripathi and J. Bonilla-Cruz, "*Review on healthcare biosensing nanomaterials*," ACS Applied Nano Materials **6**, 5042 (2023).

[31] N. L. Teradal and R. Jelinek, "*Carbon nanomaterials in biological studies and biomedicine*," Advanced healthcare materials **6**, 1700574 (2017).

[32] R. G. Mendes, P. S. Wrobel, A. Bachmatiuk, J. Sun, T. Gemming, Z. Liu, and M. H. Rummeli, "*Carbon nanostructures as a multi-functional platform for sensing applications*," Chemosensors **6**, 60 (2018).

[33] R. Das, S. B. Abd Hamid, M. E. Ali, A. F. Ismail, M. Annuar, and S. Ramakrishna, "*Multifunctional carbon nanotubes in water treatment: the present, past and future*," Desalination **354**, 160 (2014).

[34] C. Yang, P. Wu, W. Gan, M. Habib, W. Xu, Q. Fang, and L. Song, "*Low temperature CVD growth of ultrathin carbon films*," AIP Advances **6** (2016).

[35] Y. M. Manawi, Ihsanullah, A. Samara, T. Al-Ansari, and M. A. Atieh, "*A review of carbon nanomaterials' synthesis via the chemical vapor deposition (CVD) method*," Materials **11**, 822 (2018).

[36] X. Wang, G. Li, R. Liu, H. Ding, and T. Zhang, "*Reproducible layer-by-layer exfoliation for free-standing ultrathin films of single-walled carbon nanotubes*," Journal of Materials Chemistry **22**, 21824 (2012).

[37] C.-Y. Su, A.-Y. Lu, Y. Xu, F.-R. Chen, A. N. Khlobystov, and L.-J. Li, "*High-quality thin graphene films from fast electrochemical exfoliation*," ACS nano **5**, 2332 (2011).

[38] Y. Huang, Y.-H. Pan, R. Yang, L.-H. Bao, L. Meng, H.-L. Luo, Y.-Q. Cai, G.-D. Liu, W.-J. Zhao, Z. Zhou, *et al.*, "*Universal mechanical exfoliation of large-area 2D crystals*," Nature communications **11**, 2453 (2020).

[39] L. Song, X. Cao, L. Li, Q. Wang, H. Ye, L. Gu, C. Mao, J. Song, S. Zhang, and H. Niu, "*General method for large-area films of carbon nanomaterials and application of a self-assembled carbon nanotube film as a high-performance electrode material for an all-solid-state supercapacitor*," Advanced Functional Materials **27**, 1700474 (2017).

[40] M. Yang, Y. Yang, H. Yang, G. Shen, and R. Yu, "*Layer-by-layer self-assembled multilayer films of carbon nanotubes and platinum nanoparticles with polyelectrolyte for the fabrication of biosensors*," Biomaterials **27**, 246 (2006).

[41] C. Venet, C. Pearson, A. Jombert, M. Mabrook, D. Zeze, and M. Petty, "*The morphology and electrical conductivity of single-wall carbon nanotube thin films prepared by the Langmuir–Blodgett technique*," Colloids and Surfaces A: Physicochemical and Engineering Aspects **354**, 113 (2010).

[42] M. Poonia, V. Manjuladevi, and R. Gupta, "*Ultrathin films of functionalised single-walled carbon nanotubes: a potential bio-sensing platform*," Liquid Crystals **47**, 1204 (2020).

[43] A. Gayakwad, V. Manjuladevi, and R. K. Gupta, "*Interfacial Langmuir-Blodgett layer of functionalized single-walled carbon nanotubes for efficient glucose sensing*," IEEE Sensors Journal (2023).

[44] G. Giancane, A. Ruland, V. Sgobba, D. Manno, A. Serra, G. M. Farinola, O. H. Omar, D. M. Guldi, and L. Valli, "*Aligning Single-Walled Carbon Nanotubes By Means Of Langmuir–Blodgett Film Deposition: Optical, Morphological, and Photo-electrochemical Studies*," Advanced Functional Materials **20**, 2481 (2010).

[45] S.-W. Choi, W.-S. Kang, J.-H. Lee, C. K. Najeeb, H.-S. Chun, and J.-H. Kim, "*Patterning of Hierarchically Aligned Single-Walled Carbon Nanotube Langmuir- Blodgett Films by Microcontact Printing*," Langmuir **26**, 15680 (2010).

[46] S. Abdulla and B. Pullithadathil, "*Unidirectional Langmuir–Blodgett-mediated alignment of polyaniline-functionalized multiwalled carbon nanotubes for NH3 gas sensor applications*," Langmuir **36**, 11618 (2020).

[47] J.-H. Lee, W.-S. Kang, C. K. Najeeb, B.-S. Choi, S.-W. Choi, H. J. Lee, S. S. Lee, and J.-H. Kim, "*A hydrogen gas sensor using single-walled carbon nanotube Langmuir–Blodgett films decorated with palladium nanoparticles*," Sensors and Actuators B: Chemical **188**, 169 (2013).

[48] X. Fan, Y. Xu, C. Ma, and W. He, "*In-situ growth of Co3O4 nanoparticles based on electrospray for an acetone gas sensor*," Journal of Alloys and Compounds **854**, 157234 (2021).

[49] S. Salehi, E. Nikan, A. A. Khodadadi, and Y. Mortazavi, "*Highly sensitive carbon nanotubes–SnO2 nanocomposite sensor for acetone detection in diabetes mellitus breath*," Sensors and Actuators B: Chemical **205**, 261 (2014).

[50] H. Lin, Y. Zheng, C. Zhong, L. Lin, K. Yang, Y. Liu, H. Hu, and F. Li, "*Controllable-assembled functional monolayers by the Langmuir–Blodgett technique for optoelectronic applications*," Journal of Materials Chemistry C **12**, 1177 (2024).

[51] X. Li, G. Zhang, X. Bai, X. Sun, X. Wang, E. Wang, and H. Dai, "*Highly conducting graphene sheets and Langmuir–Blodgett films*," Nature nanotechnology **3**, 538 (2008).

[52] S. Ramasamy, P. Nagamony, and V. Chinnuswamy, "*Self-assembled SnO2/reduced graphene oxide nanocomposites via Langmuir-Blodgett technique as anode materials for Li-ion batteries*," Materials Letters **218**, 295 (2018).

[53] M. Poonia, V. Manjuladevi, and R. Gupta, "*Ultrathin film of carboxylated graphene at air-water and air-solid interfaces*," Surfaces and Interfaces **13**, 37 (2018).

[54] D.-K. Kang, M. M. Ali, K. Zhang, S. S. Huang, E. Peterson, M. A. Digman, E. Gratton, and W. Zhao, "*Rapid detection of single bacteria in unprocessed blood using Integrated Comprehensive Droplet Digital Detection*," Nature communications **5**, 5427 (2014).

[55] J. A. Adkins, K. Boehle, C. Friend, B. Chamberlain, B. Bisha, and C. S. Henry, "*Colorimetric and electrochemical bacteria detection using printed paper-and transparency-based analytic devices*," Analytical chemistry **89**, 3613 (2017).

[56] M. Amiri, A. Bezaatpour, H. Jafari, R. Boukherroub, and S. Szunerits, "*Electrochemical methodologies for the detection of pathogens*," ACS sensors **3**, 1069 (2018).

[57] C. E. Rowland, C. W. Brown III, J. B. Delehanty, and I. L. Medintz, "*Nanomaterial-based sensors for the detection of biological threat agents*," Materials Today **19**, 464 (2016).

[58] H. Chen, Y. Xie, A. M. Kirillov, L. Liu, M. Yu, W. Liu, and Y. Tang, "*A ratiometric fluorescent nanoprobe based on terbium functionalized carbon dots for highly sensitive detection of an anthrax biomarker*," Chemical Communications **51**, 5036 (2015).

[59] S. Karuppiah, N. C. Mishra, W.-C. Tsai, W.-S. Liao, and C.-F. Chou, "*Ultrasensitive and low-cost paper-based graphene oxide nanobiosensor for monitoring water-borne bacterial contamination*," ACS sensors **6**, 3214 (2021).

[60] R. Hernandez, C. Valles, A. M. Benito, W. K. Maser, F. X. Rius, and J. Riu, "*Graphene-based potentiometric biosensor for the immediate detection of living bacteria*," Biosensors and bioelectronics **54**, 553 (2014).

[61] B. Liedberg, C. Nylander, and I. Lundström, "*Biosensing with surface plasmon resonance—how it all started*," Biosensors and Bioelectronics **10**, i (1995).

[62] C.-C. Chang, N.-F. Chiu, D. S. Lin, Y. Chu-Su, Y.-H. Liang, and C.-W. Lin, "*High-sensitivity detection of carbohydrate antigen 15-3 using a gold/zinc oxide thin film surface plasmon resonance-based biosensor*," Analytical chemistry **82**, 1207 (2010).

[63] V. Chabot, C. M. Cuerrier, E. Escher, V. Aimez, M. Grandbois, and P. G. Charette, "*Biosensing based on surface plasmon resonance and living cells*," Biosensors and Bioelectronics **24**, 1667 (2009).

[64] P. Singh, "*SPR biosensors: historical perspectives and current challenges*," Sensors and actuators B: Chemical **229**, 110 (2016).

[65] F. Wu, P. Thomas, V. Kravets, H. O. Arola, M. Soikkeli, K. Iljin, G. Kim, M. Kim, H. Shin, D. Andreeva, *et al.*, "*Layered material platform for surface plasmon resonance biosensing*," Scientific reports **9**, 20286 (2019).

[66] D. T. Nurrohman, Y.-H. Wang, and N.-F. Chiu, "*Exploring graphene and MoS2 chips based surface plasmon resonance biosensors for diagnostic applications*," Frontiers in Chemistry **8**, 728 (2020).

[67] S. H. Kim, T. U. Kim, H. Y. Jung, H. C. Ki, D. G. Kim, and B.-T. Lee, "*The effect of Au/Ag bimetallic thin-films on surface plasmon resonance properties comparing with those of Au and Ag single thin-films*," Journal of Nanoscience and Nanotechnology **18**, 1777 (2018).

[68] X. Luo, T. Qiu, W. Lu, and Z. Ni, "*Plasmons in graphene: recent progress and applications*," Materials Science and Engineering: R: Reports **74**, 351 (2013).

[69] T. J. Constant, S. M. Hornett, D. E. Chang, and E. Hendry, "*All-optical generation of surface plasmons in graphene*," Nature Physics **12**, 124 (2016).

[70] M. Maleki, M. Mehran, and A. Mokhtari, "*Design of a near-infrared plasmonic gas sensor based on graphene nanogratings*," JOSA B **37**, 3478 (2020).

[71] A. Nimbalkar and H. Kim, "*Opportunities and challenges in twisted bilayer graphene: a review*," Nano-Micro Letters **12**, 1 (2020).

[72] Y. Wang, Z. Ni, L. Liu, Y. Liu, C. Cong, T. Yu, X. Wang, D. Shen, and Z. Shen, "*Stacking-dependent optical conductivity of bilayer graphene*," ACS Nano **4**, 4074 (2010).

[73] J. Peng, G. Barnes, and I. Gentle, "*The structures of Langmuir–Blodgett films of fatty acids and their salts*," Advances in Colloid and Interface Science **91**, 163 (2001).

[74] J. Basu and M. K. Sanyal, "*Ordering and growth of Langmuir–Blodgett films: X-ray scattering studies*," Physics Reports **363**, 1 (2002).

[75] L. G. Parratt, "*Surface studies of solids by total reflection of X-rays*," Physical review **95**, 359 (1954).

[76] V. Devanarayanan, V. Manjuladevi, and R. Gupta, "*Surface plasmon resonance sensor based on a new opto-mechanical scanning mechanism*," Sensors and Actuators B: Chemical **227**, 643 (2016).

[77] P. Hohenberg and W. Kohn, "*Inhomogeneous electron gas*," Physical Review **136**, B864 (1964).

[78] M. Paradise and T. Goswami, "*Carbon nanotubes – Production and industrial applications*," Materials and Design **28**, 1477 (2007).

[79] L. Yu, C. Shearer, and J. Shapter, "*Recent Development of Carbon Nanotube Transparent Conductive Films*," Chemical Reviews **116**, 13413 (2016), pMID: 27704787, https://doi.org/10.1021/acs.chemrev.6b0017 .

[80] Y. Wu, X. Zhao, Y. Shang, S. Chang, L. Dai, and A. Cao, "*Application-Driven Carbon Nanotube Functional Materials*," ACS Nano **15**, 7946 (2021).

[81] V. Schroeder, S. Savagatrup, M. He, S. Lin, and T. M. Swager, "*Carbon Nanotube Chemical Sensors*," Chemical Reviews **119**, 599 (2018).

[82] E. Llobet, "*Gas sensors using carbon nanomaterials: A review*," Sensors and Actuators B: Chemical **179**, 32 (2013).

[83] Y. Wang, K. Zhang, J. Zou, X. Wang, L. Sun, T. Wang, and Q. Zhang, "*Functionalized horizontally aligned CNT array and random CNT network for CO2 sensing*," Carbon **117**, 263 (2017).

[84] M. Mittal and A. Kumar, "*Carbon nanotube (CNT) gas sensors for emissions from fossil fuel burning*," Sensors and Actuators B: Chemical **203**, 349 (2014).

[85] N. Lee, D. Chung, I. Han, J. Kang, Y. Choi, H. Kim, S. Park, Y. Jin, W. Yi, M. Yun, J. Jung, C. Lee, J. You, S. Jo, C. Lee, and J. Kim, "*Application of carbon nanotubes to field emission displays*," Diamond and Related Materials **10**, 265 (2001).

[86] H. Murakami, M. Hirakawa, C. Tanaka, and H. Yamakawa, "*Field emission from well-aligned, patterned, carbon nanotube emitters*," Applied Physics Letters **76**, 1776 (2000).

[87] M. Poonia, R. K. Gupta, V. Manjuladevi, S. K. Gupta, and J. Akhtar, "*Supramolecular assembly of single-walled carbon nanotubes at air-solid interface*," Journal of Nanoparticle Research **16** (2014), 10.1007/s11051-014-2572-2.

[88] I. Akhtar and S.-H. Chang, "*Highly aligned carbon nanotubes and their sensor applications*," Nanoscale **12**, 21447 (2020).

[89] M. Poonia, V. Manjuladevi, R. K. Gupta, S. K. Gupta, J. Singh, P. B. Agarwal, and J. Akhtar, "*Ultrathin Films of Single-Walled Carbon Nanotubes: A Potential Methane Gas Sensor*," Science of Advanced Materials **7**, 455 (2015).

[90] L. L. Zhang and X. S. Zhao, "*Carbon-based materials as supercapacitor electrodes*," Chemical Society Reviews **38**, 2520 (2009).

[91] H. Zhang, G. Cao, and Y. Yang, "*Carbon nanotube arrays and their composites for electrochemical capacitors and lithium-ion batteries*," Energy Environ. Sci. **2**, 932 (2009).

[92] X. Zhou, H. Cao, D. Yang, L. Zhang, L. Jiang, and M. Liu, "*Two-Dimensional Alignment of Self-Assembled Organic Nanotubes through Langmuir–Blodgett Technique*," Langmuir **32**, 13065 (2016).

[93] M. Penza, G. Cassano, P. Aversa, F. Antolini, A. Cusano, A. Cutolo, M. Giordano, and L. Nicolais, "*Alcohol detection using carbon nanotubes acoustic and optical sensors*," Applied Physics Letters **85**, 2379 (2004).

[94] M. Penza, F. Antolini, and M. V. Antisari, "*Carbon nanotubes as SAW chemical sensors materials*," Sensors and Actuators B: Chemical **100**, 47 (2004).

[95] F. A. Scholl, P. V. Morais, R. C. Gabriel, M. J. Schoning, J. R. Siqueira Jr, and L. Caseli, "*Carbon nanotubes arranged as smart interfaces in lipid Langmuir–Blodgett films enhancing the enzymatic properties of penicillinase for biosensing applications*," ACS applied materials and interfaces **9**, 31054 (2017).

[96] M. A. Deshmukh, M. D. Shirsat, A. Ramanaviciene, and A. Ramanavicius, "*Composites based on conducting polymers and carbon nanomaterials for heavy metal ion sensing*," Critical reviews in analytical chemistry **48**, 293 (2018).

[97] A. Gayakwad, V. Manjuladevi, and R. K. Gupta, "*Interfacial Langmuir-Blodgett layer of functionalized single-walled carbon nanotubes for efficient glucose sensing*," IEEE Sensors Journal (2023).

[98] S. Malik and C. C. Tripathi, "*Thin film deposition by Langmuir Blodgett technique for gas sensing applications*," J. Surf. Eng. Mater. Adv. Technol **03**, 235 (2013).

[99] S. Abdulla and B. Pullithadathil, "*Unidirectional Langmuir-Blodgett-Mediated Alignment of Polyaniline-Functionalized Multiwalled Carbon Nanotubes for NH3 Gas Sensor Applications*," Langmuir **36**, 11618 (2020).

[100] Q. Cao and J. A. Rogers, "*Ultrathin Films of Single-Walled Carbon Nanotubes for Electronics and Sensors: A Review of Fundamental and Applied Aspects*," Advanced Materials **21**, 29 (2009).

[101] A. A. Baharuddin, B. C. Ang, A. Haseeb, Y. C. Wong, and Y. H. Wong, "*Advances in chemiresistive sensors for acetone gas detection*," Materials Science in Semiconductor Processing **103**, 104616 (2019).

[102] N. Alizadeh, H. Jamalabadi, and F. Tavoli, "*Breath acetone sensors as non-invasive health monitoring systems: A review*," IEEE Sensors Journal **20**, 5 (2019).

[103] C. Wang, A. Mbi, and M. Shepherd, "*A study on breath acetone in diabetic patients using a cavity ringdown breath analyzer: Exploring correlations of breath acetone with blood glucose and glycohemoglobin A1C*," IEEE Sensors Journal **10**, 54 (2009).

[104] T. Liu, H. Guan, T. Wang, X. Liang, F. Liu, F. Liu, C. Zhang, and G. Lu, "*Mixed potential type acetone sensor based on GDC used for breath analysis*," Sensors and Actuators B: Chemical **326**, 128846 (2021).

[105] Y. Li, L. Qiao, D. Yan, L. Wang, Y. Zeng, and H. Yang, "*Preparation of Au-sensitized 3D hollow SnO2 microspheres with an enhanced sensing performance*," Journal of alloys and compounds **586**, 399 (2014).

[106] G. Li, Z. Cheng, Q. Xiang, L. Yan, X. Wang, and J. Xu, "*Bimetal PdAu decorated SnO2 nanosheets based gas sensor with temperature-dependent dual selectivity for detecting formaldehyde and acetone*," Sensors and Actuators B: Chemical **283**, 590 (2019).

[107] S. Zhang, W. Jiang, Y. Li, X. Yang, P. Sun, F. Liu, X. Yan, Y. Gao, X. Liang, J. Ma, *et al.*, "*Highly-sensitivity acetone sensors based on spinel-type oxide (NiFe2O4) through optimization of porous structure*," Sensors and Actuators B: Chemical **291**, 266 (2019).

[108] D.-H. Kim, J.-S. Jang, W.-T. Koo, S.-J. Choi, S.-J. Kim, and I.-D. Kim, "*Hierarchically interconnected porosity control of catalyst-loaded WO3 nanofiber scaffold: Superior acetone sensing layers for exhaled breath analysis*," Sensors and Actuators B: Chemical **259**, 616 (2018).

[109] H. Jung, W. Cho, R. Yoo, H.-s. Lee, Y.-S. Choe, J. Y. Jeon, and W. Lee, "*Highly selective real-time detection of breath acetone by using ZnO quantum dots with a miniaturized gas chromatographic column*," Sensors and Actuators B: Chemical **274**, 527 (2018).

[110] W. Liu, X. Zhou, L. Xu, S. Zhu, S. Yang, X. Chen, B. Dong, X. Bai, G. Lu, and H. Song, "*Graphene quantum dot-functionalized three-dimensional ordered mesoporous ZnO for acetone detection toward diagnosis of diabetes*," Nanoscale **11**, 11496 (2019).

[111] T. Xiao, X.-Y. Wang, Z.-H. Zhao, L. Li, L. Zhang, H.-C. Yao, J.-S. Wang, and Z.-J. Li, "*Highly sensitive and selective acetone sensor based on C-doped WO3 for potential diagnosis of diabetes mellitus*," Sensors and Actuators B: Chemical **199**, 210 (2014).

[112] P. Das, B. C. Behera, S. K. Panigrahy, A. K. Sahu, and S. K. Tripathy, "*Enhanced Acetone Sensing at Room Temperature using Tailored Co3O4 Nanostructures-Coated Optical Fibers: An Application towards Non-invasive Blood Glucose Sensor*," Surfaces and Interfaces **41**, 103256 (2023).

[113] C. Li, P. G. Choi, K. Kim, and Y. Masuda, "*High performance acetone gas sensor based on ultrathin porous NiO nanosheet*," Sensors and Actuators B: Chemical **367**, 132143 (2022).

[114] A. J. Qavi, A. L. Washburn, J.-Y. Byeon, and R. C. Bailey, "*Label-free technologies for quantitative multiparameter biological analysis*," Analytical and Bioanalytical Chemistry **394**, 121 (2009).

[115] C. L. Roozeboom, B. E. Hill, V. A. Hong, C. H. Ahn, E. J. Ng, Y. Yang, T. W. Kenny, M. A. Hopcroft, and B. L. Pruitt, "*Multifunctional Integrated Sensors for Multiparameter Monitoring Applications*," Journal of Microelectromechanical Systems **24**, 810 (2015).

[116] D. James, S. M. Scott, Z. Ali, and W. T. O'Hare, "*Chemical Sensors for Electronic Nose Systems*," Microchimica Acta **149**, 1 (2004).

[117] H. V. Shurmer and J. W. Gardner, "*Odour discrimination with an electronic nose*," Sensors and Actuators B: Chemical **8**, 1 (1992).

[118] C. L. Wong and M. Olivo, "*Surface Plasmon Resonance Imaging Sensors: A Review*," Plasmonics **9**, 809 (2014).

[119] Y. Zeng, R. Hu, L. Wang, D. Gu, J. He, S.-Y. Wu, H.-P. Ho, X. Li, J. Qu, B. Z. Gao, and Y. Shao, "*Recent advances in surface plasmon resonance imaging: detection speed, sensitivity, and portability*," Nanophotonics **6**, 1017 (2017).

[120] A. Ladniak, M. Jurak, and A. E. Wiacek, "*Langmuir monolayer study of phospholipid DPPC on the titanium dioxide–chitosan–hyaluronic acid subphases*," Adsorption **25**, 469 (2019).

[121] K. Choudhary, J. Kumar, P. Taneja, R. Gupta, and V. Manjuladevi, "*Langmuir–Blodgett films of stearic acid deposited on substrates at different orientations relative to compression direction: alignment layer for nematic liquid crystal*," Liquid Crystals **44**, 1592 (2017).

[122] V. T. Tiong, N. D. Pham, T. Wang, T. Zhu, X. Zhao, Y. Zhang, Q. Shen, J. Bell, L. Hu, S. Dai, and H. Wang, "*Octadecylamine-Functionalized Single-Walled Carbon Nanotubes for Facilitating the Formation of a Monolithic Perovskite Layer and Stable Solar Cells*," Advanced Functional Materials **28**, 1705545 (2018).

[123] S.-J. Young, Y.-H. Liu, Z.-D. Lin, K. Ahmed, M. N. I. Shiblee, S. Romanuik, P. K. Sekhar, T. Thundat, L. Nagahara, S. Arya, R. Ahmed, H. Furukawa, and A. Khosla, "*Multi-Walled Carbon Nanotubes Decorated with Silver Nanoparticles for Acetone Gas Sensing at Room Temperature*," Journal of The Electrochemical Society **167**, 167519 (2020).

[124] J. Kou, E. P. Nguyen, A. Merkoci, and Z. Guo, "*2-dimensional materials-based electrical/optical platforms for smart on-off diagnostics applications*," 2D Materials **7**, 032001 (2020).

[125] T. Kuila, S. Bose, P. Khanra, A. K. Mishra, N. H. Kim, and J. H. Lee, "*Recent advances in graphene-based biosensors*," Biosensors and bioelectronics **26**, 4637 (2011).

[126] J. Shen, N. Li, M. Shi, Y. Hu, and M. Ye, "*Covalent synthesis of organophilic chemically functionalized graphene sheets*," Journal of colloid and interface science **348**, 377 (2010).

[127] T. Kuila, S. Bose, A. K. Mishra, P. Khanra, N. H. Kim, and J. H. Lee, "*Chemical functionalization of graphene and its applications*," Progress in Materials Science **57**, 1061 (2012).

[128] Y.-K. Yang, C.-E. He, R.-G. Peng, A. Baji, X.-S. Du, Y.-L. Huang, X.-L. Xie, and Y.-W. Mai, "*Non-covalently modified graphene sheets by imidazolium ionic liquids for multifunctional polymer nanocomposites*," Journal of Materials Chemistry **22**, 5666 (2012).

[129] K. Yang, L. Feng, H. Hong, W. Cai, and Z. Liu, "*Preparation and functionalization of graphene nanocomposites for biomedical applications*," Nature protocols **8**, 2392 (2013).

[130] K. Fan, X. Liu, Y. Liu, Y. Li, Y. Chen, Y. Meng, X. Liu, W. Feng, and L. Luo, "*Covalent functionalization of fluorinated graphene through activation of dormant radicals for water-based lubricants*," Carbon **167**, 826 (2020).

[131] L. Chaabane, E. Beyou, D. Luneau, and M. H. V. Baouab, "*Functionalization of graphene oxide sheets with magnetite nanoparticles for the adsorption of copper ions and investigation of its potential catalytic activity toward the homocoupling of alkynes under green conditions*," Journal of catalysis **388**, 91 (2020).

[132] Y. JuáYun, H. JuáPark, S. EonáMoon, B. HoonáKim, *et al.*, "*A 3D scaffold for ultra-sensitive reduced graphene oxide gas sensors*," Nanoscale **6**, 6511 (2014).

[133] Y. Zou, N. Duan, S. Wu, M. Shen, and Z. Wang, "*Selection, identification, and binding mechanism studies of an ssDNA aptamer targeted to different stages of E. coli O157: H7*," Journal of agricultural and food chemistry **66**, 5677 (2018).

[134] J.-I. Lee, S.-S. Kim, and D.-H. Kang, "*Susceptibility of Escherichia coli O157: H7 grown at low temperatures to the krypton-chlorine excilamp*," Scientific reports **9**, 563 (2019).

[135] S. F. Oloketuyi and F. Khan, "*Strategies for biofilm inhibition and virulence attenuation of foodborne pathogen-Escherichia coli O157: H7*," Current microbiology **74**, 1477 (2017).

[136] H. Leclerc, D. Mossel, S. Edberg, and C. Struijk, "*Advances in the bacteriology of the coliform group: their suitability as markers of microbial water safety*," Annual Reviews in Microbiology **55**, 201 (2001).

[137] A. Bajwa, S. T. Tan, R. Mehta, and B. Bahreyni, "*Rapid detection of viable microorganisms based on a plate count technique using arrayed microelectrodes*," Sensors **13**, 8188 (2013).

[138] J. W.-F. Law, N.-S. Ab Mutalib, K.-G. Chan, and L.-H. Lee, "*Rapid methods for the detection of foodborne bacterial pathogens: principles, applications, advantages and limitations*," Frontiers in microbiology **5**, 770 (2015).

[139] Y. Huang, Z. Su, W. Li, and J. Ren, "*Recent progresses on biosensors for Escherichia coli detection*," Food Analytical Methods , 1 (2022).

[140] K. D. Young, "*The selective value of bacterial shape*," Microbiology and molecular biology reviews **70**, 660 (2006).

[141] K. Sharma and M. Sharma, "*Optical biosensors for environmental monitoring: Recent advances and future perspectives in bacterial detection*," Environmental Research , 116826 (2023).

[142] R. Jijie, K. Kahlouche, A. Barras, N. Yamakawa, J. Bouckaert, T. Gharbi, S. Szunerits, and R. Boukherroub, "*Reduced graphene oxide/polyethylenimine based immunosensor for the selective and sensitive electro-*

chemical detection of uropathogenic Escherichia coli," Sensors and Actuators B: Chemical **260**, 255 (2018).

[143] A. Gupta, S. K. Bhardwaj, A. L. Sharma, and A. Deep, "*A graphene electrode functionalized with aminoterephthalic acid for impedimetric immunosensing of Escherichia coli*," Microchimica Acta **186**, 1 (2019).

[144] S. S. Yoo, S. Y. Kim, K. S. Kim, S. Hong, M. J. Oh, M. G. Nam, W.-J. Kim, J. Park, C.-H. Chung, W.-S. Choe, *et al.*, "*Controlling inter-sheet-distance in reduced graphene oxide electrodes for highly sensitive electrochemical impedimetric sensing of myoglobin*," Sensors and Actuators B: Chemical **305**, 127477 (2020).

[145] A. Kumar, R. Gupta, and M. V., "*Selective detection of E.coli bacteria using ultrathin film of octadecylamine functionalized graphene*," Indian Patent , Application in progress (2024).

[146] S. Sieuwerts, F. A. De Bok, E. Mols, W. M. De Vos, and J. van Hylckama Vlieg, "*A simple and fast method for determining colony forming units*," Letters in applied microbiology **47**, 275 (2008).

[147] V. Devanarayanan, V. Manjuladevi, M. Poonia, R. Gupta, S. K. Gupta, and J. Akhtar, "*Measurement of optical anisotropy in ultrathin films using surface plasmon resonance*," Journal of Molecular Structure **1103**, 281 (2016).

[148] A. Joshi, A. Kumar, V. Manjuladevi, and R. Gupta, "*Modulating surface plasmon resonance response by an external electromagnetic wave*," Europhysics Letters **133**, 67005 (2021).

[149] A. Kumar, R. K. Gupta, M. V, and A. Joshi, "*Surface plasmon resonance for in-plane birefringence measurement of anisotropic thin organic film*," Plasmonics **16**, 1023 (2021).

[150] D. L. Allara and R. G. Nuzzo, "*Spontaneously organized molecular assemblies. 2. Quantitative infrared spectroscopic determination of equilibrium structures of solution-adsorbed n-alkanoic acids on an oxidized aluminum surface*," Langmuir **1**, 52 (1985).

[151] T. Martynski and J. Miyake, "*Langmuir–Blodgett films of dichroic dyes oriented by liquid crystal*," Supramolecular Science **5**, 643 (1998).

[152] A. Alizadehkhaledi, A. L. Frencken, M. K. Dezfouli, S. Hughes, F. C. van Veggel, and R. Gordon, "*Cascaded plasmon-enhanced emission from a single upconverting nanocrystal*," ACS Photonics **6**, 1125 (2019).

[153] C. M. Das, F. Yang, Z. Yang, X. Liu, Q. T. Hoang, Z. Xu, S. Neermunda, K. V. Kong, H.-P. Ho, L. A. Ju, *et al.*, "*Computational Modeling for Intelligent Surface Plasmon Resonance Sensor Design and Experimental Schemes for Real-Time Plasmonic Biosensing: A Review*," Advanced Theory and Simulations **6**, 2200886 (2023).

[154] R. Gupta, "*Sensing through surface plasmon resonance technique*," Reviews in Plasmonics 2016 , 39 (2017).

[155] R. Dkabrowski, P. Kula, and J. Herman, "*High birefringence liquid crystals*," Crystals **3**, 443 (2013).

[156] R.-P. Pan, C.-F. Hsieh, C.-L. Pan, and C.-Y. Chen, "*Temperature-dependent optical constants and birefringence of nematic liquid crystal 5CB in the terahertz frequency range*," Journal of Applied Physics **103** (2008).

[157] R. WS, "*Imagej, us national institutes of health, bethesda, maryland, usa*," http://imagej. nih. gov/ij/ (2011).

[158] A. Kumar, M. V, and R. Gupta, "*The Effect of Relative In-Plane Twisting in Graphene Bilayer on Sensing Using Surface Plasmon Resonance*," Plasmonics **18**, 213 (2023).

[159] J. Shiang, J. Heath, C. Collier, and R. Saykally, "*Cooperative phenomena in artificial solids made from silver quantum dots: the importance of classical coupling*," The Journal of Physical Chemistry B **102**, 3425 (1998).

[160] G. Markovich, C. P. Collier, S. E. Henrichs, F. Remacle, R. D. Levine, and J. R. Heath, "*Architectonic quantum dot solids*," Accounts of Chemical Research **32**, 415 (1999).

[161] N. Mott, *Metal-insulator transitions* (CRC Press, 2004).

[162] C. Collier, R. Saykally, J. Shiang, S. Henrichs, and J. Heath, "*Reversible tuning of silver quantum dot monolayers through the metal-insulator transition*," Science **277**, 1978 (1997).

[163] Y. Lan, Y. Wang, and Z. Ren, "*Physics and applications of aligned carbon nanotubes*," Advances in Physics **60**, 553 (2011).

[164] M. Terrones, "*Science and technology of the twenty-first century: synthesis, properties, and applications of carbon nanotubes*," Annual review of materials research **33**, 419 (2003).

[165] R. Rao, C. L. Pint, A. E. Islam, R. S. Weatherup, S. Hofmann, E. R. Meshot, F. Wu, C. Zhou, N. Dee, P. B. Amama, *et al.*, "*Carbon nanotubes and related nanomaterials: critical advances and challenges for synthesis toward mainstream commercial applications*," ACS nano **12**, 11756 (2018).

[166] V. Kumar, S. K. Raghuwanshi, and S. Kumar, "*Recent advances in carbon nanomaterials based spr sensor for biomolecules and gas detection-A review*," IEEE Sensors Journal (2022).

[167] E. G. Lee, K. M. Park, J. Y. Jeong, S. H. Lee, J. E. Baek, H. W. Lee, J. K. Jung, and B. H. Chung, "*Carbon nanotube-assisted enhancement of surface plasmon resonance signal*," Analytical biochemistry **408**, 206 (2011).

[168] Y. Zhou, W. Chang, H. Liu, Y. Wang, X. Zhao, and H. Chen, "*Single-walled carbon nanowires-integrated SPR biosensors: A facile approach for direct detection of exosomal PD-L1*," Sensors and Actuators B: Chemical **399**, 134795 (2024).

[169] G. Dresselhaus, M. S. Dresselhaus, and R. Saito, *Physical properties of carbon nanotubes* (World scientific, 1998).

[170] Z.-P. Yang, L. Ci, J. A. Bur, S.-Y. Lin, and P. M. Ajayan, "*Experimental observation of an extremely dark material made by a low-density nanotube array*," Nano letters **8**, 446 (2008).

[171] F. Garcia-Vidal, J. Pitarke, and J. Pendry, "*Effective medium theory of the optical properties of aligned carbon nanotubes*," Physical review letters **78**, 4289 (1997).

[172] J. Homola, "*Present and future of surface plasmon resonance biosensors*," Analytical and bioanalytical chemistry **377**, 528 (2003).

[173] J. Homola and M. Piliarik, *Surface plasmon resonance (SPR) sensors* (Springer, 2006).

[174] J. Homola, "*Surface plasmon resonance sensors for detection of chemical and biological species*," Chemical reviews **108**, 462 (2008).

[175] S. Szunerits, N. Maalouli, E. Wijaya, J.-P. Vilcot, and R. Boukherroub, "*Recent advances in the development of graphene-based surface plasmon resonance (SPR) interfaces*," Analytical and bioanalytical chemistry **405**, 1435 (2013).

[176] L. Wu, H.-S. Chu, W. S. Koh, and E.-P. Li, "*Highly sensitive graphene biosensors based on surface plasmon resonance*," Optics express **18**, 14395 (2010).

[177] L. He, Q. Pagneux, I. Larroulet, A. Y. Serrano, A. Pesquera, A. Zurutuza, D. Mandler, R. Boukherroub, and S. Szunerits, "*Label-free femtomolar cancer biomarker detection in human serum using graphene-coated surface plasmon resonance chips*," Biosensors and Bioelectronics **89**, 606 (2017).

[178] S. Chen and C. Lin, "*Figure of merit analysis of graphene based surface plasmon resonance biosensor for visible and near infrared*," Optics Communications **435**, 102 (2019).

[179] M. Vanin, J. J. Mortensen, A. Kelkkanen, J. M. Garcia-Lastra, K. S. Thygesen, and K. W. Jacobsen, "*Graphene on metals: A van der Waals density functional study*," Physical Review B **81**, 081408 (2010).

[180] C. Casiraghi, A. Hartschuh, E. Lidorikis, H. Qian, H. Harutyunyan, T. Gokus, K. S. Novoselov, and A. Ferrari, "*Rayleigh imaging of graphene and graphene layers*," Nano Letters **7**, 2711 (2007).

[181] L. Falkovsky, "*Optical properties of graphene*," in *Journal of Physics: Conference Series*, Vol. 129 (IOP Publishing, 2008) p. 012004.

[182] P. Blake, E. Hill, A. Castro Neto, K. Novoselov, D. Jiang, R. Yang, T. Booth, and A. Geim, "*Making graphene visible*," Applied Physics Letters **91**, 063124 (2007).

[183] G. Yang, L. Li, W. B. Lee, and M. C. Ng, "*Structure of graphene and its disorders: a review*," Science and Technology of Advanced Materials **19**, 613 (2018).

[184] A. Laref, M. Alsagri, S. M. Alay-e Abbas, S. Laref, H. Huang, Y. Xiong, J. Yang, S. A. Khandy, D. P. Rai, D. Varshney, *et al.*, "*Electronic structure and optical characteristics of AA stacked bilayer graphene: A first principles calculations*," Optik **206**, 163755 (2020).

[185] M. Koshino and T. Ando, "*Magneto-optical properties of multilayer graphene*," Physical Review B **77**, 115313 (2008).

[186] K. Patel and P. K. Tyagi, "*Multilayer graphene as a transparent conducting electrode in silicon heterojunction solar cells*," AIP Advances **5**, 077165 (2015).

[187] C. H. Lui, Z. Li, Z. Chen, P. V. Klimov, L. E. Brus, and T. F. Heinz, "*Imaging stacking order in few-layer graphene*," Nano Letters **11**, 164 (2011).

[188] Y. Hao, Y. Wang, L. Wang, Z. Ni, Z. Wang, R. Wang, C. K. Koo, Z. Shen, and J. T. Thong, "*Probing layer number and stacking order of few-layer graphene by Raman spectroscopy*," Small **6**, 195 (2010).

[189] I.-T. Lin, J.-M. Liu, K.-Y. Shi, P.-S. Tseng, K.-H. Wu, C.-W. Luo, and L.-J. Li, "*Terahertz optical properties of multilayer graphene: Experimental observation of strong dependence on stacking arrangements and misorientation angles*," Physical Review B **86**, 235446 (2012).

[190] E. McCann and M. Koshino, "*The electronic properties of bilayer graphene*," Reports on Progress in Physics **76**, 056503 (2013).

[191] Y. Duan, C. D. Stinespring, and B. Chorpening, "*Electronic structures, bonding configurations, and band-gap-opening properties of graphene binding with low-concentration fluorine*," Chemistry Open **4**, 642 (2015).

[192] S. Cheon, K. D. Kihm, H. goo Kim, G. Lim, J. S. Park, and J. S. Lee, "*How to reliably determine the complex refractive index (RI) of graphene by using two independent measurement constraints*," Scientific Reports **4**, 1 (2014).

[193] W. Kohn and L. J. Sham, "*Self-consistent equations including exchange and correlation effects*," Physical Review **140**, A1133 (1965).

[194] M. C. Payne, M. P. Teter, D. C. Allan, T. Arias, and a. J. Joannopoulos, "*Iterative minimization techniques for ab initio total-energy calculations: molecular dynamics and conjugate gradients*," Reviews of Modern Physics **64**, 1045 (1992).

[195] R. Brako, D. VSokVcević, P. Lazić, and N. Atodiresei, "*Graphene on the Ir (111) surface: from van der Waals to strong bonding*," New Journal of Physics **12**, 113016 (2010).

[196] S. J. Clark, M. D. Segall, C. J. Pickard, P. J. Hasnip, M. I. Probert, K. Refson, and M. C. Payne, "*First principles methods using CASTEP*," Zeitschrift für Kristallographie-Crystalline Materials **220**, 567 (2005).

[197] H. J. Monkhorst and J. D. Pack, "*Special points for Brillouin-zone integrations*," Physical Review B **13**, 5188 (1976).

[198] M. Klintenberg, S. Lebegue, C. Ortiz, B. Sanyal, J. Fransson, and O. Eriksson, "*Evolving properties of two-dimensional materials: from graphene to graphite*," Journal of Physics: Condensed Matter **21**, 335502 (2009).

[199] X. Wang, Y. P. Chen, and D. D. Nolte, "*Strong anomalous optical dispersion of graphene: complex refractive index measured by Picometrology*," Optics Express **16**, 22105 (2008).

[200] T. Xue, X. Cui, J. Chen, C. Liu, Q. Wang, H. Wang, and W. Zheng, "*A switch of the oxidation state of graphene oxide on a surface plasmon resonance chip*," ACS applied materials & interfaces **5**, 2096 (2013).

[201] F. Nelson, V. Kamineni, T. Zhang, E. Comfort, J. Lee, and A. Diebold, "*Optical properties of large-area polycrystalline chemical vapor deposited graphene by spectroscopic ellipsometry*," Applied Physics Letters **97**, 253110 (2010).

[202] P. Rani, G. S. Dubey, and V. Jindal, "*DFT study of optical properties of pure and doped graphene*," Physica E: Low-dimensional Systems and Nanostructures **62**, 28 (2014).

[203] H. A. Lorentz, *The theory of electrons and its applications to the phenomena of light and radiant heat*, Vol. 29 (GE Stechert & Company, 1916).

[204] I.-T. Lin, *Optical properties of graphene from the THz to the visible spectral region* (University of California, Los Angeles, 2012).

[205] E. V. Castro, K. Novoselov, S. Morozov, N. Peres, J. L. Dos Santos, J. Nilsson, F. Guinea, A. Geim, and A. C. Neto, "*Biased bilayer graphene: semiconductor with a gap tunable by the electric field effect*," Physical Review Letters **99**, 216802 (2007).

[206] A. Kuzmenko, L. Benfatto, E. Cappelluti, I. Crassee, D. Van Der Marel, P. Blake, K. Novoselov, and A. Geim, "*Gate tunable infrared phonon anomalies in bilayer graphene*," Physical Review Letters **103**, 116804 (2009).

[207] G. Jeong, B. Choi, D.-S. Kim, S. Ahn, B. Park, J. H. Kang, H. Min, B. H. Hong, and Z. H. Kim, "*Mapping of Bernal and non-Bernal stacking domains in bilayer graphene using infrared nanoscopy*," Nanoscale **9**, 4191 (2017).

[208] H. Tang, F. Du, S. Carr, C. DeVault, O. Mello, and E. Mazur, "*Modeling the optical properties of Twisted Bilayer Photonic Crystals*," arXiv preprint arXiv:2103.13600 (2021).

[209] F. Gargiulo and O. V. Yazyev, "*Structural and electronic transformation in low-angle twisted bilayer graphene*," 2D Materials **5**, 015019 (2017).

[210] E. Y. Andrei and A. H. MacDonald, "*Graphene bilayers with a twist*," Nature Materials **19**, 1265 (2020).

[211] G. T. De Laissardiere, D. Mayou, and L. Magaud, "*Numerical studies of confined states in rotated bilayers of graphene*," Physical Review B **86**, 125413 (2012).

[212] S. Adachi, *Handbook On Optical Constants Of Metals, The: In Tables And Figures* (World Scientific, 2012).

LIST OF PUBLICATIONS AND PRESENTATIONS

- **Publications in National/International Journals**

  1. **Amrit Kumar**, Raj Kumar Gupta, Manjuladevi V. and Ashutosh Joshi" Surface plasmon resonance for in-plane birefringence measurement of anisotropic thin organic film", *Plasmonics*, **16**, 1023-1028 (January 19, 2021).

  2. **Amrit Kumar**, Manjuladevi V. and R K Gupta, "Refractive index of graphene AA and AB stacked bilayers under the influence of relative planar twisting", *Journal of Physics: Condensed Matter (IOP)*, **34**,015302 (October 26, 2021).

  3. **Amrit Kumar**, Manjuladevi V. and R K Gupta, "The Effect of Relative In-Plane Twisting in Graphene Bilayer on Sensing Using Surface Plasmon Resonance", *Plasmonics*, **18**, 213-224 (December 15, 2022).

  4. **Amrit Kumar**, S.J. Shivaraja, Manjuladevi V. and R.K. Gupta " Ultrathin Langmuir-Blodgett film of functionalized single-walled carbon nanotubes for enhanced acetone sensing", *Microchemical Journal*, **200**,110219 (February 21, 2024).

  5. **Amrit Kumar**, Shweta Mishra, Manjuladevi V and Raj Kumar Gupta," Machine Learning assisted EIS based selective sensing of E.coli", *Manuscript Submitted.*

  6. **Amrit Kumar**, Akash Gayakwad, Manjuladevi V. and R K Gupta, "SPR investigation of sub-monolayer of silver nanoparticles", *Manuscript Submitted.*

  7. **Amrit Kumar**, Manjuladevi V. and R K Gupta, "Role of surface coverage/intertubular distance and alignment of CNT on SPR response", *Manuscript under preparation.*

- **Publications in National/International Journals: Not included in thesis**

1. I. Sill, B. Chakraborty, **Amrit Kumar**, S.J. Shivaraja, Manjuladevi V., R.K. Gupta and P. Bhattacharyya*" Fabrication, Structural, Electrical, and Optical Characterizations of p-Nanoparticle- and n-Nanotube-Based ZnO Homojunction", *IEEE Transactions on Electron Devices*, **67**,4256-4261 (September 03, 2020).
2. Ashutosh Joshi, **Amrit Kumar**, Manjuladevi V. and Raj Kumar Gupta, "Modulating surface plasmon resonance response by an external electromagnetic wave", *Europhysics Letters*, **133**,67005 (May 23, 2021).

- **Book Chapters**

1. **Amrit Kumar**, Manjuladevi V. and R K Gupta, "3D Graphene-Based Optical Sensors"In 3D Graphene: Fundamentals, Synthesis, and Emerging Applications *Springer, Cham.*, 2023.

2. **Amrit Kumar**, Manjuladevi V. and R K Gupta, "Materials for Langmuir Blodgett films. Langmuir-Blodgett Films: from Fundamentals to Application *Elsevier.*, In press.

- **Conference, Schools and Workshops Participation**

1. **Amrit Kumar** delivered a short invited talk on paper titled "Langmuir monolayer and Langmuir Blodgett films of Nematic Liquid Crystal molecules" at International Conference on Liquid Crystals, Liquid Crystalline Polymers and Nanosystems" (ICLCPN 2019) held at Mahatma Gandhi University, Kottayam, Kerala India, on December 13-15, 2019. He was awarded **2**nd prize for the talk.

2. **Amrit Kumar** participated "International Conference on Light Matter Interaction (ICLMIN-2021)", organised by Indira Gandhi Centre for Atomic Research (IGCAR), Kalpakkam, India during May 19-21, 2021

3. **Amrit Kumar** attended six weeks online school at "MaX School on Advanced Materials and Molecular Modelling with QE", organised by ICTP during May 17- June 30, 2021.

4. **Amrit Kumar** attended a seven days workshop "STUTI-2023" jointly organized by BITS PILANI, PILANI Campus and Amity University Jaipur January 2023.

BRIEF BIOGRAPHY OF THE SUPERVISOR

Prof. Raj Kumar Gupta is a professor in the Department of Physics, and Associate Dean, Grants,Consultancy and Industrial Research, Birla Institute of Technology & Science Pilani, Pilani Campus. He obtained the Doctorate of Philosophy from the Raman Research Institute, Bangalore, India in 2005 under the supervision of Professor K.A Suresh. He joined the Physics Department of BITS Pilani, Pilani Campus, in August 2005. He also worked as a visiting faculty at University of Colorado Boulder, USA in 2016. His research interests lies in thin films of mesogenic molecules, nanomaterials and the composites. Currently, his research interests are focused on understanding the change in properties of materials in the ultrathin film regime and its application for device fabrication. He has more than 70 publications and 10 book chapter of international repute. He has a patent on "A novel opto-mechanical system for measuring surface plasmon resonance" and filed another on portable nano-SPR device.

BRIEF BIOGRAPHY OF THE CANDIDATE

Mr. Amrit Kumar did is Bachelors in science from University of Delhi, India. He joined BITS Pilani in June 2019 as project fellow and later registered for PhD in the Department of Physics, BITS Pilani as a in August 2019. He is currently pursuing a PhD in the area of condensed matter physics. He has published research articles in reputed international journals. He has attended various workshops and conference on various topics during his PhD. His expertise lies in both simulation and experimental condensed matter physics.